



Universidad de  
Oviedo



# **ESCUELA POLITÉCNICA DE INGENIERÍA DE GIJÓN**

## **MÁSTER UNIVERSITARIO EN INGENIERÍA INDUSTRIAL**

### **ESPECIALIDAD EN DISEÑO Y FABRICACIÓN DE SISTEMAS MECÁNICOS**

#### **DESARROLLO Y PRODUCCIÓN DE UNA RUEDA CON MOTOR INTEGRADO PARA UN VEHÍCULO SOLAR DE COMPETICIÓN**

**ALEJANDRO BOBES DE JESÚS**  
**TUTOR: ANDREA ZUCHELLI**  
**COTUTOR: DAVIDE COCCHI**

**FECHA: Julio de 2019**

# ÍNDICE

<b>1.- ALOJAMIENTO DE LA RUEDA (SOPORTE DEL BUJE).....</b>	<b>3</b>
<b>2.- OPTIMIZACIÓN DE LA GEOMETRÍA DE LA LLANTA.....</b>	<b>6</b>
<b>3.- SECUENCIA DE LAMINACIÓN DE LA LLANTA Y DEL CERCO DE LA RUEDA .....</b>	<b>8</b>
3.1.- RESULTADOS DEL TEST DE FLEXIÓN (TÚV) .....	10
3.2.- RESULTADOS DE LA SIMULACIÓN DE LA PRESIÓN DE INFLADO .....	10
<b>4.- OPTIMIZACIÓN DE LA SECUENCIA DE LAMINACIÓN DEL CERCO.....</b>	<b>12</b>
4.1.- PARÁMETROS.....	13
4.2.- OBJETIVOS Y RESTRICCIONES .....	14
4.3.- OPTIMIZACIÓN Y POSIBLES SOLUCIONES .....	14
4.4.- COMPARACIÓN DE RESULTADOS .....	15

# 1.- ALOJAMIENTO DE LA RUEDA (SOPORTE DEL BUJE)

El objetivo de esta parte del proyecto ha sido la realización de un nuevo soporte para el buje de la rueda con motor integrado del coche solar Emilia 4.

El objetivo principal de diseño ha sido la obtención de un componente ligero pero lo suficientemente resistente como para soportar las condiciones de carga que actúan sobre la rueda. Por tanto, mediante simulaciones FEM, se ha tratado constantemente de realizar cambios en su geometría para reducir su peso lo máximo posible.

En primer paso del proceso, se ha realizado una optimización de la topología del componente en la que, partiendo de un diseño básico, se ha obtenido un diseño preliminar siguiendo las pautas que esta optimización mostraba en sus resultados (figura 1.1).

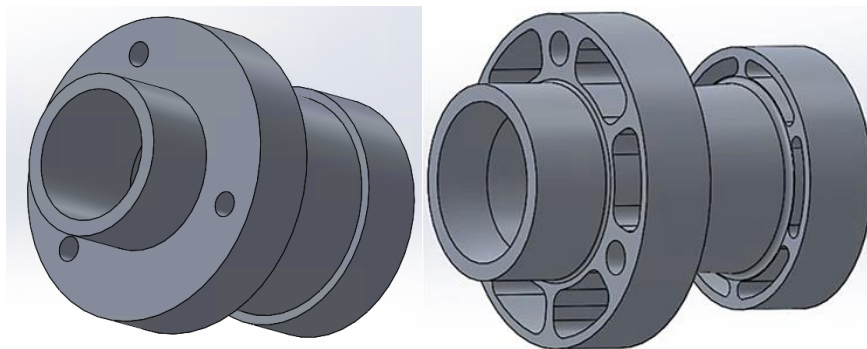


Figura 1.1: Evolución del diseño del alojamiento de la rueda a través de la optimización de la topología.

A partir de este diseño preliminar, se han realizado una serie de cambios (analizados mediante simulaciones FEM) hasta la obtención del componente final:

- Realización de los agujeros pertinentes para incluir los rodamientos en el interior del componente.
- Utilización de casquillos de acero para solventar el problema de la presión de contacto en ciertas zonas, debido a la transmisión del movimiento de rotación de la rueda a través de los pernos.

- Ampliación de los agujeros realizados en la parte exterior de la pieza para conseguir una mayor reducción de su peso. Por otro lado, también el espesor del componente ha sido disminuido considerablemente para alcanzar este objetivo.

Una vez se ha obtenido la forma final del componente teniendo en cuenta los cambios en su geometría mencionados anteriormente, se ha realizado una simulación final considerando todos los componentes del ensamblaje de la rueda. En esta simulación, al igual que en las anteriores se ha simulado tanto el efecto del momento torsor y flector que actúa sobre la rueda en las peores condiciones de carga.

En la figura 1.2, se muestran los resultados tanto del factor de seguridad del componente, como la tensión equivalente de Von Mises. A la vista de los resultados se puede observar que, en ciertas zonas, la tensión sobrepasa el límite elástico del componente (Alclad Aluminium 7075-T6).

Sin embargo, esto es debido a que en la simulación final se ha incluido el efecto de la pretensión de la unión roscada que existe en la parte izquierda del componente. Esto explica que en ciertas zonas de esa unión roscada, se supere el límite elástico (fenómeno frecuente en una unión atornillada). A pesar de esto, como se puede observar en los resultados, en el resto de zonas, el componente muestra un comportamiento idóneo.

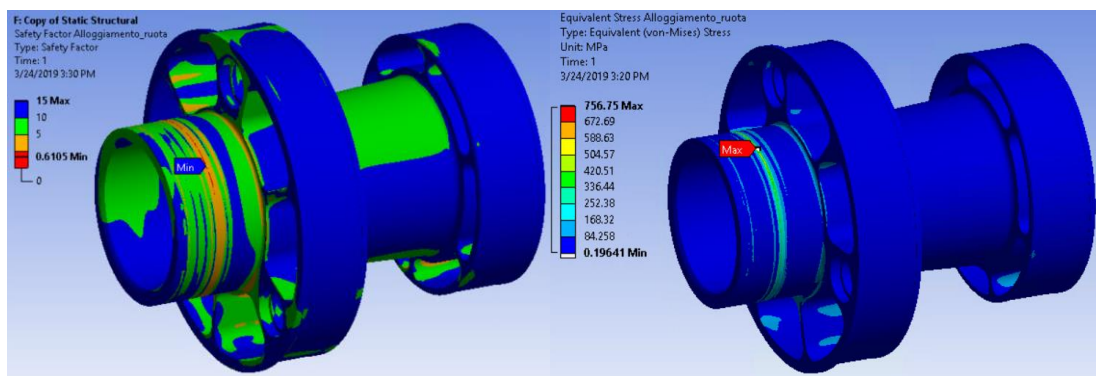


Figura 1.2: Resultados del factor de seguridad y del análisis tensional de Von Mises.

En el caso de la presión de contacto, añadiendo los casquillos de acero, su valor se ha incrementado notablemente comparándola con versiones anteriores en la que estos elementos no estaban presentes en el ensamblaje. A pesar de esto, hay que tener en cuenta que, al estar hechos de acero, su presión admisible es mucho mayor que la del aluminio. Por tanto, a pesar de que esta presión es muy alta al evaluar los resultados (figura 1.3), con

estos casquillos, se consigue un factor de seguridad aproximadamente 2 considerando la situación de carga más crítica.

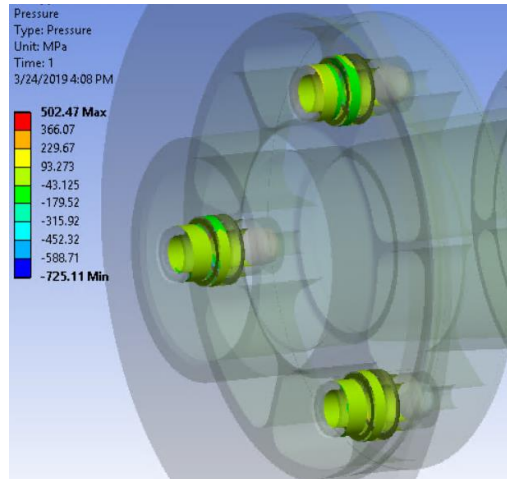


Figura 1.3: Distribución de la presión de contacto entre los pernos y los casquillos.

Por último, en la tabla 1.1, se muestra un resumen de las distintas simulaciones FEM que se han realizado, comparando los resultados de las diferentes versiones del alojamiento de la rueda. En esta tabla de resultados cabe destacar, la evolución de la masa del componente, habiendo reducido su valor en un 58% respecto al diseño inicial.

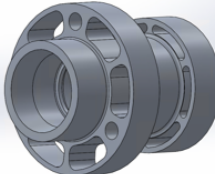
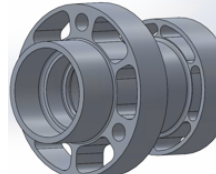
	VERSIONES			
	v 1.0	v 2.0	v 2.1	v 2.2 (Versión final)
				
Masa (g)	851.3	484.1	392.5	359.6
Variación masa (%)	REFERENCIA	-43%	-54%	-58%
Deformación máxima (mm)	0.04	0.05	0.67	-
Tensión máxima (MPa)	241.71	206.40	245.90	756.75* (*debido a la pretensión de la unión atornillada)
Presión de contacto máxima (MPa)	359.8	321.46	269.99	725.11

Tabla 1.1: Tabla resumen de las diferentes versiones del alojamiento de la rueda.

## 2.- OPTIMIZACIÓN DE LA GEOMETRÍA DE LA LLANTA

En esta parte del proyecto, se ha realizado una optimización de la geometría de la llanta de la rueda realizada en fibra de carbono. En primer lugar, se han determinado tres geometrías como posibles soluciones, cada una de ellas con una forma diferente (figura 2.1).

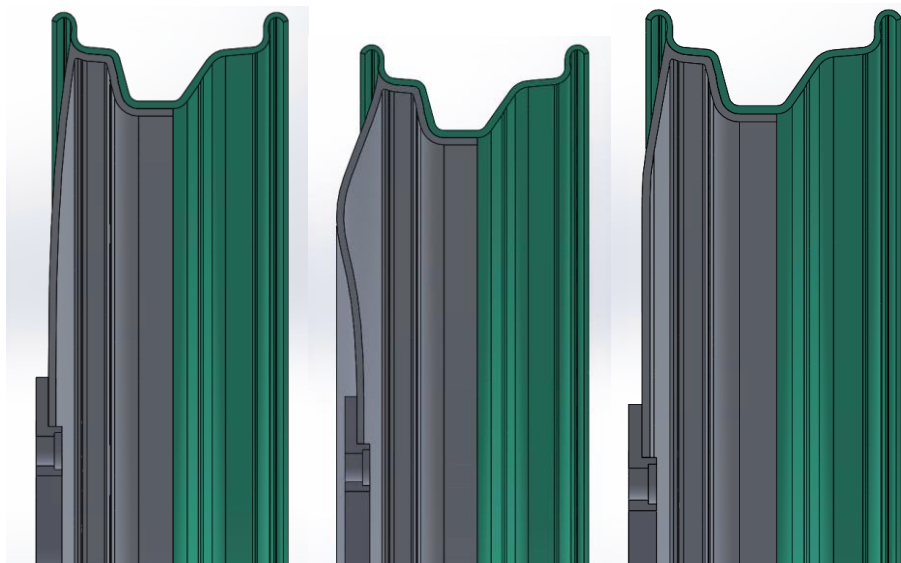


Figura 2.1: Diferentes tipos de llanta: recta, curvada y recta+ángulo.

Para determinar cuál de ellas es más apropiada para esta aplicación, se han considerado dos situaciones de carga diferente: el efecto del momento flector sobre la rueda y la rigidez de esta, cuando la rueda está en contacto con el suelo. Los resultados de ambas simulaciones se muestran en la tabla 2.1 y en la tabla 2.2:

Versión	Masa (g)	Forma de la llanta	Tipo de carga	Magnitud		Desplazamiento máx radial (mm)	Desplazamiento máx flexión (mm)	Máx tensión eq radial (MPa)	Máx tensión eq flexión (MPa)
v1.0 (REF)	1035	curvada	Radial	1000	N	0.59	-	31.9	-
			Flexión	100	Nm	-	0.63	-	67.7
v1.1	1021	recta	Radial	1000	N	0.84	-	46.2	-
			Flexión	100	Nm	-	1.00	-	94.9
v1.2	1023	recta+ángulo	Radial	1000	N	0.94	-	61.3	-
			Flexión	100	Nm	-	1.17	-	111.7

Tabla 2.1: Resumen de los resultados de las simulaciones.

Versión	Variación % desplazamiento radial	Variación % desplazamiento flexión	Variación % tensión respecto a la referencia (radial)	Variación % tensión respecto a la referencia (flexión)	Variación % masa respecto a la referencia
v1.0 (REF)	-	-	-	-	-
	-	-	-	-	-
v1.1	42.4%	-	44.8%	-	-1.4%
	-	58.7%	-	40.2%	-
v1.2	59.3%	-	92.2%	-	-1.2%
	-	85.7%	-	65.0%	-

Tabla 2.2: Comparación de los resultados entre las distintas versiones de la llanta.

Como se puede observar en la tabla 2.2, el diseño que ha obtenido los mejores resultados ha sido la llanta curva. Con esta geometría, los niveles de tensión y deformación son más bajos que en el resto de las versiones aunque sea la llanta más pesada. Por este motivo se ha decidido utilizar esta llanta curva como diseño preliminar del componente final.

A continuación, utilizando la geometría curva de la llanta, se han realizado diferentes tipos de llantas curvas cambiando ciertos parámetros geométricos como el diámetro de la zona curva al igual que su posición con respecto al eje de la rueda. De esta forma, se han obtenido cuatro geometrías curvas diferentes que han sido comparadas utilizando el estado de carga debido a la flexión.

En la tabla 2.3 se muestran los resultados de las simulaciones realizadas:

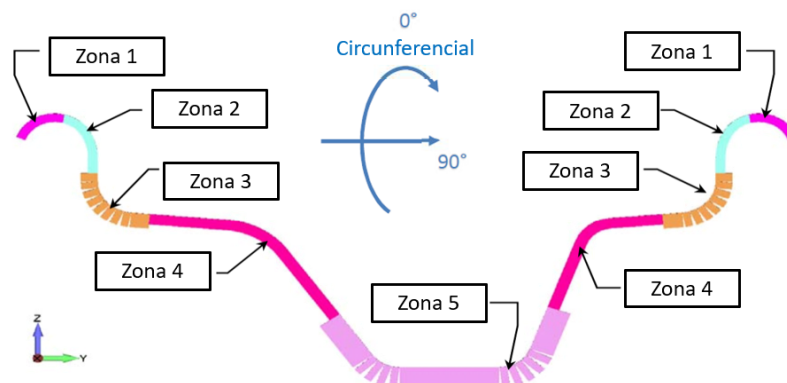
Versión	Variación % desplazamiento flexión	Variación % tensión respecto a la referencia (flexión)	Variación % masa respecto a la referencia
v2.0 (REF)	-	-	-
v2.1	-11.0%	-6.2%	-0.3%
v2.2	24.4%	15.9%	-0.9%
v2.3	-8.5%	-5.5%	-0.9%

Tabla 2.3: Comparación de resultados de las diferentes llantas curvas.

Como se puede observar en la tabla anterior, la mejor solución en términos de desplazamiento y tensiones es la v2.1. Sin embargo, se ha decidido escoger la versión v2.3 como la forma final de la llanta porque es más ligera que la v2.1, aunque sus resultados no sean los mejores.

### 3.- SECUENCIA DE LAMINACIÓN DE LA LLANTA Y DEL CERCO DE LA RUEDA

En el caso del cerco de la rueda, se ha realizado una laminación dividiendo la geometría del componente en diferentes zonas (figura 3.1). De esta forma, se ha OBTENIDO una secuencia de laminación tratando de reforzar las zonas críticas del cerco para mejorar su comportamiento ante los distintos estados de carga a los que estará sometido durante su funcionamiento. Además, esta laminación se ha hecho de tal forma que se puedan evitar más fácilmente la propagación de grietas en caso de que estas se produjesen durante la competición.



Secuencia de laminación	nº capas	orientación	Zona 1	Zona 2	Zona 3	Zona 4	Zona 5
			tipo de prepeg				
↑	2	0°	Twill T300				
	2	0°	UD T1000				
	2	0°					Twill T300
	1	0°				Twill T300	
	2	0°	Twill T300				
	4	90°					UD T1000
	2	90°					UD T1000
	1	45°	Twill T300				
	3	90°					UD T1000
	3	90°					UD T1000
1	0°	Twill T300					
Superficie del molde							
Espesor (mm)			1.03	1.38	2.12	3.43	4.11

Figure 3.1: Secuencia de laminación (plybook) del cerco de la rueda.

Por otro lado, la laminación de la llanta (tabla 3.1) se ha llevado a cabo reforzando la zona central de la misma, puesto que esta es una de las zonas críticas cuando el componente se encuentra sometido a flexión.

Tipo de prepeg	Nº de capas	Orientación	Zona
Twill T300	1	0° (R1)	Toda la parte exterior de la llanta (Lens1)
Twill T300	1	45° (R1 + 45°)	Disco central (D240 mm)
UD T1000	5 (x5 radios)	radial	Radios de la llanta
Twill T300	1	144° (R3)	Toda la parte exterior de la llanta (Lens1)
Tipo de prepeg	Nº de capas	Orientación	Zona
UD T1000	-	circunferencial	Relleno de la zona cerco-llanta
Biax T300	parches	radial	Piezas de unión cerco-llanta
Twill T300	1	189° (R3 + 45°)	Disco central (D240 mm)
UD T1000	4 (x5 radios)	radial	Radios de la llanta
Twill T300	1	288° (R5)	Toda la parte interna de la llanta (Lens2)
Twill T300	1	333° (R5 + 45°)	Disco central (D240 mm)
UD T1000	4 (x5 radios)	radial	Radios de la llanta
Twill T300	1	117° (R2 + 45°)	Disco central (D240 mm)
Twill T300	1	72° (R2)	Toda la parte interna de la llanta (Lens2)
UD T1000	5 (x5 radios)	radial	Radios de la llanta
Twill T300	1	261° (R4 + 45°)	Disco central (D240 mm)
Twill T300	1	216° (R4)	Toda la parte interna de la llanta (Lens2)

Tabla 3.1: Secuencia de laminación (plybook) de la llanta.

Con estas dos secuencias de laminación, se han realizado diferentes simulaciones considerando la dinámica del vehículo y los tests TÜV, que se utilizan para analizar el comportamiento de las ruedas de coches comerciales teniendo en cuenta las principales situaciones de carga de este tipo de componentes.

Sin embargo, en este documento solo se muestran los resultados del test de flexión (TÜV) y de la simulación de la presión de inflado, puesto que estas dos situaciones son las más críticas a las que estos componentes estarán sometidos.

### 3.1.- RESULTADOS DEL TEST DE FLEXIÓN (TÜV)

Utilizando el criterio de fallo Hashin 3D podemos observar que, tanto en la llanta como en el cerco, se obtienen valores aceptables en cuanto a la seguridad de los componentes (figura 3.1). Las zonas que se encuentran en rojo, es decir, con un factor de seguridad inverso mayor que uno, son valores que no se dan en la realidad como tal. Esto es debido a que estas zonas son, o bien fallos del mallado producido al generarse el modelo, o zonas de concentración de tensiones que solo existen en el modelo, pero no en la realidad (en un modelo no siempre es posible representar al cien por cien las condiciones reales del componente).

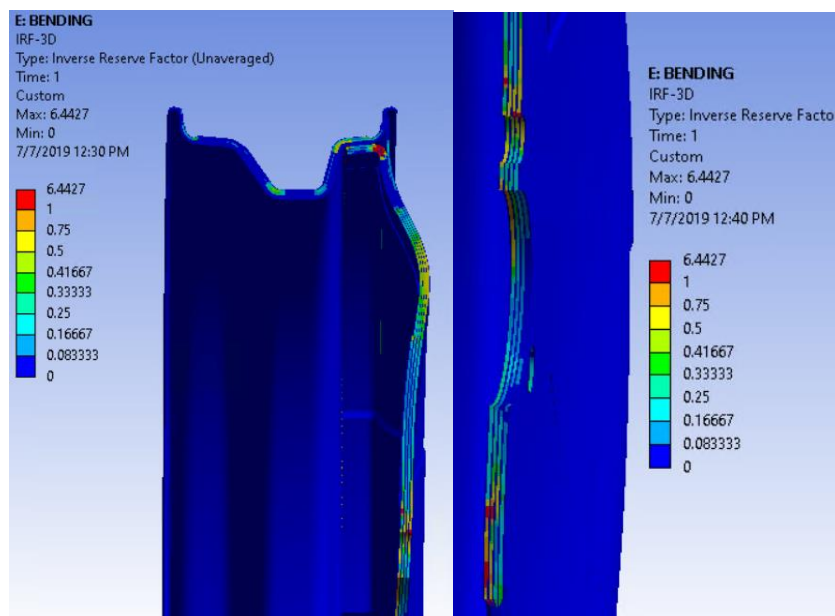


Figura 3.1: Resultados usando el criterio de fallo Hashin 3D en el test de flexión.

### 3.2.- RESULTADOS DE LA SIMULACIÓN DE LA PRESIÓN DE INFLADO

Al igual que en la simulación anterior, se ha utilizado el criterio de fallo Hashin 3D para evaluar los resultados (figura 3.2). En este caso se puede observar que, en ciertas zonas del cerco, existen problemas de rotura de matriz. Sin embargo, a la hora de realizar la secuencia de laminación, se ha intentado hacer de tal forma que se evite una posible propagación de grietas generadas a partir de estas microrroturas de matriz. De esta forma,

en caso de que se produzca una grieta, esta estaría aislada del resto de capas que conforman el componente.

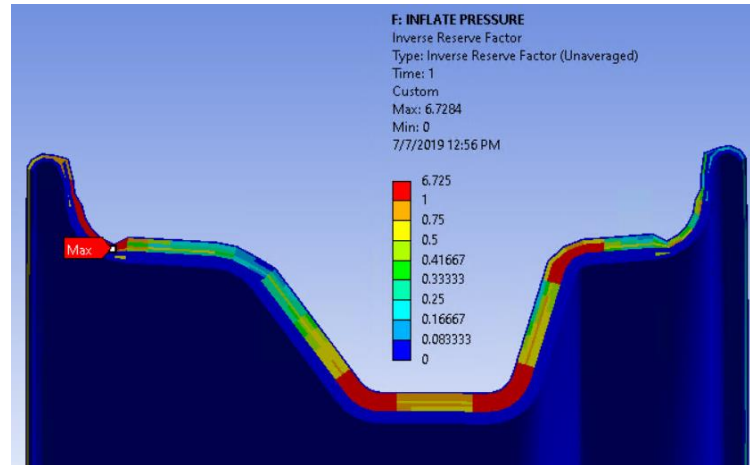


Figura 3.2: Resultados usando el criterio de fallo Hashin 3D en la simulación de la presión de inflado.

## 4.- OPTIMIZACIÓN DE LA SECUENCIA DE LAMINACIÓN DEL CERCO

Por último, se ha realizado una optimización de la secuencia de laminación del cerco siguiendo una metodología concreta (figura 4.1). En primer lugar, se ha realizado un modelo FEM simplificado en 2D para reducir el tiempo computacional a la hora de realizar las simulaciones y facilitar así la labor de la obtención de resultados. Utilizando ese modelo simplificado, mediante una optimización directa con ciertos objetivos y restricciones, se obtendrá la secuencia de laminación óptima. El último paso es el de evaluar esa nueva secuencia de laminación utilizando el modelo sólido en 3D utilizado anteriormente, para así realizar una comparativa directa con los resultados de la anterior secuencia de laminación.

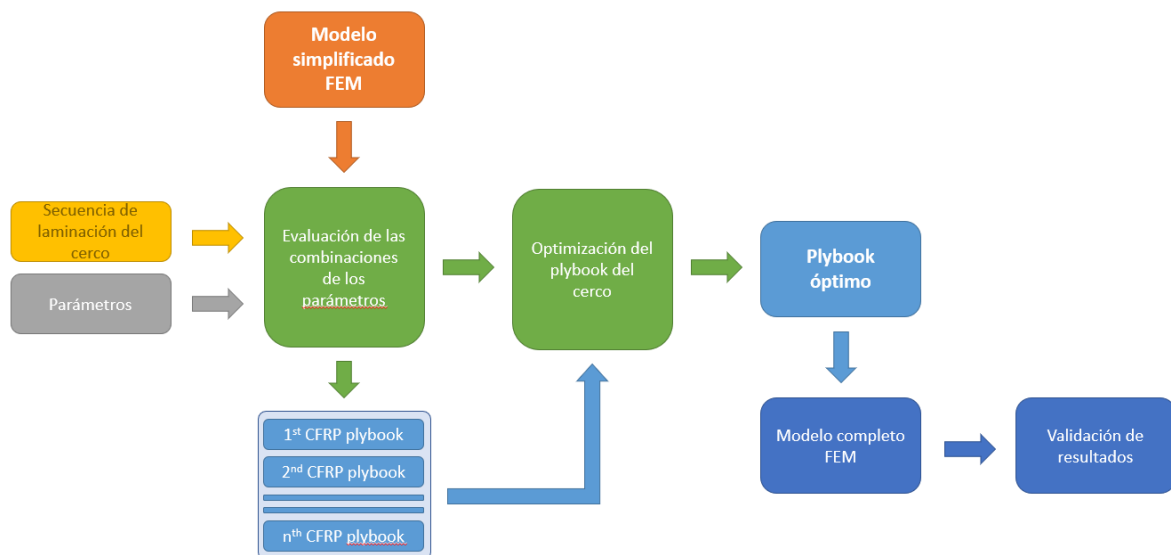


Figura 4.1: Diagrama de flujo del proceso de optimización.

### 4.1.- PARÁMETROS

Para esta optimización se han utilizado tres tipos de parámetros:

- Número de capas: este parámetro sirve para saber el posible número de capas en ciertas zonas de la secuencia de laminación.
- Orientación (ángulo de las capas): solamente en ciertas capas de Twill T300.
- Tipos de prepreg: este parámetro se utiliza para activar o desactivar una capa de Twill T300 considerando espesores relativamente bajos.

A continuación, en la tabla 4.1 se muestra la lista de los parámetros de entrada que han sido definidos para el proceso de optimización

2	2 TWILL T300 - FINAL		
2	2 UD T1000 (0)		
2	2 TWILL T300 (0) 4-5		
1	Twill T300 (0) 3-4-5		
2	2 TWILL T300 (0) 2-3-4-5		
4			4 UD T1000 (90) 5
2	2 UD T1000 (90) 4-5		
1	Twill T300 (45) 2-3-4-5		
3	3 UD T1000 (90) 4-5		
3	3 UD T1000 (90) 3-4-5		
1	Twill T300 - MOLD		
Mold surface			

1	Input Parameters			
2	Name	Lower Bound	Upper Bound	
3	P16 - TWILL T300 (0) 3-4-5.ply_material	1 2		
4	P17 - TWILL T300 - MOLD.number_of_layers	1 2		
5	P18 - 2 TWILL T300 (0) 2-3-4-5.number_of_layers	2 3		
6	P19 - TWILL T300 (0) 3-4-5.number_of_layers	1 2		
7	P20 - 2 TWILL T300 (0) 4-5.number_of_layers	2 3		
8	P21 - TWILL T300 (0) 3-4-5.ply_angle	45 0		
9	P22 - 2 TWILL T300 - FINAL.number_of_layers	2 1		
10	P23 - TWILL T300 (45)- 2-3-4-5.ply_angle	45 0		
11	P24 - 4 UD T1000 (90) 5.number_of_layers	4 2 3		
12	P25 - 2 UD T1000 (90) 4-5.number_of_layers	2 3 4		
13	P26 - 3 UD T1000 (90) 4-5.number_of_layers	3 2 4		
14	P27 - 3 UD T1000 (90) 3-4-5.number_of_layers	3 2 4		

Tabla 4.1: Lista de parámetros de entrada.

Por otro lado, los parámetros de salida para evaluar la secuencia de laminación son: el máximo valor de los criterios de fallo de Hashin (0.40416), Tsai-Wu (0.66427) y Maximum stress (0.6175), la deformación máxima direccional (1.577 mm) y el peso del cerco (759.67 g).

## 4.2.- OBJETIVOS Y RESTRICCIONES

Para esta optimización, los objetivos y restricciones (tabla 4.2), han sido definidos de la siguiente manera:

- Minimizar el máximo valor del factor inverso del criterio de Tsai-Wu.
- Minimizar el máximo valor del factor inverso del criterio de Maximum stress.
- Minimizar el máximo valor del factor inverso del criterio de Hashin.
- El peso máximo del cerco debe ser menor o igual que 780g.
- La suma del número de capas en cada grupo de UD T1000 debe ser como máximo 7. De esta forma, se evitan zonas con espesores relativamente grandes que puedan actuar como zonas de concentración de tensiones.

Table of Schematic G2: Optimization							
	A	B	C	D	E	F	G
1	Name	Parameter	Objective		Constraint		
2			Type	Target	Type	Lower Bound	Upper Bound
3	Minimize P14	P14 - IRF- TsaiWu Maximum	Minimize		No Constraint		
4	Minimize P13	P13 - IRF-MaxStress Maximum	Minimize		No Constraint		
5	Minimize P12	P12 - IRF-Hashin Maximum	Minimize		No Constraint		
6	P15	P15 - Directional Deformation Maximum	No Objective		No Constraint		
7	P29 <= 0.00078	P29 - Sensor.2.weight	No Objective		Values <= Upper Bound		0.00078
*		Select a Parameter					

Parameter Relationships				
	Name	Left Expression	Operator	Right Expression
18	P26+P27 <= 7	P26+P27	<=	7
19	P24+P25 <= 7	P24+P25	<=	7
*	<i>New Parameter Relationship</i>	<i>New Expression</i>	<=	<i>New Expression</i>

Tabla 4.2: Lista de objetivos y restricciones.

## 4.3.- OPTIMIZACIÓN Y POSIBLES SOLUCIONES

El método de optimización usado ha sido Screening con un número de 260 puntos de diseño.

Lo primero de todo, el sistema genera estos puntos escogiendo 260 puntos de todas las posibles combinaciones que existen. A continuación, el programa simula estas 260 combinaciones, y analizando una a una, considerando los objetivos y restricciones, se obtiene una lista de posibles soluciones (tabla 4.3).

En esta optimización, cinco posibles soluciones han sido generadas escogiendo la segunda de ellas como la solución óptima. Se ha decidido escoger esta, puesto que es la solución que tiene un valor más bajo de la deformación máxima direccional.

Candidate Points					
	Candidate Point 1	Candidate Point 2	Candidate Point 3	Candidate Point 4	Candidate Point 5
P16 - TWILL T300 (0) 3-4-5.ply_material	1	2	2	1	1
P17 - TWILL T300 - MOLD.number_of_layers	2	1	2	1	2
P18 - 2 TWILL T300 (0) 2-3-4-5.number_of_layers	3	3	3	2	3
P19 - TWILL T300 (0) 3-4-5.number_of_layers	1	2	1	1	1
P20 - 2 TWILL T300 (0) 4-5.number_of_layers	2	2	2	3	3
P21 - TWILL T300 (0) 3-4-5.ply_angle	45	45	0	0	45
P22 - 2 TWILL T300 - FINAL.number_of_layers	1	2	2	2	1
P23 - TWILL T300 (45) 2-3-4-5.ply_angle	0	0	0	0	0
P24 - 4 UD T1000 (90) 5.number_of_layers	4	4	2	4	2
P25 - 2 UD T1000 (90) 4-5.number_of_layers	3	2	2	2	3
P26 - 3 UD T1000 (90) 4-5.number_of_layers	2	2	2	2	2
P27 - 3 UD T1000 (90) 3-4-5.number_of_layers	2	4	3	3	2
P14 - IRF- TsaiWu Maximum	★ 0.49093	★ 0.49941	★★ 0.42904	★ 0.49417	★ 0.49029
P13 - IRF-MaxStress Maximum	★★ 0.44207	★★ 0.42212	★★ 0.43962	★★ 0.44739	★★ 0.44224
P12 - IRF-Hashin Maximum	★ 0.39546	★ 0.40522	— 0.4397	★ 0.39832	★ 0.40824
P15 - Directional Deformation Maximum (mm)	1.5585	1.4746	1.537	1.5476	1.5773
P29 - Sensor.2.weight	★★★ 0.00077362	★★★ 0.00077201	★★★ 0.00075104	★★★ 0.00076693	★★★ 0.00077092

Tabla 4.3: Lista de posibles soluciones.

Por tanto, de acuerdo con la información obtenida de la segunda solución, la secuencia de laminación óptima del cerco es la siguiente (tabla 4.4):

Secuencia de laminación	nº capas	orientación	Zona 1	Zona 2	Zona 3	Zona 4	Zona 5	
			tipo de prepreg					
	2	0°	Twill T300					
	2	0°	UD T1000					
	2	0°				Twill T300		
	3	0°	Twill T300					
	4	90°					UD T1000	
	2	90°				UD T1000		
	1	0°	Twill T300					
	2	90°				UD T1000		
	4	90°				UD T1000		
1	0°	Twill T300						
Superficie del molde								
Espesor (mm)			1.03	1.61	2.29	3.43	4.11	

Tabla 4.4: Secuencia de laminación del cerco óptima.

#### 4.4.- COMPARACIÓN DE RESULTADOS

Comparando las dos secuencias de laminación utilizando el modelo 3D, se puede observar que, añadiendo solamente 20 gramos aproximadamente, se han obtenido buenos resultados

reduciendo en gran medida tanto el valor del factor inverso Hashin 3D como la máxima deformación total (tabla 4.5).

	PLYBOOK ANTERIOR	PLYBOOK ÓPTIMO	Comparación (%)
Deformación total máxima (mm)	3.691	3.563	-3.5%
Hashin (3D)	6.725	6.303	-6.3%

Tabla 4.5: Comparación de resultados de las diferentes secuencias de laminación del cerco.



ALMA MATER STUDIORUM  
UNIVERSITÀ DI BOLOGNA

**LAUREA MAGISTRALE IN INGEGNERIA  
MECCANICA**

**DEVELOPMENT AND PRODUCTION OF A LIGHTWEIGHT  
MOTORWHEEL FOR A SOLAR RACE VEHICLE**

**ALEJANDRO BOBES DE JESÚS**

**TUTOR: ANDREA ZUCHELLI  
COTUTOR: DAVIDE COCCHI**



# INDEX

<b>1.- OBJECTIVE.....</b>	<b>7</b>
<b>2.- STATE OF THE ART .....</b>	<b>8</b>
2.1.- SOLAR CARS .....	8
2.1.1.- <i>Definition</i> .....	8
2.1.2.- <i>Solar car races</i> .....	8
2.1.2.1.- World solar challenge (WSC).....	8
2.1.2.2.- American solar challenge (ASC).....	9
2.1.3.- <i>Emilia 4 project</i> .....	10
2.2.- LIGHTWEIGHT WHEELS .....	11
2.2.1.- <i>Composite wheels</i> .....	11
2.2.1.1.- Composite wheel characteristics.....	12
2.2.1.2.- Wheels made of composite materials .....	13
2.3.- MOTORWHEELS .....	17
2.3.1.- <i>Protean in-wheel motors</i> .....	18
2.3.2.- <i>Michelin's Active Wheel</i> .....	19
2.3.3.- <i>Fraunhofer hub motor</i> .....	20
<b>3.- DESIGN OF A LIGHTWEIGHT CFRP MOTORWHEEL.....</b>	<b>22</b>
3.1.- DESIGN METHODS.....	22
3.1.1.- <i>Evolutionary algorithm</i> .....	22
3.1.2.- <i>Design of experiment</i> .....	27
3.2.- STANDARDS .....	33
3.2.1.- <i>TÜV E/ECE 324</i> .....	33
3.2.1.1.- Rotating bending test.....	34
3.2.1.2.- Rolling test .....	35
3.2.1.3.- Impact test .....	36
3.2.1.4.- Alternating torque test.....	36
3.3.- EMILIA 4 WHEELS.....	37
<b>4.- DESIGN PROCESS .....</b>	<b>48</b>
4.1.- WHEEL HOUSING.....	48
4.1.1.- <i>Material</i> .....	48
4.1.2.- <i>Topology optimization</i> .....	50
4.1.2.1.- Materials.....	51



4.1.2.2.- Loads & constraints.....	52
4.1.2.3.- Results.....	53
4.1.2.4.- Topology optimization.....	54
4.1.3.- FEM simulation (second design).....	56
4.1.3.1.- Results.....	57
4.1.4.- FEM simulation (third design).....	59
4.1.4.1.- Materials.....	59
4.1.4.2.- Loads & constraints.....	60
4.1.4.3.- Results.....	61
4.1.5.- Design of the final component.....	63
4.1.5.1.- Inner surface.....	63
4.1.5.2.- External surface.....	65
4.1.5.3.- Pins and its location.....	67
4.1.6.- FEM final simulation.....	68
4.1.6.1.- Materials.....	68
4.1.6.2.- Loads & constraints.....	68
4.1.6.3.- Results.....	69
4.2.- WHEEL LENS.....	72
4.2.1.- Lens design.....	72
4.2.1.1.- Straight lens.....	73
4.2.1.2.- Curved lens.....	74
4.2.1.3.- Straight+angle lens.....	74
4.2.1.4.- Radial stiffness simulation comparing different designs.....	75
4.2.1.4.1 Materials.....	75
4.2.1.4.2 Loads & constraints.....	75
4.2.1.4.3 Results.....	76
4.2.1.4.3.1 Curved lens.....	76
4.2.1.4.3.2 Straight lens.....	76
4.2.1.4.3.3 Straight+angle lens.....	77
4.2.1.5.- Bending stiffness simulation comparing different designs.....	77
4.2.1.5.1 Materials.....	77
4.2.1.5.2 Loads & constraints.....	77
4.2.1.5.3 Results.....	78
4.2.1.5.3.1 Curved lens.....	78
4.2.1.5.3.2 Straight lens.....	78
4.2.1.5.3.3 Straight+angle lens.....	79
4.2.1.6.- Conclusions.....	79
4.2.2.- Adhesive bond assessment.....	80
4.2.2.1.- Results.....	81
4.2.3.- New contact bond between flange and lens.....	82
4.2.4.- Shape optimization of the curved lens.....	82
4.2.4.1.- Results.....	83
4.2.4.1.1 v2.0.....	83



4.2.4.1.2 v2.1.....	84
4.2.4.1.3 v2.2.....	84
4.2.4.1.4 v2.3.....	85
4.2.4.2.- Conclusions.....	85
<b>5.- COMPOSITE COMPONENTS OPTIMIZATION.....</b>	<b>87</b>
5.1.- COMPOSITE MATERIALS .....	87
5.1.1.- Composite material definition .....	87
5.1.2.- Classification of composite materials.....	87
5.1.2.1.- Particle reinforced composite .....	88
5.1.2.2.- Reinforced composite with short fibers.....	88
5.1.2.3.- Reinforced composite with long fibers.....	88
5.1.2.3.1 Ply .....	88
5.1.2.3.2 Composite laminate .....	89
5.1.2.3.2.1 Advantages of composite laminates .....	89
5.1.2.3.2.2 Disadvantages of composite laminates.....	89
5.1.3.- FRP materials.....	90
5.1.4.- Prepregs .....	90
5.1.5.- Failure criteria .....	92
5.1.5.1.- Tsai-Hill criterion .....	92
5.1.5.2.- Tsai-Wu criterion .....	94
5.1.5.3.- Hashin criterion .....	94
5.1.5.4.- Maximum Stress criterion .....	95
5.1.6.- Manufacturing process.....	96
5.2.- COMPOSITE DESIGN & DOE.....	98
5.2.1.- Rim design & plybook .....	98
5.2.2.- Lens design & plybook .....	101
5.2.2.1.- Detailed lamination process of the lens .....	102
5.2.2.1.1 Phase 1 .....	102
5.2.2.1.2 Phase 2 .....	103
5.2.2.1.3 Phase 3 .....	103
5.2.2.1.4 Phase 4 .....	103
5.2.3.- Design of the molds .....	104
5.2.3.1.- Rim mold.....	104
5.2.3.2.- Lens mold.....	105
5.2.4.- Rotating bending test (modified from TÜV E/ECE324) simulation (v1.0) .....	106
5.2.4.1.- ACP (Pre).....	107
5.2.4.1.1 Geometry.....	107
5.2.4.1.2 Model .....	107
5.2.4.1.3 Setup.....	110
5.2.4.2.- Static structural.....	114
5.2.4.2.1 Materials.....	114



5.2.4.2.2	Loads & constraints .....	114
5.2.4.2.3	Results .....	115
5.2.5.-	<i>Rotating bending test (modified from TÜV E/ECE324) simulation (v1.1)</i> .....	117
5.2.5.1.-	Results .....	119
5.2.6.-	<i>Rotating bending test (modified from TÜV E/ECE324) simulation (v2.0)</i> .....	120
5.2.6.1.-	Results .....	122
5.2.7.-	<i>Rim inflation pressure simulation (v2.0)</i> .....	123
5.2.7.1.-	Load & constraints .....	123
5.2.7.2.-	Results .....	124
5.2.8.-	<i>Torsion (rev CD – vehicle dynamics) simulation (v2.0)</i> .....	124
5.2.8.1.-	Loads & constraints .....	125
5.2.8.2.-	Results .....	125
5.2.9.-	<i>Impact (rev CD – vehicle dynamics) simulation (v2.0)</i> .....	126
5.2.9.1.-	Loads & constraints .....	126
5.2.10.-	<i>Results</i> .....	127
5.2.11.-	<i>Rolling (modified from TÜV E/ECE 324) simulation (v2.0)</i> .....	127
5.2.11.1.-	Load & constraints .....	127
5.2.11.2.-	Results .....	128
5.2.12.-	<i>Curve loads (rev CD – vehicle dynamics) simulation (v2.0)</i> .....	128
5.2.12.1.-	Loads & constraints .....	128
5.2.12.2.-	Results .....	129
5.2.13.-	<i>DOE (direct optimization)</i> .....	129
5.2.13.1.-	Parameters .....	131
5.2.13.2.-	Objectives and constraints .....	132
5.2.13.3.-	Optimization and candidate points .....	132
5.2.13.4.-	Results comparison .....	135
<b>6.-</b>	<b>PRODUCTION PROCESS .....</b>	<b>137</b>
6.1.-	LAMINATION OF THE RIM .....	137
6.2.-	LAMINATION OF THE EXTERNAL PART OF THE LENS (LENS1) .....	139
6.3.-	LAMINATION OF THE INTERNAL PART OF THE LENS (LENS2) .....	142
6.4.-	MANUFACTURED COMPONENTS .....	143
<b>7.-</b>	<b>CONCLUSIONS .....</b>	<b>144</b>
<b>8.-</b>	<b>BIBLIOGRAPHY .....</b>	<b>146</b>
<b>9.-</b>	<b>ANNEX I.- CALCULATION OF THE BOLT PRETENTION .....</b>	<b>151</b>
<b>10.-</b>	<b>ANNEX II.- CALCULATION OF THE CONTACT PRESSURE .....</b>	<b>153</b>
10.1.-	BENDING ASSESSMENT .....	154
10.2.-	SHEAR ASSESSMENT .....	155
10.3.-	ADMISSIBLE CONTACT PRESSURE ASSESSMENT .....	156



10.3.1.- Region 2.....	156
10.3.2.- Region 1.....	157
<b>11.- ANNEX III.- COMPOSITE MATERIALS DATA.....</b>	<b>158</b>
11.1.- T1000 UD .....	158
11.2.- M40J UD.....	160
11.3.- TWILL T300.....	162
11.4.- BIAXIAL T300.....	163
11.5.- TWILL T800 (ISOTROPIC AND HOMOGENEOUS) .....	165
<b>12.- ANNEX IV.- PLANIFICATION .....</b>	<b>167</b>

# 1.- OBJECTIVE

This project is an optimization of a previous version of the motorwheel, already installed on the solar vehicle Emilia 4, produced by Onda Solare team. The work is regarding the lightening of the wheel group, in particular, the optimization of critical components, as hub supports, bearings, rims, lenses and other special features.

In this project, the following tasks have been carried out:

- Analysis of loads and constraints of the solar car. Comparison of the results directly on dynamic analysis performed in the previous version of the car (accelerometer tests, road tests...).
- Development of the hub support, using FEM tools supported by topology optimization.
- Development of the wheel shape: definition of old and new constraints. Evaluations in relationship with updated loads. Development based on the previous wheel experience.
- Optimization of the lens geometry and lamination sequence of its CFRP plies. This has been performed with FEM tools specific for composite materials, including a DOE analysis.
- Design of the molds to produce the CFRP (carbon fiber reinforced plastic) wheel.
- Monitoring of the manufacturing process of all the components directly in the producer workshop.

## **2.- STATE OF THE ART**

### **2.1.- SOLAR CARS**

#### **2.1.1.- Definition**

A solar car is a solar vehicle used for land transport. These cars run on only with sun power, managing that energy with electrical components as batteries and solar panels.

Solar cars combine technology normally used in the automotive, bicycle, alternative energy and aerospace industries. The design of a solar vehicle is limited by the amount of energy input into the car. Nowadays, most solar cars have been built for solar car races. Some prototypes have been done for public use, but currently, no cars primarily powered by the sun are available commercially.

Solar cars depend on a solar array that uses PV cells (photovoltaic cells) to obtain electricity from the sunlight. When the sunlight photons strike these cells, they excite electrons and allow them to flow, obtaining an electric current. PV cells are made of semiconductor materials such as gallium, nitrogen, silicon and alloys of indium. The most common material used is the crystalline silicon which has an efficiency rate of 15-20%. [1]

#### **2.1.2.- Solar car races**

##### **2.1.2.1.- World solar challenge (WSC)**

The World Solar Challenge or Bridgestone World Solar Challenge is the world's most well-known solar-powered car race event. This event has been created in 1987 to promote the development of experimental, solar-powered vehicles covering 3,022 km through the Australian Outback, from Darwin, Northern Territory, to Adelaide, South Australia (figure 2.1).

This race attracts teams from around the world, most of which are fielded by universities or corporations. Initially held once every three years, the event became biennial from the turn of the century.[2]



Figure 2.1: 3000 km route of World Solar Challenge. [2]

Participating teams enter their vehicle into of the following three categories [3]:

- The Challenger Class: for single-seat solar cars designed to be fast.
- The Cruiser Class: for efficient, practical solar cars with two or more seats.
- The Adventure Class: is a non-competitive class for solar cars built for previous events.

#### 2.1.2.2.- American solar challenge (ASC)

The American Solar Challenge, previously known as the North American Solar Challenge and Sunrayce, is a competition to design, build, and drive solar-powered cars in a cross-country time/distance rally event. Teams compete over a 1,500-2,000 mile course between multiple cities across the country. The event has had over two decades of organized events in North America.

This event is a test of teamwork, engineering skill, and endurance that stretches across thousands of miles of public roads. [4]

The routes have varied greatly over the course of the event history:

- 1990 – GM Sunrayce USA – Orlando, FL to Warren, MI
- 1993 – Sunrayce93 – Arlington, TX to Minneapolis, MN
- 1995 – Sunrayce95 – Indianapolis, IN to Golden, CO
- 1997 – Sunrayce97 – Indianapolis, IN to Colorado Springs, CO

- 1999 – Sunrayce99 – Washington, D.C. to Orlando, FL
- 2001 – American Solar Challenge 2001 – Chicago, IL to Claremont, CA
- 2003 – American Solar Challenge 2003 – Chicago, IL to Claremont, CA
- 2005 – North American Solar Challenge 2005 – Austin, TX to Calgary, Alberta, Canada
- 2008 – North American Solar Challenge 2008 – Plano, TX to Calgary, Alberta, Canada
- 2010 – American Solar Challenge 2010 – Broken Arrow, OK to Naperville, IL
- 2012 – American Solar Challenge 2012 – Rochester, NY to St. Paul, MN
- 2014 – American Solar Challenge 2014 – Austin, TX to Minneapolis, MN
- 2016 – American Solar Challenge 2016 – Brecksville, OH to Hot Springs, SD
- 2018 – American Solar Challenge 2018 – Omaha, NE to Bend, OR

### 2.1.3.- Emilia 4 project

Emilia 4 is the solar car designed and built by the University of Bologna that triumphed at the 2018 American Solar Challenge (figure 2.2).

After 2,700 kilometres from Nebraska to Oregon, being the only European team in the race, ended the ASC winning the first place. In addition, two special prizes have been given within this competition: the prize for the best mechanics and use of composites and the prize for the best battery project. [5]



Figure 2.2: Emilia 4 car. [6]

Developed and built in Emilia Romagna, Emilia 4 is 4.6 meter long, 1.8 meter wide and 1.2 meter high, it is equipped with a 5 square meter photovoltaic roof, made of 362 silicon cells, with a nominal power of 1200W. The cells lamination has been carried out by the Turin based company Solbian.

On this occasion, in addition to using the increasingly powerful cells supplied by SunPower, Solbian has transferred in the automotive field the latest developments already introduced for solar boats, in particular the company has chosen a combination of materials that can reduce the maximum weight of the photovoltaic system, while keeping the characteristics of resistance necessary in this type of competition intact.

Batteries included, the empty vehicle weights 230 kg and it can load 4 people and 2 luggages, namely 360 kg.

The car has an autonomy of 600 km without sun light at an average speed of 50-60km/h. Moreover, this car only uses solar energy without ever connecting to the electrical grid to recharge its batteries. [7]

The main phases of the construction of this car have been the following [8]:

- It has been started with a new design (as a result of an international competition of ideas) and has been continued with the creation of the CAD models, the execution of the many functional details for each component and then the structural and fluid dynamics analysis using FEM and SPH (smooth particle hydrodynamic) tools.
- After that, the prototyping of scale models, wind tunnel tests and multi-objective optimization of the geometries.
- Finally, vehicle construction is achieved thanks to unconventional techniques such as hybrid manufacturing solutions and the use of composite materials.

The design phase involved about 60 people and took two years, while construction was completed in less than a year.

## **2.2.- LIGHTWEIGHT WHEELS**

### **2.2.1.- Composite wheels**

Nowadays, composites are one of the most widely used materials due to its relative ease of combination with other materials and their adaptability to different situations to serve specific purposes.

In the automotive sector, the weight of cars has been increased continuously over time, in relation to improvements in driving aid systems, comfort and more passive safety requirements. Since 2000, as a consequence of increasing requirements on pollution emissions reduction, an important attention towards weight reduction in cars has been adopted. For this reason, the research of lightweight components has become one of the main challenges in the automotive industry. Traditionally, steel has been substituted by aluminium, but nowadays, carbon fiber-reinforced plastics (CFRP) technologies are a trend particularly important for the next generation of electric or hybrid vehicles. The market size for CFRP composites accounted for 20.3 \$ billion in 2014 and is projected to reach 35.8 \$ billion in 2020.[9]

Currently, composites are being considered to make safer, lighter and fuel-efficient vehicles. The weight of the carbon-fiber composites is about one-fifth compared with steel but are as good or in some cases better in terms of stiffness and strength. Moreover, these types of materials do not corrode or rust, which is a great advantage compared with metals like aluminium or steel.

However, the use of these materials has been limited due to the materials and manufacturing associated costs. For example, the material costs of carbon fiber composites are approximately 20 times more than the material costs using steel. For this reason, it has been done a great development in this area trying to make these materials more affordable [10].

#### **2.2.1.1.- Composite wheel characteristics**

In the particular case of the composite wheels, besides to help meeting the fuel economy goals of vehicle manufacturers, these types of materials offer other advantages:

- Reducing the wheel weight, the quality of vehicle ride is improved since the wheel is an unsprung component. The reduced weight shows improved vibrations when the vehicle is tested on rough roads.
- The manufacturing process of metal wheels may involve welding, stamping and forging. Eccentricity and runout defects can occur in these processes.

Since the composite wheels can be manufactured in molds which are made to precise dimensions, the wheels can be produced practically no runout or eccentricity.

- Since composite wheels can be molded in complex shapes, styling can be incorporated in the mold design. In contrast, in some cases, wheels using metal materials may require up to seven forming dies for styling.

On the other hand, composites wheels involve other design considerations than those for steel wheels.

- Material flow and stress distribution analysis require an optimum fiber orientation.
- The designer has limited freedom in varying thicknesses of stamped metal wheels since the rim and disk are normally made by stamping sheets of specified thicknesses. Furthermore, there is no incentive to obtain optimum thickness distribution due to the relatively low price of steel. With composite wheels, however, it is possible to vary thicknesses to obtain a minimum weight and uniform stress.
- Using pressure and heat during the molding process causes a movement of the fibers and the matrix in the mold. These conditions need to be analysed before arriving at a final wheel design.
- Classical stress analysis techniques are not adequate to determine deformations and stresses due to its complex shape. The finite element analysis is ideally suited for this purpose. In composite wheels, the thickness may be modified to achieve desired levels of stress that can be tolerated by the fiber-reinforced material. [11]

#### **2.2.1.2.- Wheels made of composite materials**

Manufacturing car composite wheels is not a novel idea. For this reason, in the following paragraphs, it has been compiled some examples of different wheels that have been made in the past and more recently, using composite materials.

During the 70s and 80s, the use of polymeric materials for wheels was tested. For example, in the 1970s, SMC (sheet moulding compound) wheels were made by Firestone (figure 2.3).[12]



Figure 2.3: Glass fiber reinforced SMC wheel produced by Firestone. [12]

In 1981, a composite wheel using fiber-reinforced plastic resin and the apparatus for construction have been made by James A. Woelfel. As it is described in the patent, “the wheel comprises a disc portion having reinforcing fibers in substantially random orientation disposed predominantly in planes perpendicular to the wheel axis, and a rim portion having directional first reinforcing fibers substantially parallel to each other and oriented circumferentially of or substantially parallel to the wheel axis, or both, and second reinforcing fibers which are substantially randomly oriented circumferentially of the wheel axis.”. Moreover, the method includes a detailed description of how the wheel is done using the different molds and the apparatus used to perform it (figure 2.4).[13]

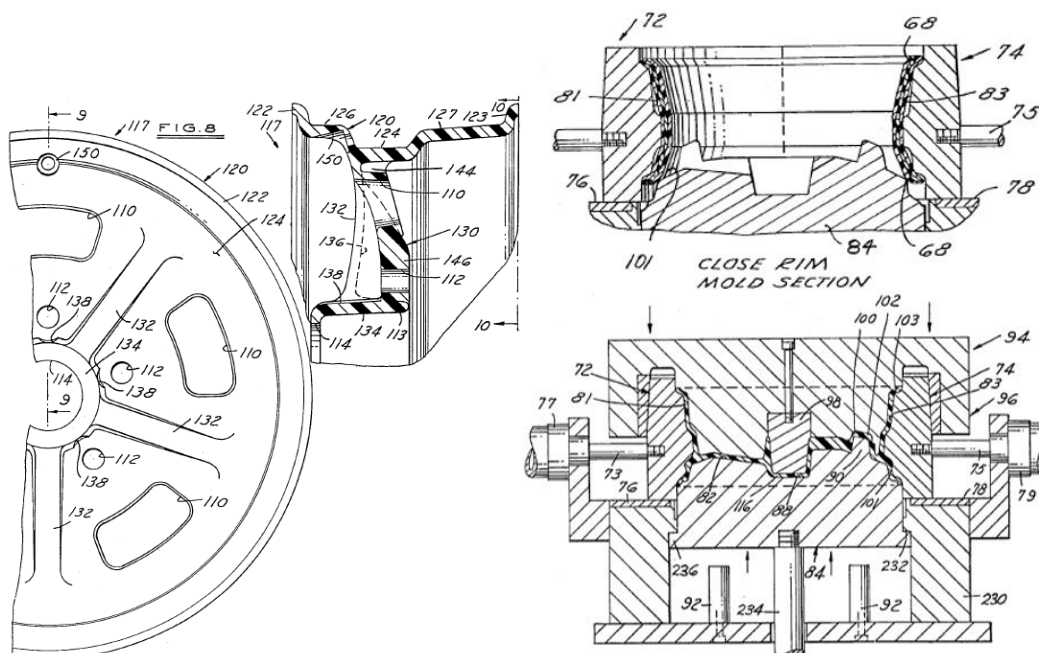


Figure 2.4: Shape of the composite wheel and the molds to produce it. [13]

In 1986, the Lancia ECV1 concept car has been presented at the Bologna Motorshow event (figure 2.5). This rally vehicle included composite materials to make the front wheel-rims. These wheels were the result of the collaboration between the racing department of Fiat-Abarth, Enichem and IDC with SPEEDLINE. The purpose of this research was to perform a wheel rim made from carbon fiber to withstand the extreme conditions which exist in a rally competition but also reducing the weight compared with traditional wheels. The results were weight savings of 40% with a total weight of 6 kg per wheel. [14]



Figure 2.5: Lancia ECV1 with the carbon-fiber rims. [14]

In 1988, Malcolm K. McDougall created a fiber reinforced plastic composite wheel and the corresponding method to manufacture it. This wheel (figure 2.6) includes a disc which comprising reinforcing fibers have been oriented in a radially outwardly extending direction. In addition, the wheel contains a rim piece which has a plurality of radially disposed and substantially distinct layers. Again, in this patent has been described all the process to obtain the composite wheel. [15]

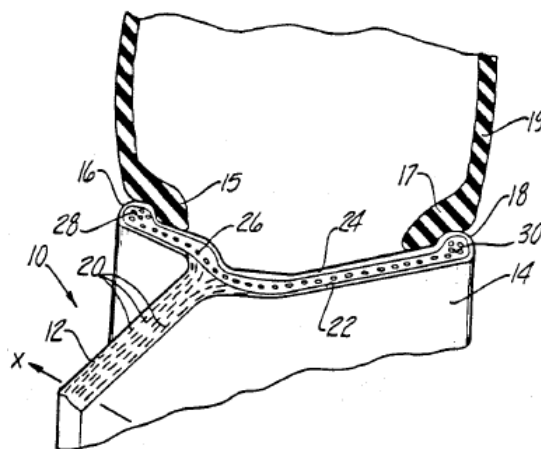


Figure 2.6: Detail of the composite wheel. [15]

In 2001 BTE Hybrid-Tech GmbH introduced SMC car wheels (figure 2.7). These wheels have successfully covered an approximate distance of 250000 km. The duration of the rotating bending moment tests reached approximately a factor of ten compared to the standard tests, for this reason, it was possible to demonstrate the great potential this material had. [12]



Figure 2.7: Glass fiber reinforced SMC wheel produced by BTE Hybrid-Tech GmbH, 2001. [12]

In 2013, Koenigsegg became the first automaker company to include carbon fiber wheels on a production car. The name of these wheels is Aircore and have been included in the auto maker's Agera R automobile (figure 2.8). These are made from pure carbon fiber with the hub and the spokes of the wheel constructed in one piece and being completely hollow. [16]



Figure 2.8: Aircore wheels used in Agera R car. [16]

More recently, an important composite wheel project has been supported by the European Union's Horizon 2020 research and innovation programme. This project is known as Carbon Rim Project (CARIM), and its purpose is to develop and commercialize a full CFRP wheel for SUV vehicles (figure 2.9) manufactured with an automated high-volume process for the market.

The actual developments in automated CFRP production technology will generate a wheel which is 30-50% lighter than the conventional aluminium wheels adding a better mechanical performance. The manufacture of these wheels is an innovative and automated HP-RTM process that reaches short cycle times and lower costs compared with the traditional technologies to produce conventional composite wheels. According to this, the target of this project is to reduce a 30% the weight of a conventional Al-wheel with a production rate of 20000 wheels per year. [17]



Figure 2.9: CARIM wheel. [17]

### 2.3.- MOTORWHEELS

Most car owners do not give much importance to elements such as wheels or tires. Despite this, there's a significant amount of technology, design and research that goes into making a good tire, but only two things normally come to mind when someone buys a new tire: the price and the time that will last.

However, in recent years, some tire companies and car manufacturers have been working to give greater importance to these elements. More specifically, placing the vehicle's power supply, as well as other integral parts of a functioning vehicle, inside the wheel. This concept is known as motorwheels and will revolutionize the future of transportation.

The basic principle of this concept is to replace the internal combustion engine usually found under the hood with at least two electric motors located in the hub of the wheels. The number of in-wheel motors a vehicle uses can be adapted to meet the vehicle requirements. In most cases, two motors supply enough power but, for example, an all-wheel-drive (AWD) vehicle requires four in-wheel motors. This type of electric motor is designed to work on full battery-operated vehicles, hybrid vehicles and even fuel-cell-powered electric vehicles. [18]

The principal challenge facing hub motors is the concern of unsprung weight. The unsprung mass (or unsprung weight) is the mass of all components that is not supported by the car's suspension. The mass of components such as the wheel hubs, wheel axles, wheel bearings suspension links and tires are included in the unsprung mass of a vehicle. This mass travels up and down over potholes, bumps and debris as it tries to follow the contour of the road, for this reason, designers try to minimize it. Using in-wheel motors, this weight is increased since the electric motor and other mechanical components are added inside the wheel. [19]

Below, some examples of in-wheel motors that are used in vehicles have been explained.

### **2.3.1.- Protean in-wheel motors**

Protean Electric is an automotive company specializing in in-wheel motor technology. Their technology creates a permanent magnet e-machine with relatively high torque and power density with the power electronics and controls packaged within the motor itself. [20]

Protean Electric transformed the Ford F-150 EV (figure 2.10) by removing the V8 engine and adding four in-wheel electric motors to the vehicle. Each of the four motors can deliver over 100 hp each, a total of 400 hp from all four motors (far more than produced by the standard V8 engine). Each motor gained power from a 42 kWh lithium-ion battery that provided the truck with a range of 161 kilometers before recharging. Another important characteristic is that, the weight of each motor is only 31 kilograms.[18]



Figure 2.10: Protean Ford F-150 All-Electric Pickup. [18]

### 2.3.2.- Michelin's Active Wheel

The Active Wheel (figure 2.11) is essentially a standard wheel that houses a pair of electric motors. One of these motors acts as an active suspension system to improve stability and comfort, while the other spins the wheel and transmits power to the ground. The system is designed for fuel-cell or battery powered electric vehicles. Moreover, using this technology, a vehicle will no longer need any clutch, gearbox, transmission shaft, anti-roll bar or universal joint.

Active Wheel's compact drive motor and integrated suspension system has also enabled designers to fit a standard brake disc between the motors, which means the braking, drive and suspension components are all fitted within the single wheel.

This system also allows to control electronically each individual wheel torque. The results are similar to the effects of an active differential, allowing to make much faster turns in poor conditions than traditional shaft-driven vehicles.

For the suspension, an actuator connected to a damping system with varying levels of firmness is controlled by an electric motor.

In addition, one benefit of Active Wheel technology is the advantages in passive safety. Since there is no need for a traditional engine in the front of the vehicle, this area can now be entirely dedicated to impact absorption.

This wheel has appeared on several concept cars but no actual production vehicles. [21]

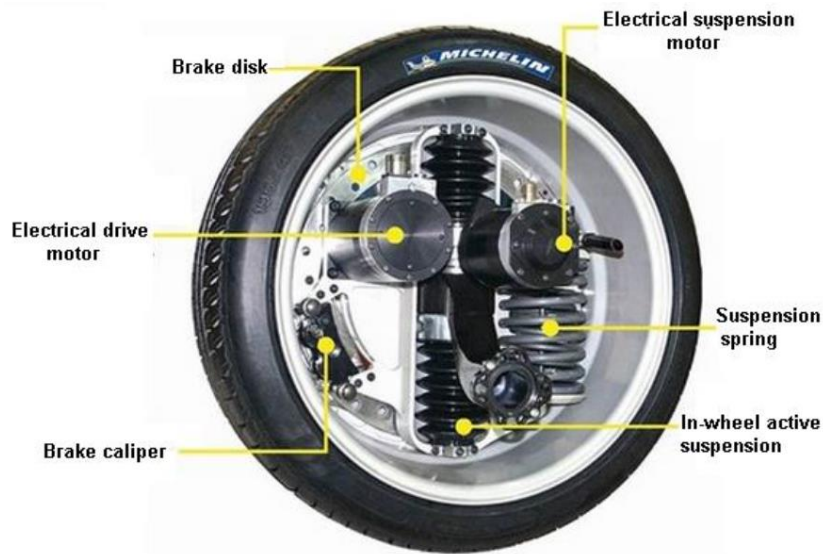


Figure 2.11: Michelin active wheel with in-wheel motor.[22]

### 2.3.3.- Fraunhofer hub motor

Researchers at Germany's Fraunhofer Institute have been working on a demonstration vehicle, the Frecc0 (Fraunhofer E-concept car Type 0), that was used to devise and evaluate all the components needed in an all-electric car (figure 2.12). One key component is the Fraunhofer hub motor.

The two motors used on the car's rear wheels are relatively light and compact, so they add little to unsprung masses weight. All motor's power electronics and control unit are in the hub. The motor provides enough torque at low speeds and puts out nearly constant power (55 kW and 700 Nm).

Individual components, as well as the assembled hub motor, have been tested to ensure they can withstand the vibrations shocks, and temperatures involved in daily driving.[23]

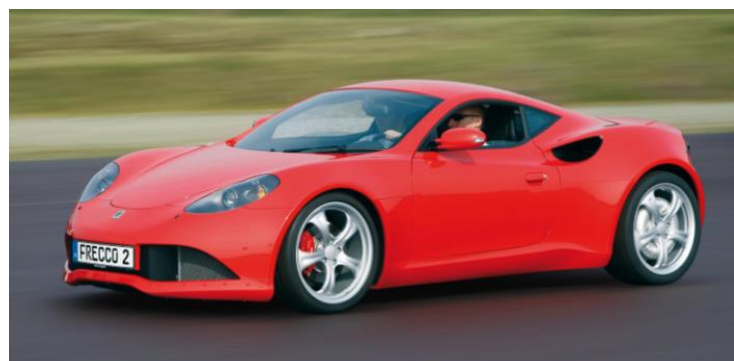


Figure 2.12: Frecc0 car. [24]

More recently, a CFRP composite wheel with integrated hub motor (figure 2.13) has been developed by this Institute [12]. The main development was to achieve the optimum in lightweight potential, considering structural durability. During this development process, some technical challenges of multifunctional design have been considered in the whole product life cycle.

The CFRP wheel has a size of 16.5 x 38.1 cm and a weight of approximately 3.5 kg (without the CFRP housing, motor components and metal parts such as screws or sleeves for bearing). The motor housing is directly connected to the inner area of the wheel axle. This prevents lateral or radial loads, especially shocks caused by kerbstone crossing or by a rough road, from being transferred to the hub motor.

Another advantage of the separation of the load paths is that the rim can be more flexible than if it were directly connected to the hub motor. To increase the flexural stiffness at a constant weight, foam cores are inserted into the spokes. A smaller, commercially available hub motor is used as the electrical motor.

The hub motor, consisting of a yoke ring with electromagnets (stator) and ring with permanent magnets (external rotor), has a drive voltage of  $2.0 \times 24.5$  V and a motor capacity of 4 kW.

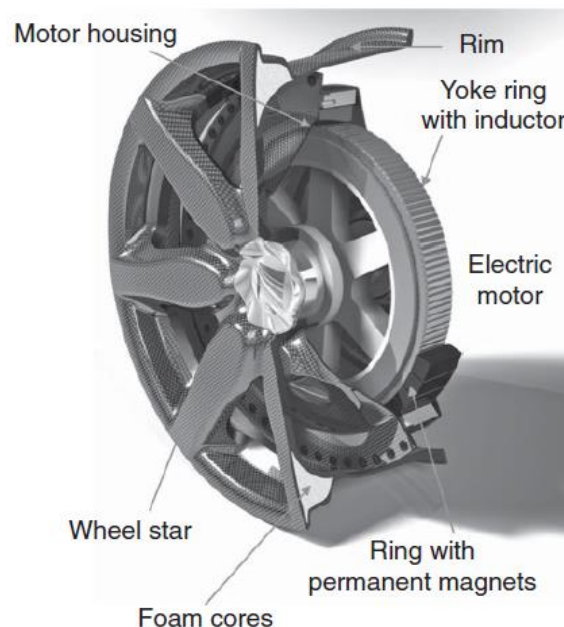


Figure 2.13: Section of the CFRP wheel with motor housing and integrated electrical motor. [25]

## 3.- DESIGN OF A LIGHTWEIGHT CFRP MOTORWHEEL

Optimization methods are techniques that enable the designers to obtain the optimal solution of a problem with the lowest possible computational cost. In the case of designing a composite wheel, these are widely used since there are a lot of variables involved in the composite's mechanical performance such as ply types, ply angles, number of plies, its disposition etc...

Below, two examples of these design optimization methods have been explained, but only the design of experiment has been carried out in this project. The purpose of this method is to obtain the optimal stacking sequence of the lenses that will be included in the new Emilia 4 motorwheel.

### 3.1.- DESIGN METHODS

#### 3.1.1.- Evolutionary algorithm

An evolutionary algorithm (EA) is a population-based metaheuristic optimization algorithm. An EA tries to imitate Darwin's "survival of the fittest" using mechanisms such as selection, reproduction, mutation and recombination but in an artificial simulation environment. The main procedure (figure 3.1) to perform this type of algorithm is written below:

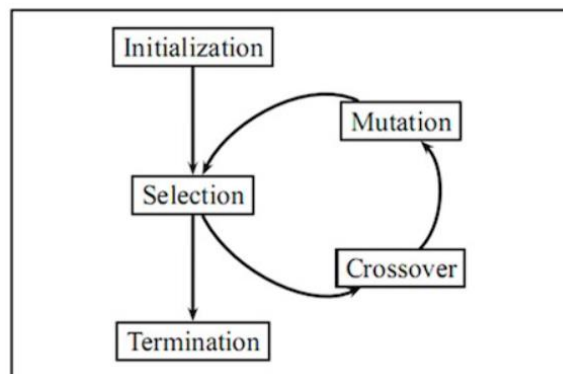


Figure 3.1: Basic elements of an evolutionary algorithm. [26]

- Initialization: the first step is to create an initial population of solutions. The population will have an arbitrary number of possible solutions (members). It is crucial to have a population that encompasses a wide range of solutions, in this way, the algorithm will explore more possible solutions.
  - Selection: once a population has been created, it is necessary to evaluate the members of the population according to a fitness function. A fitness function is a particular type of objective function which defines how close a design solution is to achieving the set aims. After that, the algorithm calculates the fitness of all members and select a portion of the top-scoring members.  
EAs allow also to use multiple fitness function. If a multiple fitness function is used, the algorithm will end up with a set of optimal points instead of identifying a single optimal point.
  - Genetic operators (crossover and mutation): after selecting the top members, a next generation in the algorithm is created using these members. Using the characteristics of the selected members (parents), new members (children) are created mixing the qualities of their parents. After that it is important to introduce “new genetic material” into the generation. If this step is not done, the algorithm will become stuck in local extrema, and therefore, optimal results won't be obtained.
  - Termination: At a certain point, the algorithm ends, obtaining the final solution.
- [26]

In the particular case of a composite wheel, this evolutionary optimization method has been used to develop composite fiber reinforced plastics (CFRP) motorcycle rims [27]. The purpose of the project was to obtain an optimal stacking sequence of the composite laminates, having an excellent compromise between the mass of the rims and some other parameters as strength or stiffness.

Below, it has been written a brief summary of this project explaining the specific working schedule of EA (figure 3.2) applied to optimize these rims:

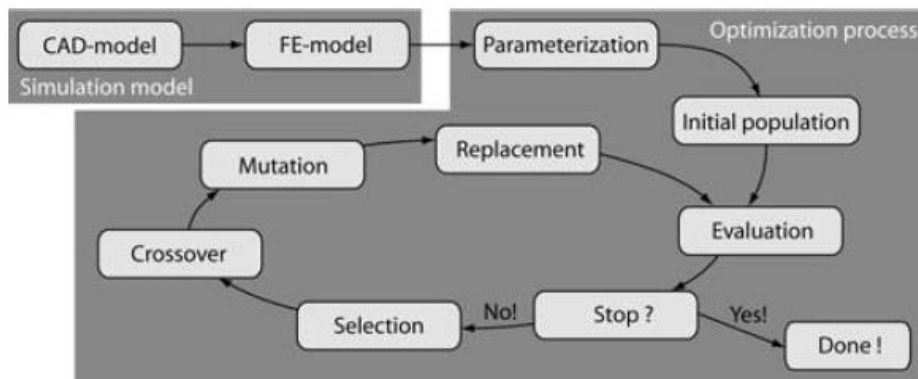


Figure 3.2: Working schedule of the EA applied. [27]

- Simulation model: Inside the CAD-model, the geometric shapes of the rims have been defined (figure 3.3). In this project, the shape of the motorcycle rims has been unchanged, only the stacking sequence of the composite laminate was altered.

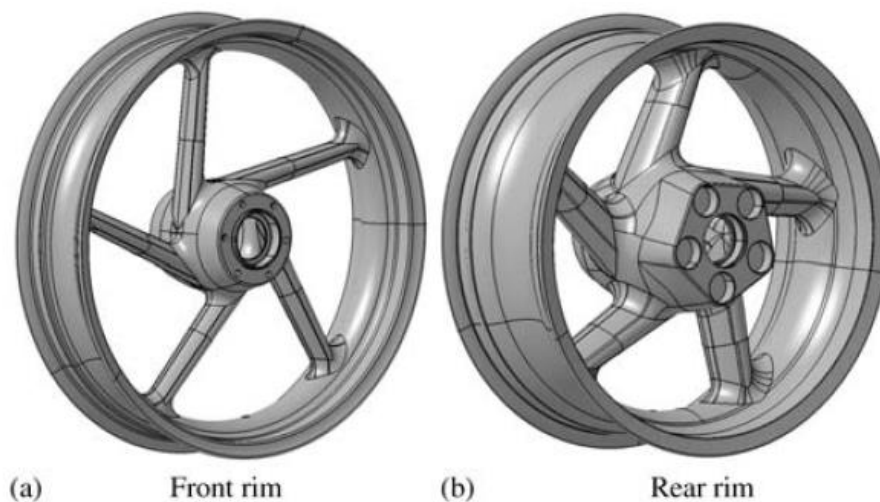


Figure 3.3: CAD models. [27]

In the FE-model, a lateral load case to prove the mechanical strength of the rims and the critical load case occurring during a race (maximum brake torque including the ground reaction) have been applied (figure 3.4).

To describe how this method works, only the front rim component has been explained.

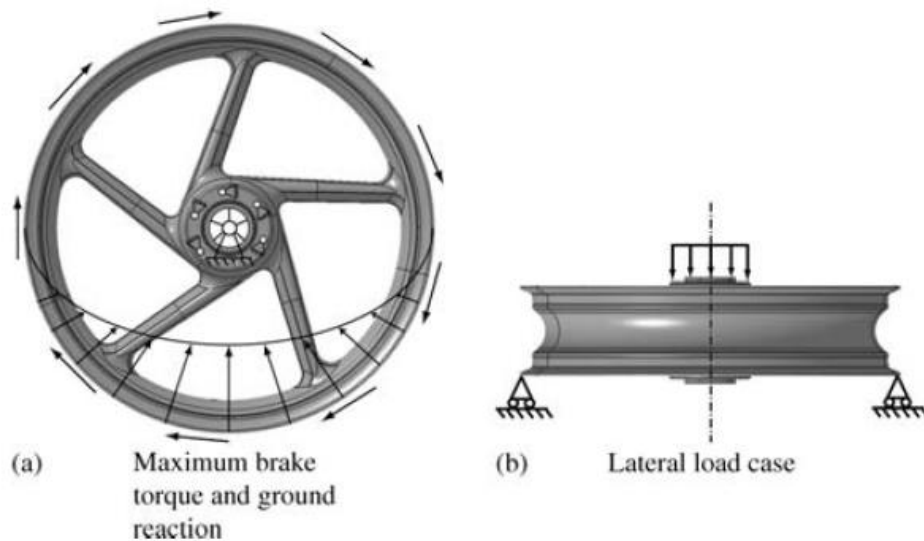


Figure 3.4: FE model load cases of the front rim.[27]

- Parameterization: There are three different parameters that describe the stacking sequence of this model:
  - The orientation of the plies.
  - The number of plies.
  - Different type of prepreg materials.

Using the eoUniGene software, the behaviour of these variables has been defined using different gene types:

- The Boolean gene determines whether a ply of the stacking sequence is active (true) or not (false).
- The const-float-list gene determines the orientation of the chosen prepreg material for each ply.
- The string-list gene identifies the material of a ply.
- The integer gene is needed to define the number of additional unidirectional reinforcement plies in specific locations of the rim.

In this project, it has been decided to divide the rim structure into four major domains (figure 3.5). Each domain will have a different stacking sequence.

The first domain includes the spokes and the hub, the second domain incorporates the rim bed, the third domain is defined as the overlap region between the first two domains and the fourth domain has the same base laminate as the first domain but

some additional unidirectional plies have to be applied to reinforce regions with high stresses.

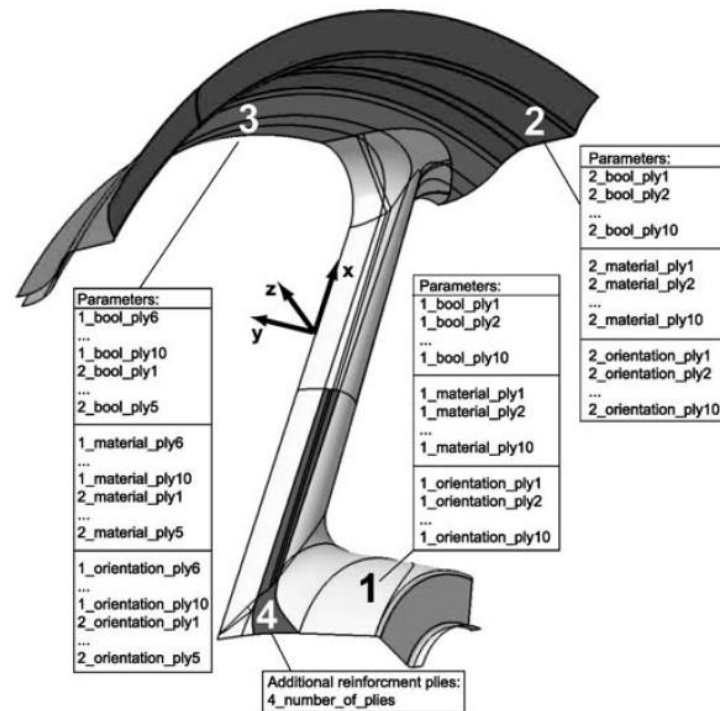


Figure 3.5: Four major domains of the rim. [27]

- Fitness function: The optimization objective has been performed as follows:

Minimize Mass

Subject to: Tsai – Wu index < 1

0.13 mm < Deflection value < 0.23 mm

The development in detail of these boundary conditions and the controlled optimization loop is explained in [27].

- Results

After some generations, convergence plots of the front optimization have been obtained (figure 3.6). In each plot, the best individual (best stacking sequence) within the population of each generation (all possible stacking sequences) has been represented. In addition, it has been represented the average value of the entire population of each generation.

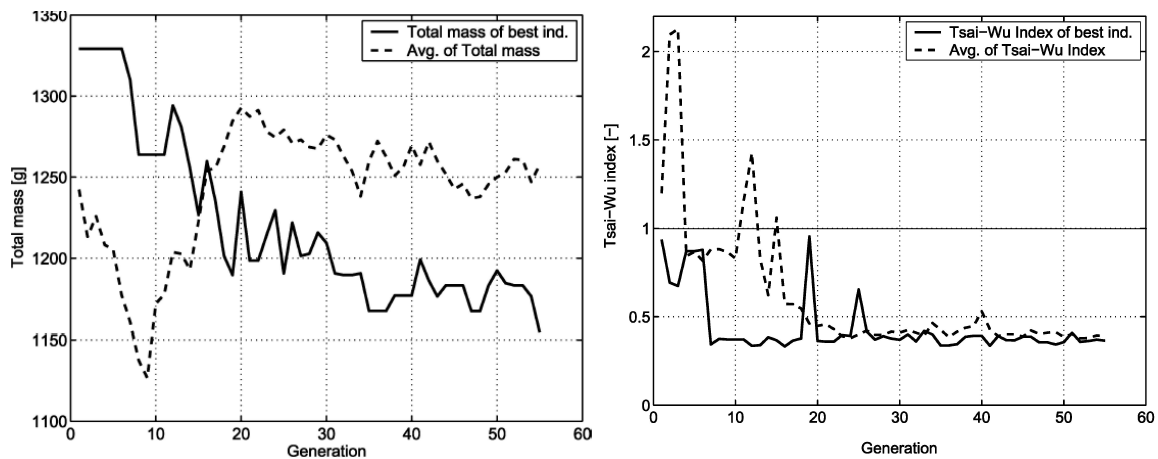


Figure 3.6: Convergence plots of the mass and the Tsai-Wu index in the front rim. [27]

As it can be observed in the results, as there is progress in the number of generations, the results obtained are more optimal. However, reaching a certain number of generations, the variation in the results is minimal.

### 3.1.2.- Design of experiment

Design of experiments (DOE) is defined as a branch of applied statistics deals with planning, conducting, analysing, and interpreting controlled tests to evaluate the factors that control the value of a parameter or group of parameters. This method allows to study the effect on the selected input parameters on a desired output response [28].

In this case, this method has been used to determine the optimal lens plybook using some constraints and objectives as it will be described later. The tool used to carry out this analysis is the Design Exploration which is a powerful approach used by DesignXplorer (figure 3.7) for designing and understanding the analysis response of parts and assemblies. It uses a deterministic method based on Design of Experiments (DOE) and various optimization methods, with parameters as its fundamental components [29].

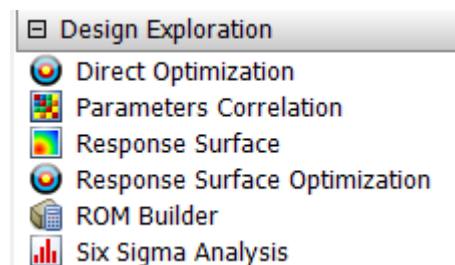


Figure 3.7: Design Exploration tools.

The first step to perform a DOE analysis is to decide the input and output parameters. Once these parameters have been determined, a parameters cell is added to the bus bar of the project. Depending on the type of input parameters selected in a model, there are two main ways to perform this analysis:

### DOE USING CONTINUOUS VARIABLES

This method also includes the cases in which the models have continuous and discrete input variables. In this case, a proper way to perform a DOE to optimize a model is to use the parameters correlation tool and the response surface optimization tool (figure 3.8):

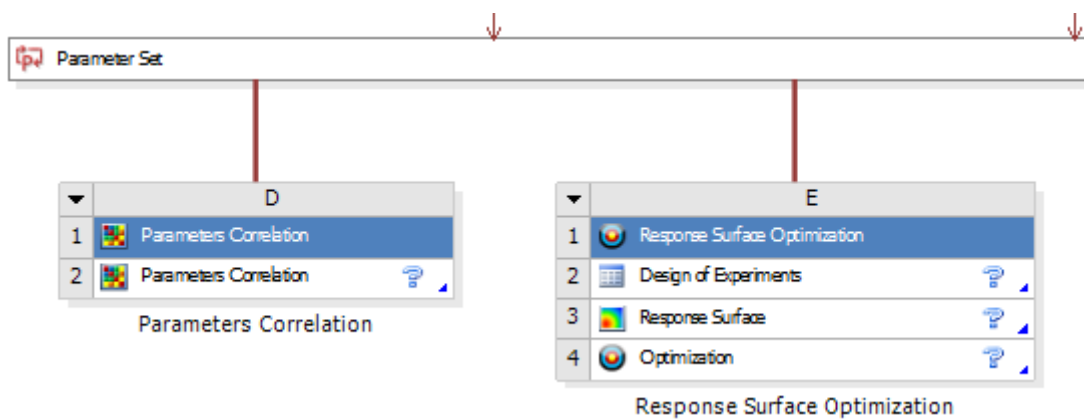


Figure 3.8: Project schematic of the design exploration.

#### - **Parameters Correlation**

This tool is useful to determine which of the selected input parameters in the first instance are truly important in the response of the system (output parameters). This means that it is possible to identify the key design parameters of a design and also to understand how some parameters are influenced by other parameters. Moreover, it must be considered that if the model has a greater number of input parameters, the increase in the number of design points can decrease the efficiency of the analysis process.

For example, inside this tool, the local sensitivity chart (figure 3.9) can be a powerful exploration tool. For each output, it allows to see the weight of the different input [30].

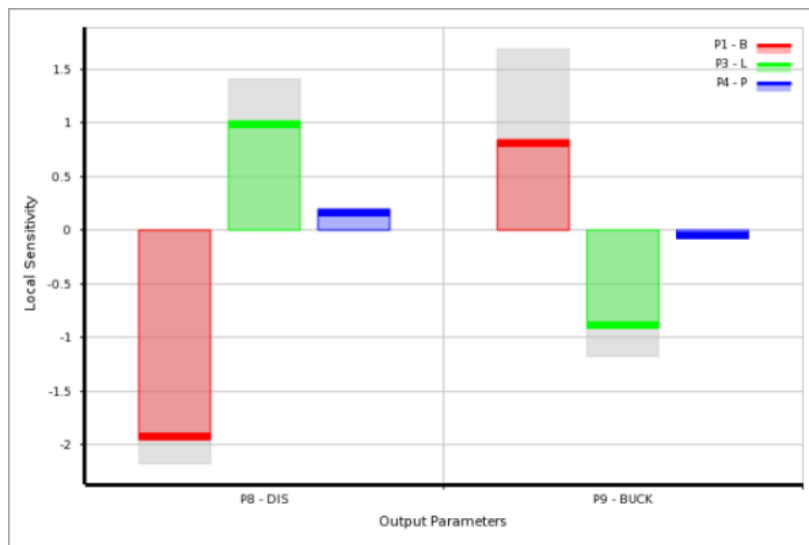


Figure 3.9: Example of a local sensitivity chart. [30]

As it can be seen in the previous figure, the third input parameter (blue) has a little influence in possible changes of the output variables. On the other hand, the sensitivities of the first and second parameter are high, which means, that a change in these input parameters has a great impact on the output parameters.

#### - Design of experiments

Design of Experiments (DOE) is a technique used to scientifically determine the location of sampling points and is included as part of the response surface, goal driven optimization, and analysis systems.

There are different DOE algorithms or methods included in this section. These techniques all have one common characteristic: they try to locate the sampling points such that the space of random input parameters is explored in the most efficient way or obtain the required information with a minimum of sampling points. Sample points in efficient location increase the accuracy of the response surface and reduce the required number of sampling points [31]. Depending on the model characteristics, the use of some specific DOE algorithms is recommended.

The Latin hypercube sampling (LHS) and Optimal space filling with user defined sample points are used the number of design points since the number of samples is independent from the number of parameters. [32]

Another more advanced choice is sparse grid, which only samples a few points initially and adaptively add new sample points based on the response surface. It is

recommended to use this method if the model is highly nonlinear. Kriging with auto-refinement has a similar effect.

In some cases, the Central composite design (CCD) is not recommended because requires a large number of samples for relatively small number of variables. [33]

#### - Response surface

This tool builds a response surface (figure 3.10) using the DOE design points' output and input values based on the chosen response surface type. In the response surface tab, it is possible to set the properties of the response surface algorithm, view several types of response charts and view the response points table [34].

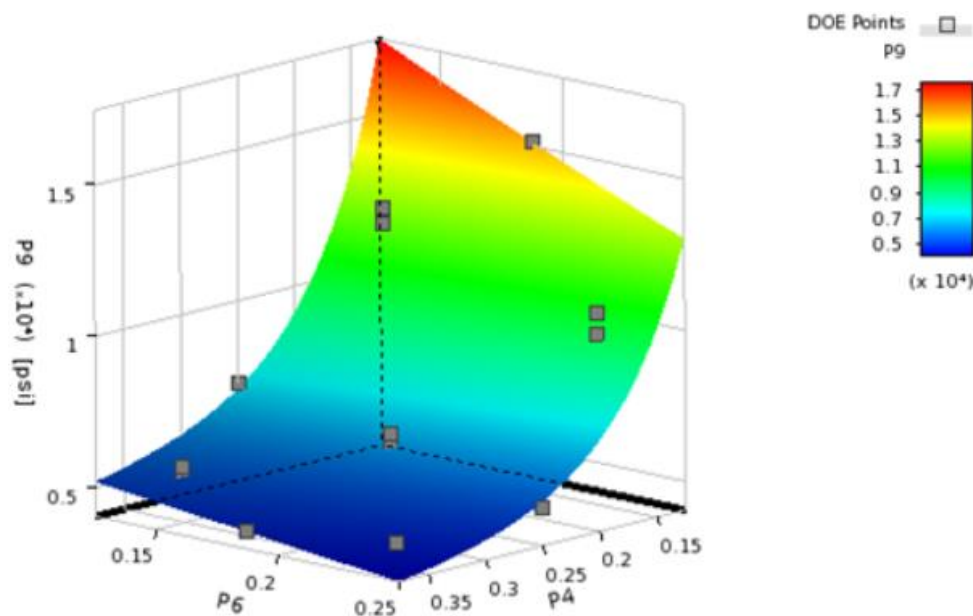


Figure 3.10: Response surface example. [35]

Below, as a summary, a small guide has been written about what response surface type should be used depending on the model characteristics:

- Standard response surface: It requires the least amount of computation in fitting and prediction. This method is useful when there is a lot of data and the change in objective is smooth.
- Kriging: This method is non-parametric, it is useful if the data is limited and highly nonlinear, and it is wanted that the model fits right through the data (i.e. the simulation results are trusted).

- Non-parametric regression: It is similar to Krigin in that the prediction depends on current data. It is used when the data is highly nonlinear and it is not necessary to fit right the model through the data.
- Neural network: if there is a high amount of non-linear data and it is not necessary to fit right the model through the data.
- Sparse grid: this method goes with the corresponding DOE method. This method can be used when the objective is highly nonlinear and it is not possible to afford many simulations. [36]

#### - **Optimization**

Using the data obtained from the DOE and the response surface, the program uses different algorithms to obtain the optimal solution for the model. It is possible to take multiple objectives, constraints and parameter relationships in the user interface. In addition, this tool tracks the progress of the optimization and shows different tables and charts which allow to evaluate tradeoffs and choose a solution from the design candidates. [37]

### **DOE USING DISCRETE VARIABLES**

#### - **Direct optimization**

This method uses actual analysis results which are solved sequentially during the optimization. It is important to consider that the sample design points are selected based on the actual optimization goal. In this way, the sample data is regenerated if the optimization goal is changed.

In a general case, it is better to use the Response Surface approach, which has several advantages with respect to the direct optimization method [38]:

- In a response surface optimization, the DOE method predetermines the number of design points required.
- The response surfaces can be used for multiple optimizations since they are not connected to a particular optimization goal.
- Knowing the design point definitions before the optimization process allows the response surface to take advantage of parallel computing.

Despite this, if a model only has discrete input variables, it is not necessary to use the response surface optimization. A simple way to work these types of variables is to use a simple optimization.

For this reason, it has been decided to use only the direct optimization tool (figure 3.11) including several number of combinations between these variables and select the best candidate point obtained.

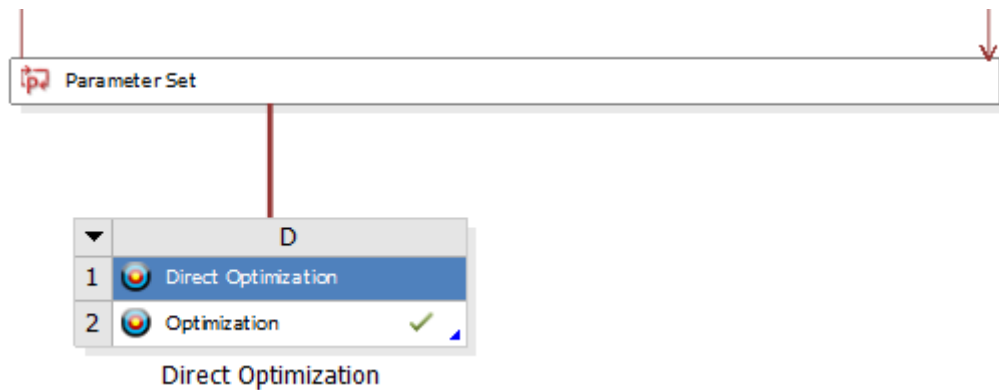


Figure 3.11: Project schematic of the direct optimization.

Inside direct optimization, there are different goal driven optimization methods (table 3.1): [39]

- Screening: this method is based on the Shifted-Hammersley sampling.
- NLPQL: this method is based on the nonlinear programming by quadratic Lagrangian.
- MISQP: is based on the mixed-integer sequential quadratic programming.
- MOGA: is a multi-objective genetic algorithm.
- Adaptive single-objective: is a hybrid optimization method with a domain reduction in direct optimization system.
- Adaptive multiple-objective: hybrid optimization method using Kriging response surface in a direct optimization system.

Method	Single Objective	Multiple Objectives	Local Search	Global Search	Discrete	Manufacturable Values	Parameter Relationships
Screening		X		X	X	X	X
NLPQL	X		X				X
MISQP	X		X		X	X	X
MOGA		X		X	X	X	X
Adaptive Single-Objective	X			X		X	
Adaptive Multiple-Objective		X		X		X	X

Table 3.1: General capabilities of each method within direct optimization. [39]

As it will be explained later, to determine the optimum stacking sequence of the rim, a multi-objective optimization using discrete variables has been done. Considering these conditions, only two methods could be used: screening and MOGA. In this case, since all the variables are discrete, there is no information that determines which method is the most suitable for this application. For this reason, it would be possible to use any of them.

### 3.2.- STANDARDS

To identify the loads and constraints to be considered to study the wheel using FEM tools, two international standards for wheel approvals have been taken as reference: the TÜV E/ECE 324 [40] and the Jaso standard [41].

Despite this, only the calculations of the test loads using the TÜV standard, have been done to know the performance of the composite wheel.

#### 3.2.1.- TÜV E/ECE 324

This standard concerns the adoption of uniform provisions concerning the approval of wheels for passenger cars and their trailer [40]. It must be considered that this standard is used for commercial wheels and does not consider the special case of the custom wheels. Despite this, it is useful as a reference to obtain the value of the forces acting on a wheel during tests following a standard procedure.

Within this standard, as it can be seen later, some tests have been considered to know the loads acting on the wheel and its performance.

### 3.2.1.1.- Rotating bending test

During the rotating bending test, the lateral forces acting on wheel in driving around a curve are simulated. The wheel rim is fixed rigidly to the test bench, and a bending moment  $M_b$  is applied to the hub mounting area (figure 3.12):

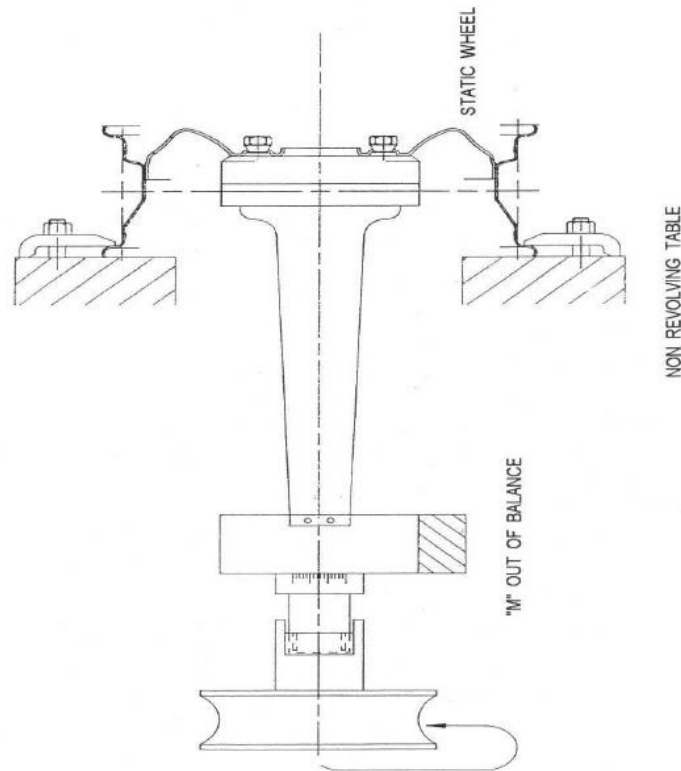


Figure 3.12: Example of a rotating bending test ring. [40]

The formula for the bending moment calculation is:

Cars and off-road vehicles:  $M_{bmax} = S * F_v (\mu * r_{dyn} + d)$

- $M_{bmax}$  = maximum reference bending moment [Nm]
- $F_v$  = maximum load capacity of wheel [N]
- $r_{dyn}$  = dynamic radius of largest tyre recommended for wheel [m]
- $d$  = inset [m]
- $\mu$  = coefficient of friction (0.9)
- $S$  = factor of safety (2)

As it is explained in this standard, this test has to be performed using four wheels, two at 50 per cent and two at 75 per cent of the maximum moment  $M_{bmax}$ . However, for this project, this test only will be simulated with a static structural FEM analysis using the maximum bending moment  $M_{bmax}$ .

### 3.2.1.2.- Rolling test

In the rolling test (figure 3.13) the stress on the wheel when driving straight ahead is simulated by testing a wheel rolling against a drum which has a minimum outside diameter of 1.7 m, in the case of an external rolling test, or a minimum internal diameter equal to the dynamic radius of the tyre divided by 0.4 in the case of an internal rolling test. Two wheels shall be tested.

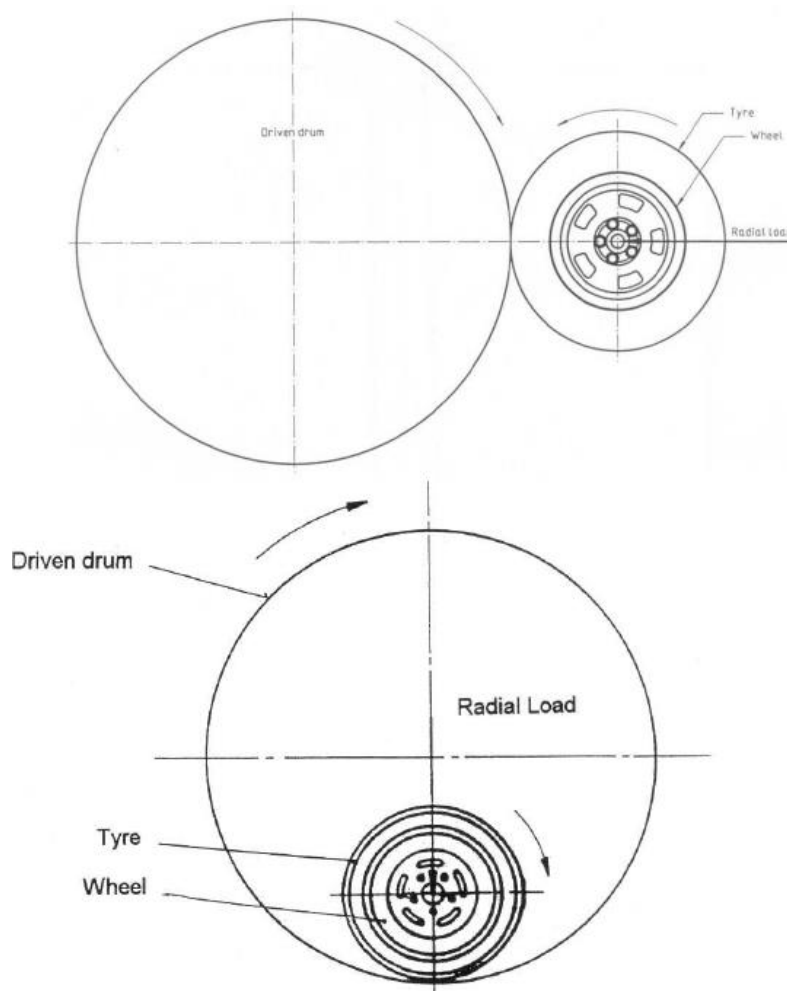


Figure 3.13: Examples of rolling test rigs. [40]

The formula used to calculate the test load is:

All type of vehicles:  $F_p = S * F_v$

- $F_p$  = testing load [N]
- $F_v$  = wheel maximum load capacity of the wheel [N]
- $S$  = factor of safety

### 3.2.1.3.- Impact test

This test evaluates the wheel strength with regard to the fractures on edges and other critical points when the wheel strikes an obstacle. To perform this test, the wheel and the tyre have to be mounted in the test machine (figure 3.14) such that the impact loading is applied to the rim flange of the wheel.

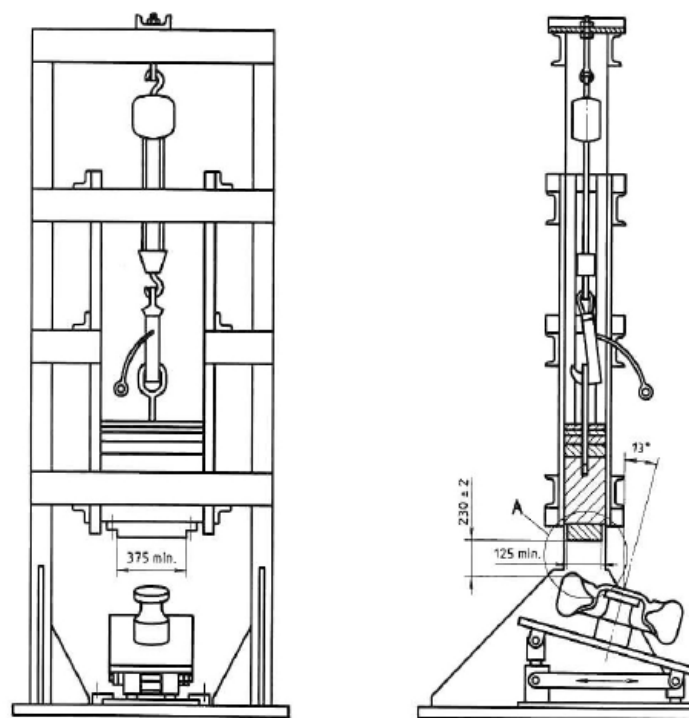


Figure 3.14: Impact loading test machine. [40]

The formula used to calculate the test load is:

$$D = 0.6 * F_v / g + 180 \text{ [kg]}$$

- $D$  = value of falling mass [kg]
- $F_v$  = maximum wheel load capacity [N]
- $g$  = acceleration due to gravity  $9.81 \text{ m/s}^2$

### 3.2.1.4.- Alternating torque test

In an alternating torque test the torque acting on wheel during braking and acceleration is simulated. The sample wheels shall be tested at each percentage value (50 per cent and 75 per cent) of the maximum calculated torque. Each wheel flange is rigidly fixed on the test

table and stressed by an alternating torque of  $\pm M_T$ , introduced through the attachment face i.e. through a brake disc or through other components.

The formula used to calculate the test load is:

$$M_T = S * F_V * r_{dyn}$$

Where:

- $M_T$  = test torque [Nm]
- $S$  = factor of safety (1)
- $F_V$  = maximum wheel load capacity [N]
- $r_{dyn}$  = dynamic radius [m]

In this case, this test will be simulated using a static structural FEM simulation considering  $M_T$  as the torsion moment acting on the wheel.

### 3.3.- EMILIA 4 WHEELS

In this section, as it can be seen later, the forces acting on the wheel have been calculated. The first step before doing any calculation is to collect all the input data about the vehicle, as mass, dimensions etc.. (table 3.2).

Mass		
Vehicle mass (estimated at 01/2019):	400	[kg]
Person mass + ballast (75 + 5 kg):	80	[kg]
Number of passengers:	4	[-]
Total mass 4 passengers + 4 ballast:	320	[kg]
Total mass "m ":	720	[kg]
Dimensions		
Front width $c_a$ :	1352	[mm]
Rear width $c_p$ :	1222	[mm]
Step $l$ :	2770	[mm]
Semistep $a1 = a2$ :	1385	[mm]
Height of the mass center $h_{cg}$ :	510	[mm]
Distribution of loads		
Front % $C_a$ :	50%	[%]
Rear % $C_p$ :	50%	[%]

Table 3.2: Principal dimensions and parameters of the Emilia 4 vehicle.

After that, it is important to determine the characteristics of the wheel. The rim used in this vehicle is the WSC Michelin tire 95-80 R16 [42]. This rim is only used to produce custom wheels for solar races on public roads and these are its characteristics (table 3.3):

Tires (3.00 B16 from Michelin Datasheet)		
Size:	16.0	[inch]
Tread width:	3.0	[inch]
Overall Diameter:	558.0	[mm]
Theoretical radius:	279.0	[mm]
Radius of contact "r":	279.0	[mm]
Max. lateral grip (real) without aerodynamic load " $\mu_{\tau}$ ":	0.6	[-]
Max. longitudinal grip (real) without aerodynamic load " $\mu_l$ ":	0.9	[-]
Max. combined grip (real) without aerodynamic load " $\mu_c$ ":	0.61	[-]
Tire (3.00 B16 from Datasheet Michelin)		
Diameter:	16.0	[inch]
Width:	3.0	[inch]
Offset "ET":	44.0	[mm]

Table 3.3: WSC Michelin tire 95-80 R16 characteristics.

In addition, as it can be seen in the previous table, it has been included the value of the maximum lateral grip and maximum longitudinal grip. These coefficients have been obtained directly from some tests using an accelerometer in the previous version of the vehicle. On the other hand, the maximum combined grip has been assumed as the 68% of the value of the maximum longitudinal grip.

The second step of the process is to determine the maximum vertical force acting on the tire. To obtain this value, it is necessary to consider two different situations, when the car is braking and when is taking a curve. After comparing both situations, the higher maximum vertical force of these two cases has been chosen to perform the following calculations.

In table 3.4 and table 3.5, all the calculations to obtain this vertical force for both models are shown:

<b>Braking</b>		<b>0.9 g</b>
Max achievable deceleration $a_{max} = \mu_l \times g$		8.8 [m/s <sup>2</sup> ]
Load transfer $\Delta z_f = m h_{cg} a_{max}/l$		1170 [N]
<b>Maximum axle loads:</b>		
Front $F_a = m g a1/l + \Delta z_f$		4700 [N]
Rear $F_p = m g a2/l - \Delta z_f$		2360 [N]
<b>Weight distribution during braking:</b>		
Front $F_a/(m g)$ :		66.6% [%]
Rear $F_p/(m g)$ :		33.4% [%]
Force acting on a single tire (assuming a uniform rectilinear motion):		
Front $F_{v\_ant} = F_a/2$		2350 [N]
Rear $F_{v\_post} = F_p/2$		1180 [N]
<b>Maximum components of the forces acting on the tire:</b>		
Tire		Front [-]
<b>Vertical</b> $F_v$		<b>2350 [N]</b>
<b>Longitudinal</b> $F_l = F_v * \mu_l$		<b>2115 [N]</b>
<b>Transversal</b> $F_t = F_v * \mu_t$		<b>1410 [N]</b>
Load transfer from rear to front:		
<b>CTC_F = coeff load transfer during braking</b>		<b>16.6% [%]</b>

Table 3.4: Calculations of the forces acting on the tire during braking.

<b>Curve</b>		<b>0.6 g</b>
Maximum lateral acceleration before slipping $a_{lat\ max} = \mu_t \times g$		5.9 [m/s <sup>2</sup> ]
Front axle load transfer $\Delta z_{ca} = m h_{ca} \%Ca a_{lat\ max}/c_a$		799 [N]
Rear axle load transfer $\Delta z_{cp} = m h_{ca} \%Cp a_{lat\ max}/c_p$		884 [N]
<b>Maximum loads on the two halves of the vehicle:</b>		
Exterior front curve $F_{e\_a} = m g \%Ca (ca/2)/ca + \Delta z_{ca}$		2564 [N]
Interior front curve $F_{i\_a} = m g \%Ca (ca/2)/ca - \Delta z_{ca}$		966 [N]
Exterior rear curve $F_{e\_p} = m g \%Cp (cp/2)/cp + \Delta z_{cp}$		2649 [N]
Interior rear curve		881 [N]
Exterior curve $F_e = F_{e\_a} + F_{e\_p}$		5213 [N]
Interior curve $F_i = F_{i\_a} + F_{i\_p}$		1847 [N]

**Weight distribution in curve:**

Exterior	$Fe/(m\ g):$	73.8%	[%]
Exterior front	$Fe\_a/(m\ g):$	36.3%	[%]
Exterior rear	$Fe\_p/(m\ g):$	37.5%	[%]
Interior	$Fi/(m\ g):$	26.2%	[%]
Interior front	$Fi\_a/(m\ g):$	13.7%	[%]
Interior rear	$Fi\_p/(m\ g):$	12.5%	[%]

Load on individual external tires (assuming a uniform rectilinear motion):

Front	$Fv\_ant = Fe\_a$	2564 [N]
Rear	$Fv\_post = Fe\_p$	2649 [N]

**Maximum components of the forces acting on the tire**

Tire		Rear [-]
<b>Vertical</b>	<b><math>Fv</math></b>	<b>2649 [N]</b>
<b>Longitudinal</b>	<b><math>Fl = Fv * \mu_l</math></b>	<b>2384 [N]</b>
<b>Transversal</b>	<b><math>Ft = Fv * \mu_t</math></b>	<b>1590 [N]</b>

Load transfer from inside to outside curve:

<b>CTC_C = coeff load transfer in curve</b>	<b>23.8% [%]</b>
---	------------------

Table 3.5: Calculations of the forces acting on the wheel during a curve.

After comparing both situations, the most solicited one happens when the car is taking a curve. The summary of the output values considered to perform future calculations are shown in (table 3.6).

Summary	
$Fv$ = Maximum vertical force acting on the tire	2649 [N]
Corresponding load type	Curve
g-Force	0.6 g
Tire	Rear

Table 3.6: Summary of the values obtained from the curve case.

After obtaining the maximum possible value of the vertical force acting on the tire, the test loads have been calculated using the TÜV E/ECE 324 standard as it has been explained in the previous section. (table 3.7).

**1 - Rotating bending test**

<b><math>Mf_{max} = k1 * Fv * (\mu_t * r + ET) =</math></b>	<b>1120 [Nm]</b>
---	------------------

k1 = safety factor:	2.0 [-]
Fv = wheel static load (vertical load):	2649 [N]

*Fatigue test for TÜV*

50% $Mf_{max}$ =	560 [Nm]
75% $Mf_{max}$ =	840 [Nm]

Notes

For TÜV:  $Fv = 650$ [kg]  
 For TÜV:  $\mu_t = 0.9$

**2 - Rolling test**

<b><math>Fp = Fv * k2</math></b>	<b>6623 [N]</b>
----------------------------------	-----------------

k2 = safety factor:	2.5 [-]
Fv = wheel static load (vertical load):	2649 [N]

**3 - Impact test**

<b><math>D = 0.6 * Fv / g + 180</math> [kg] =</b>	<b>3355 [N]</b>
---	-----------------

Fv = wheel static load (vertical load):	2649 [N]
---	----------

**4 - Alternating torque test**

<b><math>Mt = k3 * Fv * r =</math></b>	<b>739 [Nm]</b>
--	-----------------

k3 = safety factor:	1.0 [-]
Fv = wheel static load (vertical load):	2649 [N]

Table 3.7: Test loads obtained using the TÜV E/ECE 324 standard.

To perform the FEM simulations, it has been decided to make some changes in the values of some TÜV tests in addition to do other tests that are not included within this standard.

As it is said before, this standard is used for standard wheels, that is why, the safety factors applied in some cases are very high. For this reason, as it can be seen in table 3.8, the value of the safety factor used in the calculation formula of the bending moment has been changed. This safety factor has been reduced to 1.3 obtaining a maximum bending moment of 728 Nm.

**1 - Rotating bending test (modified from TÜV E/ECE 324)**

<b>Mf_max = k1 * Fv * (μt * r + ET) =</b>	<b>728 [Nm]</b>
k1 = safety factor:	1.3 [-]
Fv = wheel static load (vertical load):	2649 [N]

*Fatigue test for TÜV*

50% Mf_max =	364 [Nm]
75% Mf_max =	546 [Nm]

Table 3.8: Bending moment test modified from TÜV E/ECE 324

In the rolling test, the value of the test load has not been changed, but the value of the tire inflation pressure has been also considered (table 3.9). The effect of this pressure acting on the tire will be explained in detail later.

**2 - Rolling (modified from TÜV E/ECE 324)**

<b>Fp = Fv * k2</b>	<b>6623 [N]</b>
<b>Tyre inflate pressure p_max</b>	<b>8 [bar]</b>
	<b>p0 = 0.8 [MPa]</b>
	<b>pf = 10.2 [MPa]</b>
k2 = safety factor:	2.5 [-]
Fv = wheel static load (vertical load):	2649 [N]

Table 3.9: Rolling test modified from TÜV E/ECE 324.

In the case of the impact test, it has been decided to perform a different test from the one that is described in the TÜV standard (table 3.10). It has been assumed that the vehicle is subjected to an acceleration of 6g vertical (on both sides of the rim) and a 3g acceleration in the lateral direction (only on one side of the rim), both considering 1/3 of the rim. In addition, the presence of the internal inflation pressure has been included (during uniform straight motion).

**3 - Impact (rev CD - vehicle dynamic)**

<b>Vertical acceleration</b>	<b>6 g</b>
	58.8 [m/s <sup>2</sup> ]
Vertical inertial force in the vehicle $F_{i\_vtot}$ :	42365 [N]
<b>Vertical inertial force on the tire <math>F_{i\_v}</math> :</b>	<b>10591 [N]</b>
<b>Horizontal acceleration</b>	<b>3 g</b>
	29.4 [m/s <sup>2</sup> ]
Horizontal inertial force in the vehicle $F_{i\_htot}$ :	21182 [N]
<b>Horizontal inertial force on the tire <math>F_{i\_h}</math> :</b>	<b>5296 [N]</b>
<b>Nominal tire inflate pressure</b>	<b>5 [bar]</b>
	$p_0 = 0.5$ [MPa]
	$p_f = 6.4$ [MPa]

Table 3.10: Impact test considering the dynamics of the vehicle.

The value of the torsion load in the alternating torque test has been modified considering that the load that is transmitted to the rim is the 90% of its maximum value ("M<sub>t</sub>" load in the TÜV), taking into account the value of the maximum longitudinal grip " $\mu_1$ " (table 3.11).

**4 - Torsion (rev CD - vehicle dynamic)**

<b>Mt = k4 * FI * r =</b>	<b>665 [Nm]</b>
k4 = safety factor:	1.0 [-]
FI = longitudinal load (Fv * $\mu_1$ ):	2384 [N]

Table 3.11: Torsion test considering the dynamics of the vehicle.

In addition to the previous tests, it has been also decided to include a to analyse the wheel performance when the vehicle takes a curve, since, as it has been explained previously, this is the case where the wheel suffers the most load conditions (table 3.12).

<b>6 - Curve loads (rev CD - vehicle dynamic)</b>		<b>0.6 g</b>
<b>F<sub>v</sub></b> (vertical force) =		<b>2649 [N]</b>
<b>F<sub>l</sub></b> (longitudinal force) =		<b>2384 [N]</b>
<b>F<sub>t</sub></b> (transversal force) =		<b>1590 [N]</b>
<b>Tyre inflate pressure during normal functioning</b>		<b>5 [bar]</b>
	<b>p<sub>0</sub> =</b>	<b>0.5 [MPa]</b>
	<b>p<sub>f</sub> =</b>	<b>6.4 [MPa]</b>

Table 3.12: Loads acting on the wheel during a curve.

As a summary, in table 3.13, the value of the test loads that are included to perform the static structural simulations using FEM tools are shown:

<b>1 - Rotating bending test (modified from TÜV E/ECE 324)</b>	
<b>M<sub>f_max</sub> = k<sub>1</sub> * F<sub>v</sub> * (μ<sub>t</sub> * r + ET) =</b>	<b>728 [Nm]</b>
k <sub>1</sub> = safety factor:	<b>1.3 [-]</b>
F <sub>v</sub> = wheel static load (vertical load):	<b>2649 [N]</b>
<i>Fatigue test for TÜV</i>	
50% M <sub>f_max</sub> =	<b>364 [Nm]</b>
75% M <sub>f_max</sub> =	<b>546 [Nm]</b>
<b>2 - Rolling (modified from TÜV E/ECE 324)</b>	
<b>F<sub>p</sub> = F<sub>v</sub> * k<sub>2</sub></b>	<b>6623 [N]</b>
<b>Tyre inflate pressure p<sub>max</sub></b>	<b>8 [bar]</b>
	<b>p<sub>0</sub> = 0.8 [MPa]</b>
	<b>p<sub>f</sub> = 10.2 [MPa]</b>
k <sub>2</sub> = safety factor:	<b>2.5 [-]</b>
F <sub>v</sub> = wheel static load (vertical load):	<b>2649 [N]</b>

**3 - Impact (rev CD - vehicle dynamic)**

<b>Vertical acceleration</b>	<b>6 g</b>
	58.8 [m/s <sup>2</sup> ]
Vertical inertial force in the vehicle $F_{i\_vtot}$ :	42365 [N]
<b>Vertical inertial force on the tire <math>F_{i\_v}</math>:</b>	<b>10591 [N]</b>
<b>Horizontal acceleration</b>	<b>3 g</b>
	29.4 [m/s <sup>2</sup> ]
Horizontal inertial force in the vehicle $F_{i\_htot}$ :	21182 [N]
<b>Horizontal inertial force on the tire <math>F_{i\_h}</math>:</b>	<b>5296 [N]</b>
<b>Nominal tire inflate pressure</b>	<b>5 [bar]</b>
	$p_0 = 0.5$ [MPa]
	$p_f = 6.4$ [MPa]

**4 - Torsion (rev CD - vehicle dynamic)**

<b><math>M_t = k_4 * F_l * r =</math></b>	<b>665 [Nm]</b>
$k_4 =$ safety factor:	1.0 [-]
$F_l =$ longitudinal load ( $F_v * \mu_l$ ):	2384 [N]

**6 - Curve loads (rev CD - vehicle dynamic)**

<b><math>F_v</math> (vertical force) =</b>	<b>2649 [N]</b>
<b><math>F_l</math> (longitudinal force) =</b>	<b>2384 [N]</b>
<b><math>F_t</math> (transversal force) =</b>	<b>1590 [N]</b>
<b>Tyre inflate pressure during normal functioning</b>	<b>5 [bar]</b>
	$p_0 = 0.5$ [MPa]
	$p_f = 6.4$ [MPa]

Table 3.13: Loads included to perform the wheel FEM simulations.

To perform the simulations, the bending moment value has been rounded from 728 Nm to 730 Nm and the torque moment in the TÜV test, from 739 Nm to 740 Nm.

Otherwise, to study only the behaviour of the rim, it is necessary to know the distribution of pressure in the tire. This will be useful, as it will be described later, to determine the optimal stacking sequence of the rim. These results have been obtained using a paper which explains the influence of pressure on different elements of a wheel [43].

As it can be observed in figure 3.15, the air pressure inside the tire, acts against its sidewall, generating an axial load. This depends on the specific geometry of each rim. This axial force  $F_p$ , that results from the inflation pressure  $P_0$ , is estimated from the following relationship:

$$F_p = \pi(a^2 - r_f^2)P_0$$

Where  $r_f$  is the radius of the loading point on the rim flange and  $a$  is the inner radius of the tire. For the calculation of this force, to increase the safety factor, the parameter  $a$  has been considered as the external radius of the tire. In this way, the force value obtained is greater than the theoretical one.

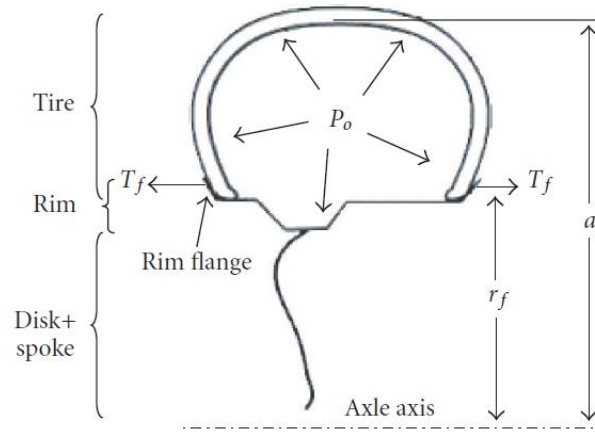


Figure 3.15: A schematic showing the load induced by tire inner pressure. [43]

Since axial load is supported by the flange of the rim and the tire tread, approximately half of the load is assumed to be borne by each part. In this way, the load on a unit length of the circumference of the rim flange  $T_f$  is obtained using the following expression:

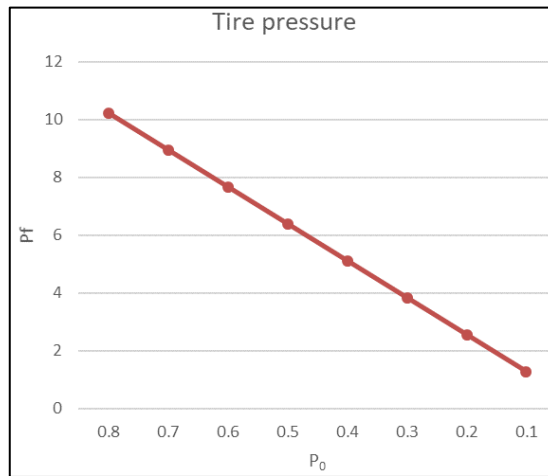
$$T_f = \frac{F_p}{4\pi * r_f} = (a^2 - r_f^2) \frac{P_0}{4 * r_f}$$

However, to perform the simulation, the  $T_f$  load is not useful since the parameter that is needed to evaluate the performance of the rim is the pressure acting in the contact area between rim and tire. For this reason,  $P_f$  which is the value of this pressure has been calculated as follows:

$$P_f = \frac{F_p}{2 * \text{contact area}}$$

In table 3.14, the evolution of the pressure values acting on the rim during the inflation process of the tire are shown. As it is described in figure 3.15,  $P_0$  represents the internal

pressure inside the tire while  $P_f$  represents the pressure which acts in the contact area between the rim and the tire.



Pressure $p_0$	8	7	6	5	4	3	2	1	[bar]
	0.8	0.7	0.6	0.5	0.4	0.3	0.2	0.1	[MPa]
Radius $r_f$	203	203	203	203	203	203	203	203	[mm]
Radius $a$	279	279	279	279	279	279	279	279	[mm]
Axial comp. $F_p$	92066	80558	69050	57541	46033	34525	23017	11508	[N]
Contact area tire-rim	4500	4500	4500	4500	4500	4500	4500	4500	[mm <sup>2</sup> ]
Pressure $p_f$	10.23	8.95	7.67	6.39	5.11	3.84	2.56	1.28	[MPa]

<b>Inflation Press.</b>	8	7	6	5	4	3	2	1	[bar]
<b>Pressure <math>p_0</math></b>	0.8	0.7	0.6	0.5	0.4	0.3	0.2	0.1	[MPa]
<b>Pressure <math>p_f</math></b>	10.2	9.0	7.7	6.4	5.1	3.8	2.6	1.3	[MPa]

Table 3.14: Evolution of the pressure values acting on the rim during the inflation process of the tire.

To perform the rim simulations, the values selected for these pressures correspond to the values for an inflation pressure of 8 bar. Even if the nominal inflation pressure of the wheel (5 bar) does not reach this value, it has been decided to perform it with this magnitude, in order to obtain a certain margin of safety in the simulation results.

## 4.- DESIGN PROCESS

### 4.1.- WHEEL HOUSING

The purpose of this part of the project is to make another wheel housing that was already produced for the old vehicle of Emilia 4 project but including some changes from the previous model.

For this new assembly of the wheel, the transmission is performed by the action of three pins located between the wheel housing and the flange wheel, which is directly glued to the lens, to transmit the rotational movement.

In the previous Emilia 4 vehicle, the transmission was made using noses connecting directly the lens and the rotor part of the motor (figure 4.1). This design concept must be changed because, during the manufacturing process of the previous lens using CFRP materials, it took a lot of time to produce a single piece due to its complex shape.

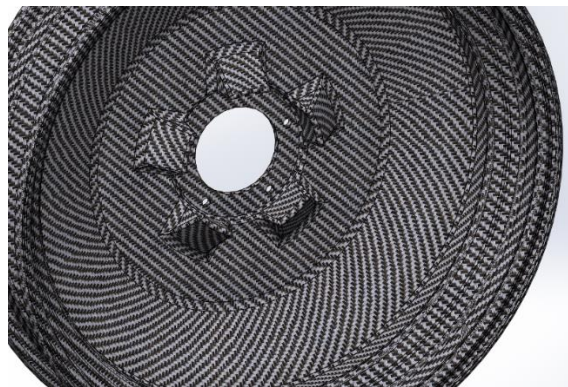


Figure 4.1: Detail of the noses in the previous wheel.

For this reason, it has been decided to change the assembly of the previous wheel and remake again some components to have a better performance.

#### 4.1.1.- Material

The main objective to make this component, is to reduce as much as possible its weight, but maintaining a good behaviour in mechanical performance.

This is the reason why, the material selected to produce this part of the assembly is Alclad Aluminium 7075- T6 [44]. This material allows to have a lightweight piece, but rigid and strong enough to hold on all the loads acting on it.

It is not possible to make this component with composite materials because as it can be seen in figure 4.2, the bearings of the hub are located inside this piece. It means that, during the placement of the bearings, the inner surface of the wheel housing could be damaged. However, using Aluminium is possible to avoid this problem since there would be a metal-metal contact between bearings and the wheel housing piece.

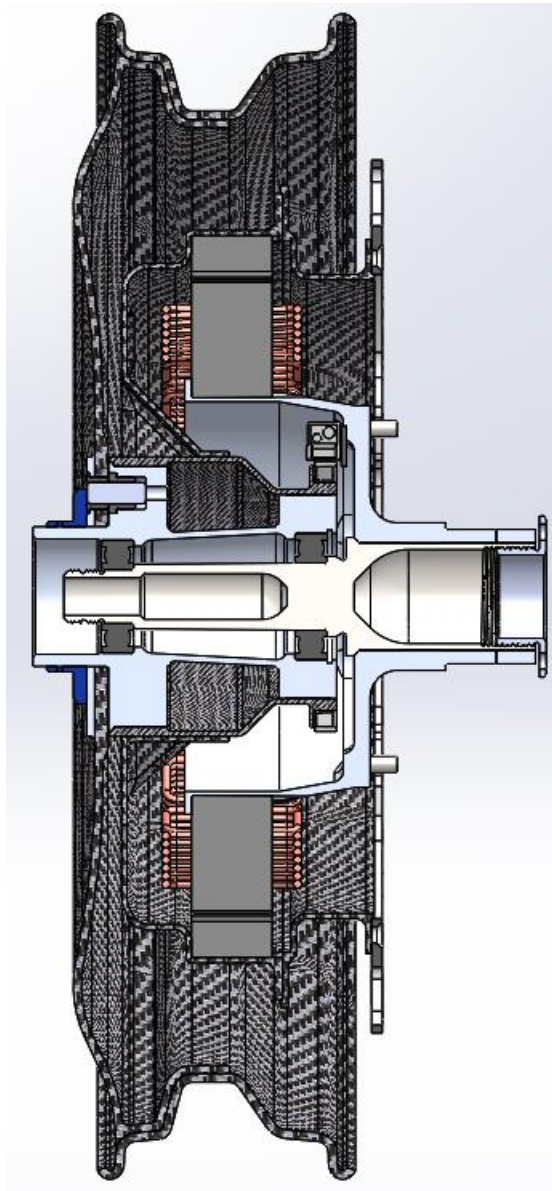


Figure 4.2: Detail of the final wheel assembly.

The only problem that this material has for the transmission, is the contact pressure between pins and the wheel housing. Aluminium has a lower admissible contact pressure than steel, and as it will be shown later, this is one the most crucial part to consider in terms of design and during the simulations.

#### 4.1.2.- Topology optimization

The first step to produce the wheel housing piece, is to optimize its shape and, as it is said before, to reduce the mass of the component as much as possible keeping a good mechanical performance. To perform it, a topology optimization has been done (figure 4.3). This tool, as it will be described later, allows to see how the shape of this piece could be in the future keeping some key constrains.

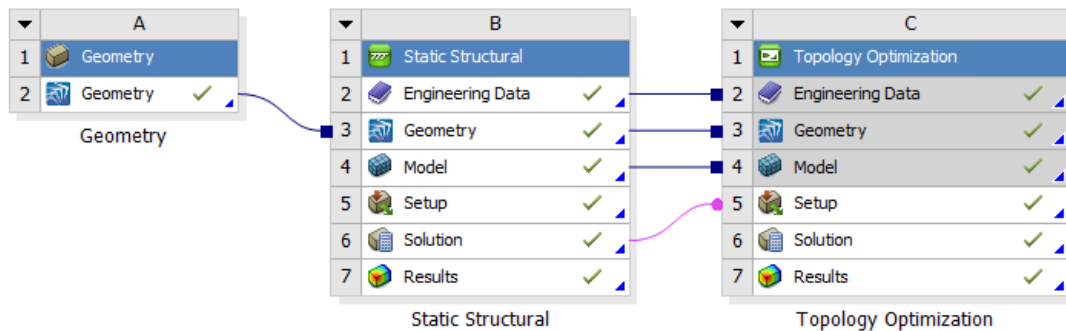


Figure 4.3: Project schematic to perform the topology optimization.

To do this, it has been done a simple piece just maintaining the most representative dimensions which are needed in the final design. For example, the two outermost surfaces of this piece are an example of that, because they have to be glued to the motor hub (mozzo rotore carbon). In this way, the rotor part of the motor can transmit the rotation through this piece (motor hub) to get that movement also in the wheel housing. For this reason, the diameter of that surfaces must be the same after the simulation.

The component made to perform the topology optimization is shown in figure 4.4:

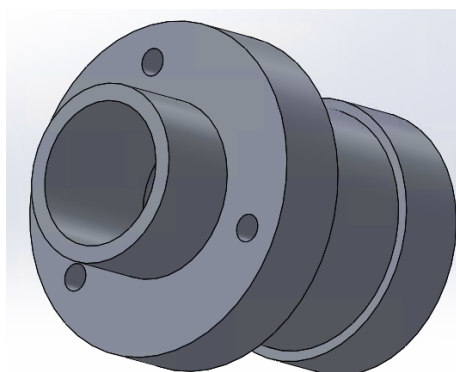


Figure 4.4: First design of the wheel housing component.

#### 4.1.2.1.- Materials

The first step to perform a simulation is to set all the materials of the assembly and the loads and constraints that are acting on it. For this model, only a few components of the final assembly have been included (figure 4.5):

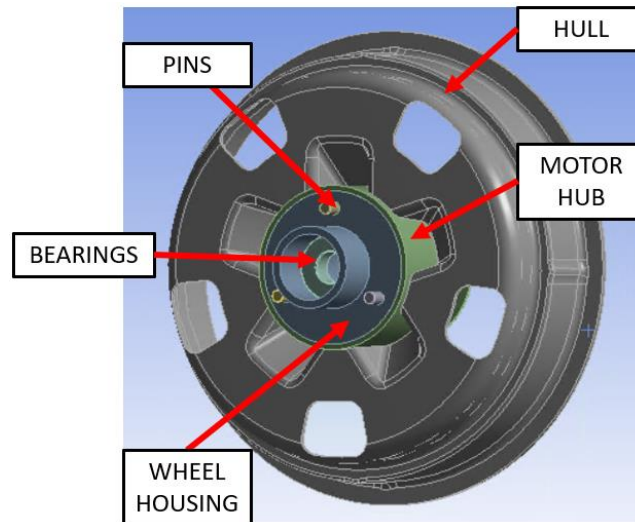


Figure 4.5: Assembly used for the topology optimization.

As it can be seen in figure 4.6, to represent bearings and pins, structural steel has been used, the motor hub and the hull are made of T800 Twill which is a composite material (this material has been defined as an homogeneous isotropic material), and the wheel housing is made of Alclad Aluminium 7075-T6.

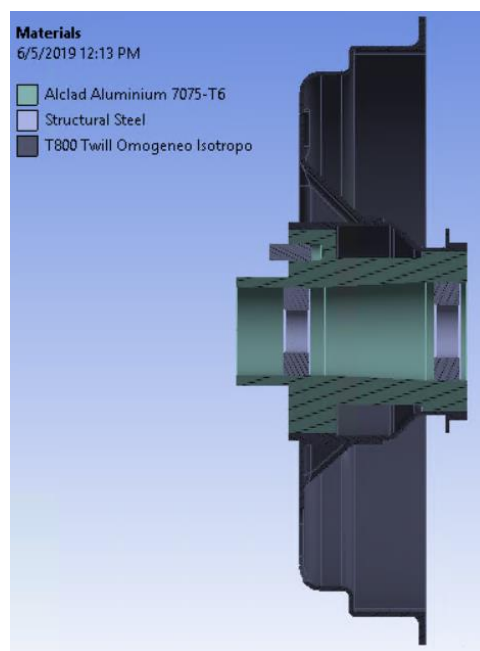


Figure 4.6: Simulation materials.

#### 4.1.2.2.- Loads & constraints

After introducing the materials, loads and constraints of this model have been determined.

The loads applied on the model are the following:

- Bending moment which represents the effect of the car taking a curve. This moment acts on the two external surfaces of the wheel housing and its estimated value is 730 Nm (+Z direction).
- Torsion moment acting on the three pins due to the transmission movement. The value of this torque is 740 Nm which has been represented as three forces acting on the pins with its corresponding module and direction.

In figure 4.7, all the loads acting on the model are shown:

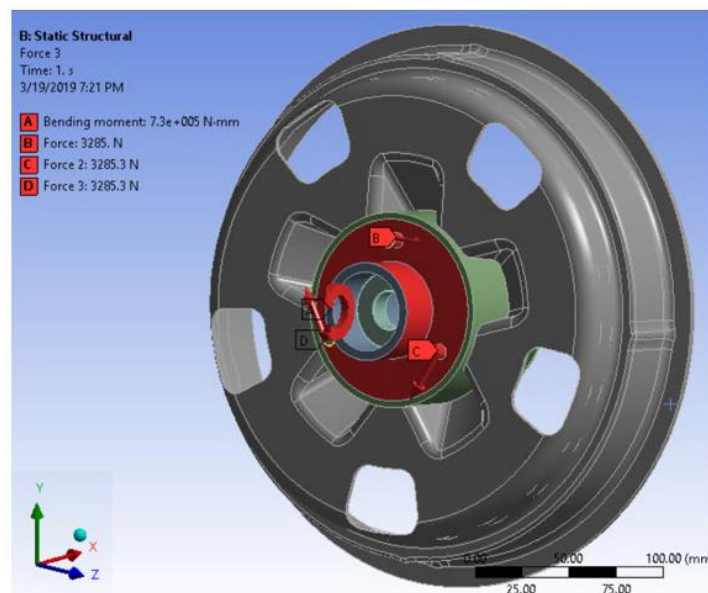


Figure 4.7: Simulation loads.

The constraints considered for this simulation (figure 4.8) are the following:

- Cylindrical support on the inner surface of the smaller bearing fixing the radial and axial movement but keeping free the tangential displacement.
- Cylindrical support on the inner surface of the bigger bearing fixing only the radial movement and keeping free on the axial and tangential directions.
- Cylindrical support on the outer surface of the hull to model the performance of the assembly during a braking. To do this, the tangential movement has been fixed.

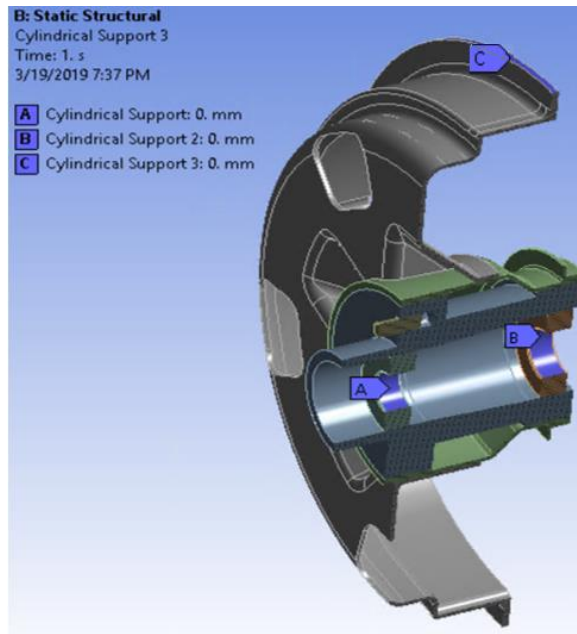


Figure 4.8: Simulation constraints.

#### 4.1.2.3.- Results

The maximum deformation of the assembly is located on a pin and its value is almost 0.06 mm , besides, the maximum value of deformation on the wheel housing is approximately 0.04 mm (figure 4.9):

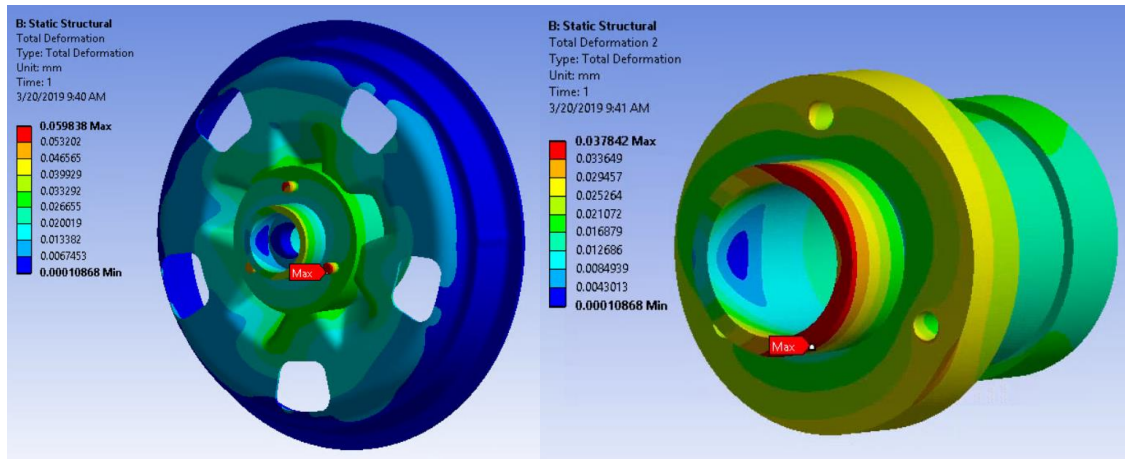


Figure 4.9: Deformation results in the assembly and on the wheel housing.

The maximum stress value is located on the external face this piece, where one of the pins is located. The exact value of this stress is 241,71 MPa as it is shown in figure 4.10:

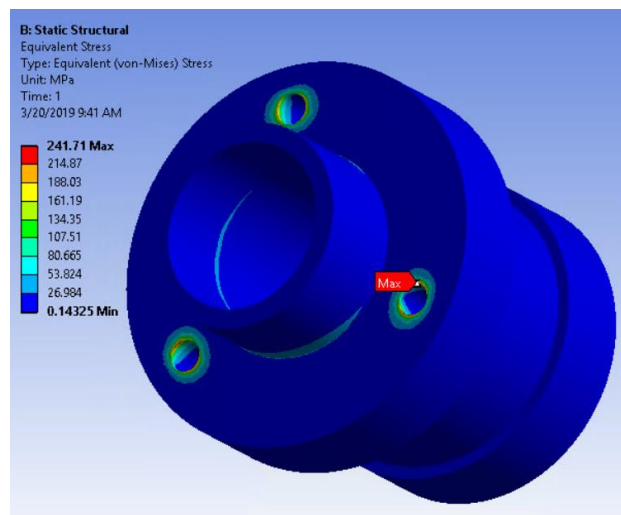


Figure 4.10: Maximum stress acting on the wheel housing.

As it is said before, another important parameter to consider is the contact pressure between pins and the wheel housing. In this case, most part of the contact surface is recognized as sticking. The contact pressure distribution between pins and the wheel housing has a maximum value of 359.8 MPa (figure 4.11).

As it will be seen in the following paragraphs, a solution to reduce this contact pressure will be described.

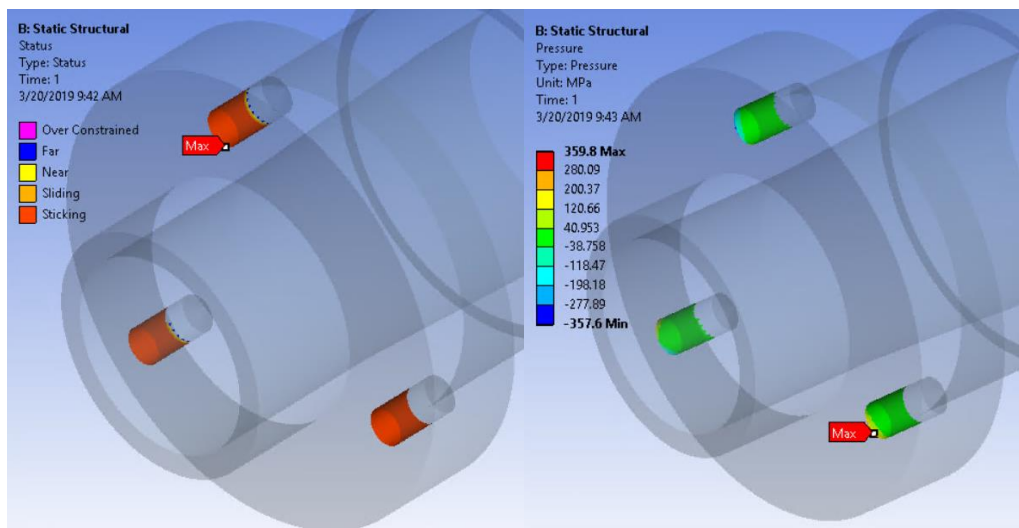


Figure 4.11: Contact status and contact pressure distribution between pins and the wheel housing.

#### 4.1.2.4.- Topology optimization

Topology optimization can produce working concepts that are optimized to a set of design criteria. It finds the best distribution of material given an optimization goal and a set of

constraints. Specifically, it works by taking a solid block of material in any shape and removes material to minimize or maximize an optimization objective such as mass, displacement, or compliance while satisfying a set of constraints such as maximum stress or displacement.

In this particular case, these are the constraints included to perform the simulation:

- Optimization region: in this section, it must be selected those surfaces that could be modified to get the final shape of the piece and those that must remain the same. For example, for the wheel housing the red surfaces that are represented in figure 4.12 has to be fixed because, through these surfaces, this piece will be assembled to other parts of the assembly that are already produced. On the other hand, the blue surfaces represent the dimensions that can be changed to get an optimized shape of the final part.

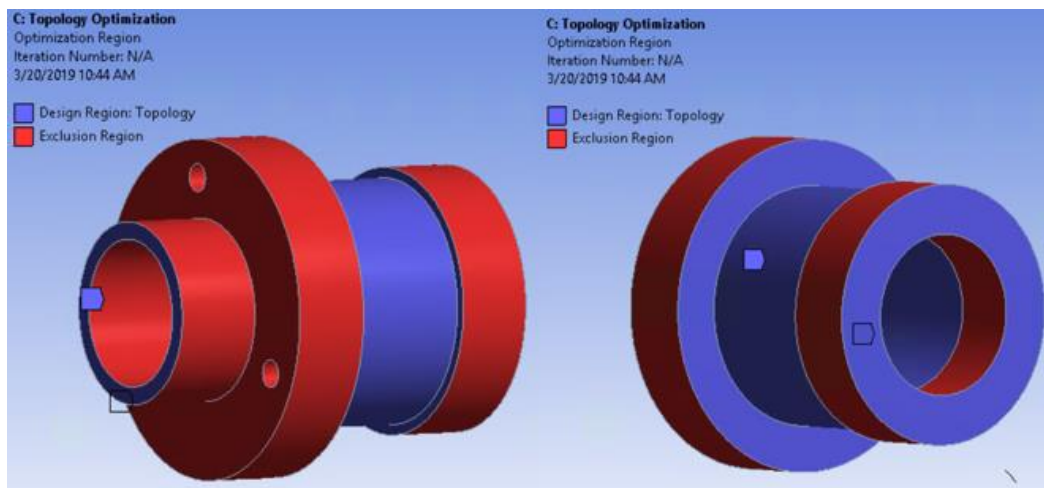


Figure 4.12: Types of regions used to perform the topology optimization.

- Objective: Minimize the compliance.
- Response constraints: For this simulation, to get the optimized region, the percent of mass to retain from the original model has been fixed as the 60%. In addition, to avoid problems with stresses, the maximum stress that this piece can reach has been fixed as 400 MPa.
- Manufacturing constraints: In this case, the piece that is analysed has a symmetrical pattern referred to the revolution axis (+X axis of the model). As it can be seen in the figures, the frontal plane of this piece has a symmetry and it can be divided in

three different sectors taking as reference the holes for the pins. This allows the program to identify better the shape of the original piece.

Moreover, the minimum size in terms of dimensions is 3 mm. With this constraint, it is ensured that the component will maintain at least a minimum thickness of 3 mm.

Finally, after performing the simulation, the program shows a solution that represents the shape of the piece considering all the constraints (figure 4.13). For these types of simulations, these results only serve as a guide to intuit the final shape of a component.

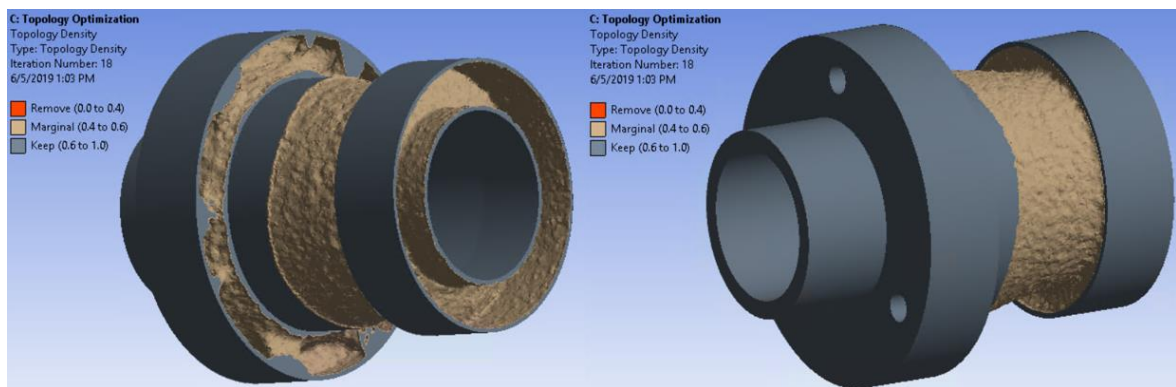


Figure 4.13: Results of the topology optimization.

As it can be seen in the previous figure, there is a lot of material that can be removed from this piece, so, the next step is to design again this component but keeping in mind that there are surfaces that could be changed.

#### 4.1.3.- FEM simulation (second design)

After some considerations, a second design (figure 4.14) has been done regarding the results of the topology optimization.

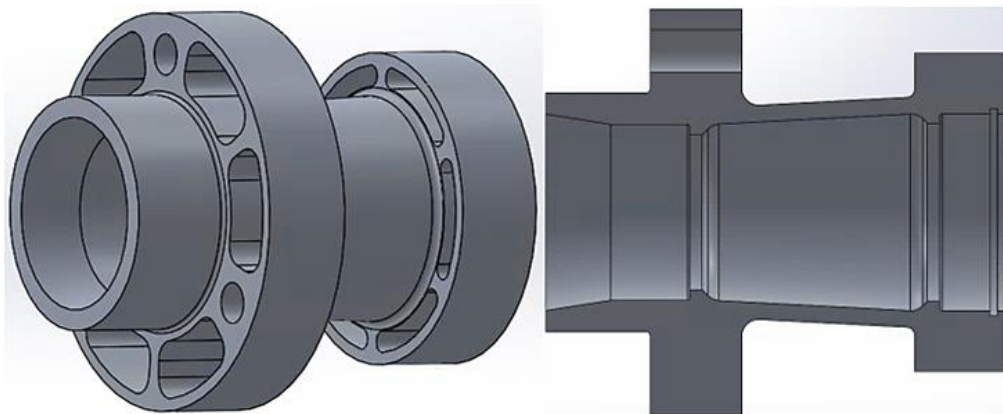


Figure 4.14: Second design of the wheel housing.

In order to optimize the final form of the component as much as possible, simulations have been carried out to predict its final performance. Thus, these simulations allow to understand better which are the most requested areas, or otherwise, where it is possible to remove more material.

This second design has the following differences from the previous one:

- The diameter and length of the pins have been changed. In this model, the diameter of the pins has been increased 2 mm (from 8 mm to 10 mm). Moreover, the holes to locate the pins are through holes and the pins cover more surface of the component. In this way, the contact pressure between pins and the wheel housing is reduced.
- The inner surface has been modified to locate the hub bearings inside this piece. These features, the bearings selection and configuration will be explained in the design of the final component.
- On some surfaces, there are through holes to reduce the weight of the component following the results of the topology optimization.

For this FEM analysis, all the materials, loads and constraints are the same as those used in the previous simulation. The aim of this simulation is to see how the second design of this component works.

#### 4.1.3.1.- Results

The maximum deformation in the assembly is almost 0.09 mm and it is located on one of the three pins (figure 4.15). In addition, the maximum deformation in the wheel housing is approximately 0.05 mm.

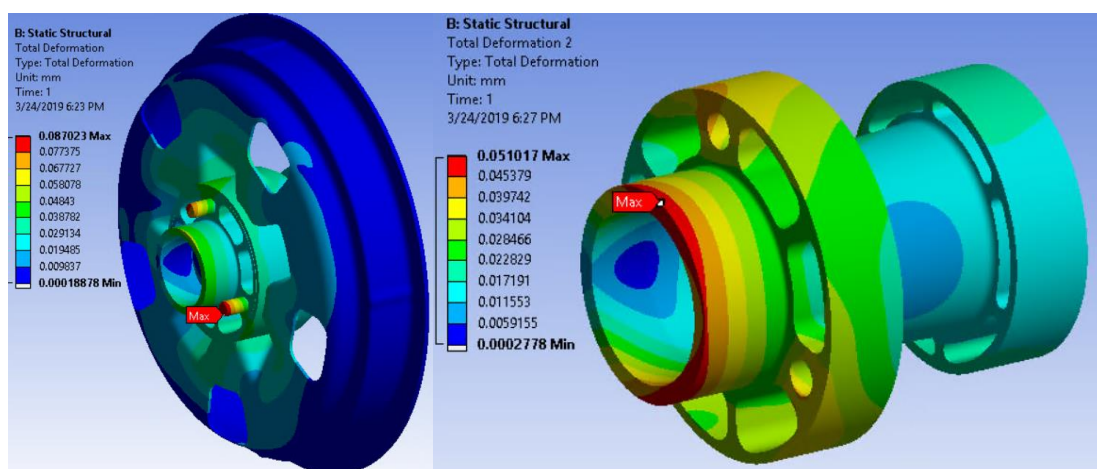


Figure 4.15: Deformation results in the assembly and on the wheel housing.

On the other hand, in figure 4.16 are represented the equivalent stress and safety factor of the component:

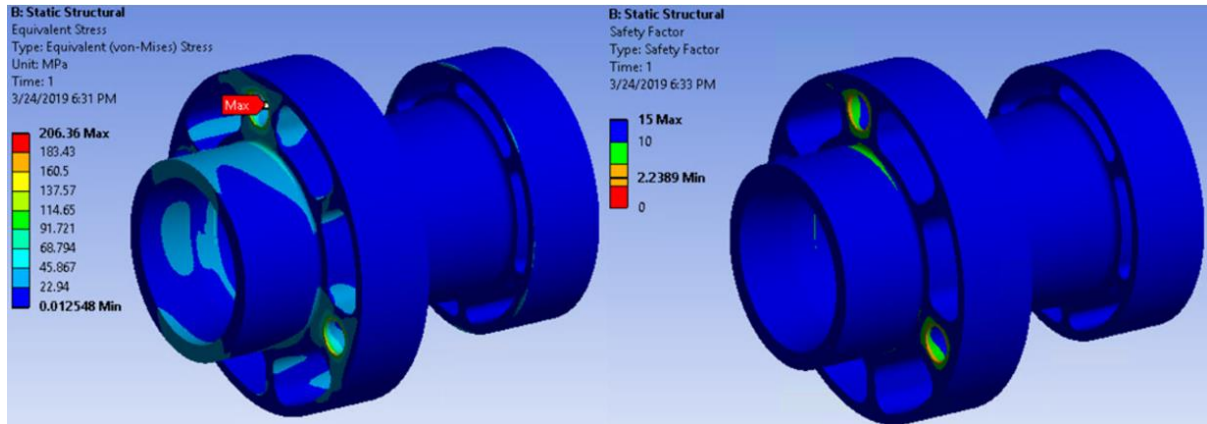


Figure 4.16: Equivalent stress and safety factor results.

The maximum stress is located on the edge of one of the holes where the pins are located, reaching a value of 206.4 MPa approximately. This means that the safety factor in the most critical part of the component is 2.23, thereby, it is possible to increment the size of the holes to remove more material.

The contact pressure has been decreased from the previous simulation (figure 4.17). This is because, as it is mentioned before, the diameter and length of the pins have been changed.

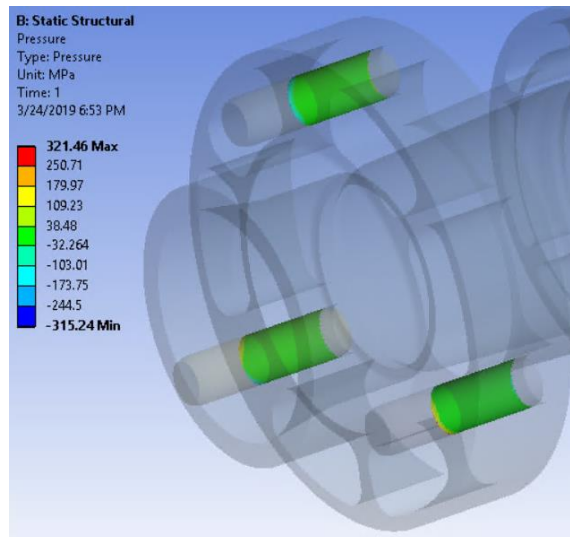


Figure 4.17: Contact pressure distribution.

#### 4.1.4.- FEM simulation (third design)

In this design, there is only a difference from the second version, the through holes to reduce the weight of this component have been increased. Moreover, this is the first simulation that includes all the components of the wheel assembly.

##### 4.1.4.1.- Materials

To perform this simulation, three different materials have been used to simulate the performance of the system:

- T800 Twill (composite material): this material is used for the motor hub and the hull (figure 4.18).
- Structural steel: to represent bearings, bushes, pins, ferrule of the hub (ghiera mozzo) and the ferrule to fix the smaller bearing. (figure 4.18).

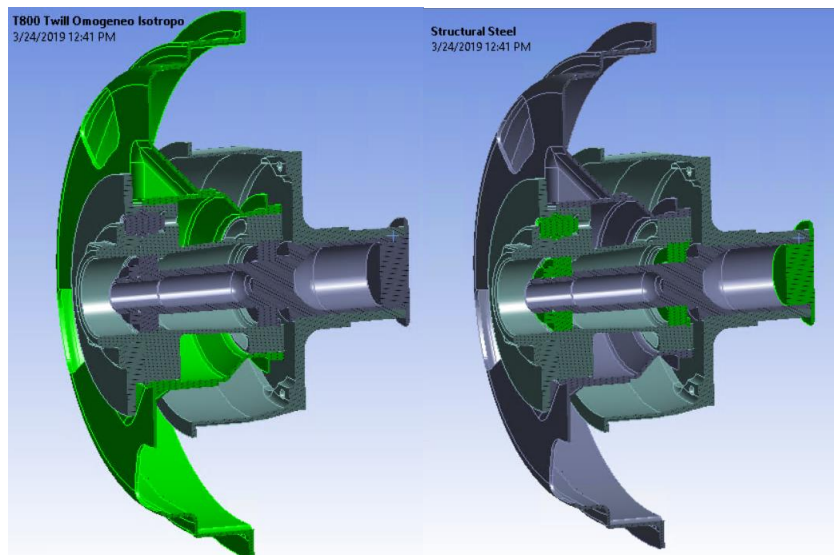


Figure 4.18: T800 Twill and structural steel components.

- Alclad Aluminium 7075-T6: wheel housing, flange, the ferrule of the wheel and the stator component (figure 4.19).
- 52SiCrNi5 (45 HRC) [45]: hub of the wheel (figure 4.19).

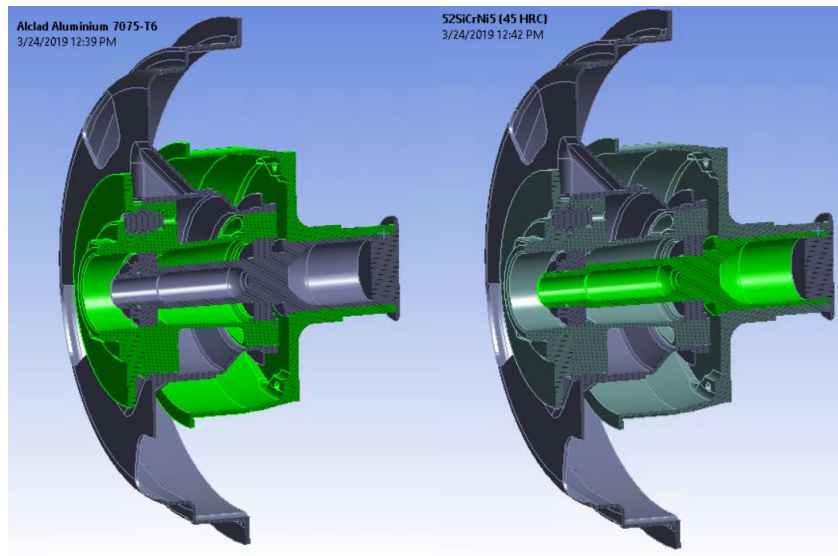


Figure 4.19: Alclad Aluminium 7075-T6 and 52SiCrNi 5 (45 HRC) components.

#### 4.1.4.2.- Loads & constraints

For this simulation, the loads are the same as in the previous simulation, but in this case, these moments are applied only on the outer face of the flange (figure 4.20):

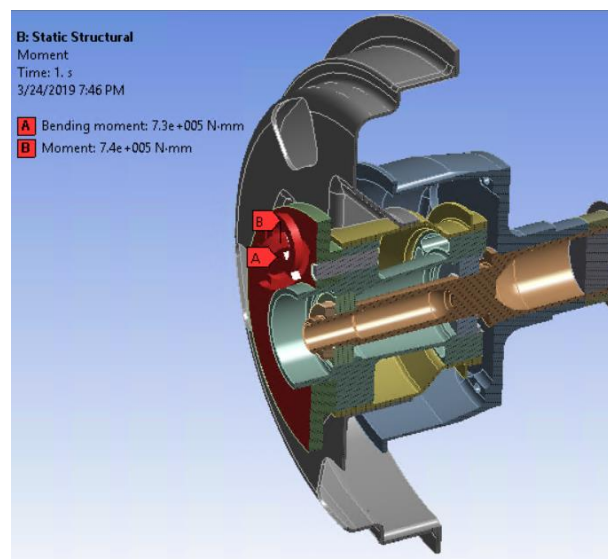


Figure 4.20: Forces acting on the assembly.

In addition, constraints have been changed to simulate the performance of the wheel:

- Cylindrical supports applied on the external surfaces of stator component as it is represented in figure 4.21. In these supports, the radial and axial displacements are fixed, although, in the tangential direction is totally free to move.

- Remote displacement to represent the action of the breaks on the wheel. The location of this displacement is (50,0,0) considering the global coordinate system of the assembly and it is applied on the surface shown in figure 4.21.

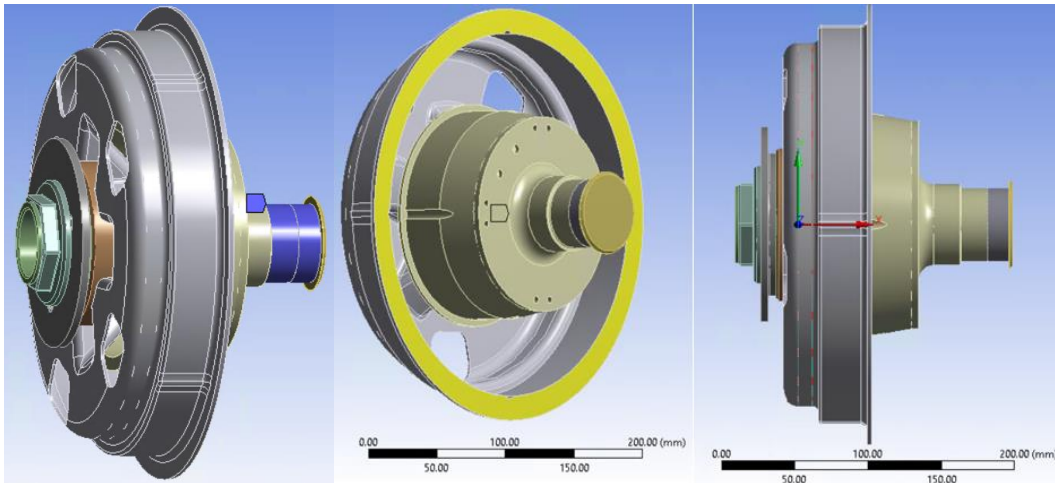


Figure 4.21: Cylindrical support and remote displacement constraints.

#### 4.1.4.3.- Results

The maximum deformation in the assembly is almost 0.9 mm and it is located on the external face of the hull. The maximum deformation of the wheel housing is approximately 0.67 mm (figure 4.22).

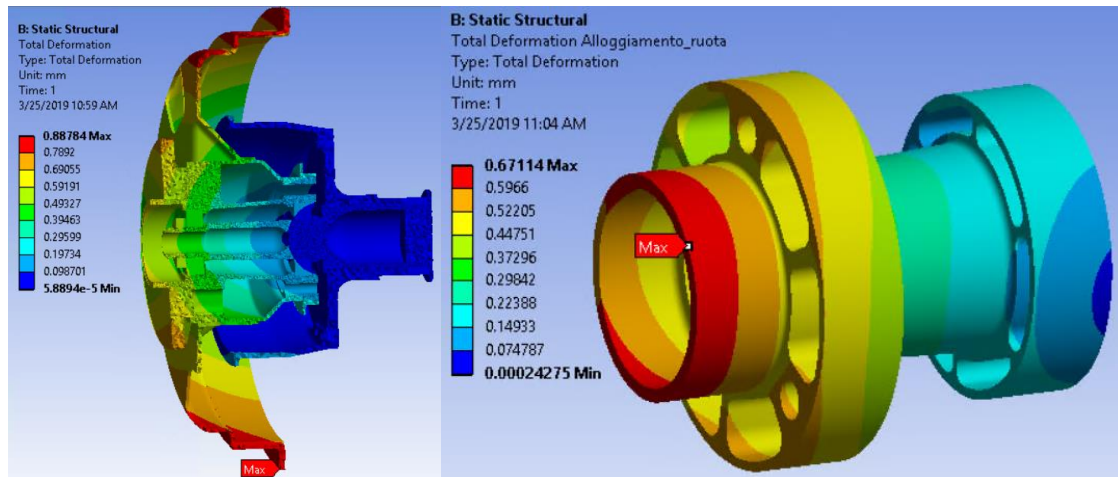


Figure 4.22: Total deformation results in the assembly and on the wheel housing.

On the other hand, the stress distribution and the safety factor of the wheel housing have been calculated (figure 4.23)

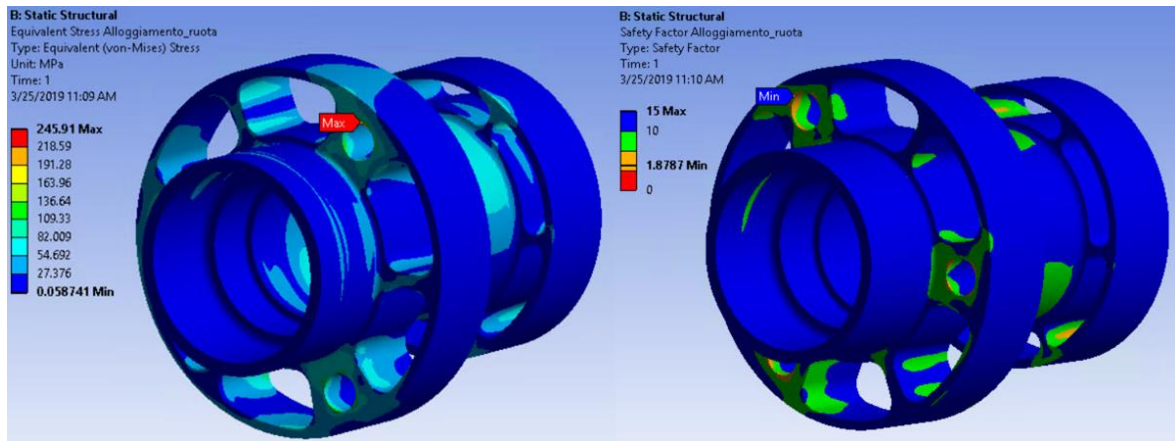


Figure 4.23: Stress distribution and safety factor of the component.

As it can be seen in the previous figure, the maximum stress value of the component is 245.9 MPa with a safety factor of 1.87. Moreover, the maximum value of the contact pressure is 138.48 MPa which has been decreased significantly from the previous simulation (figure 4.24).

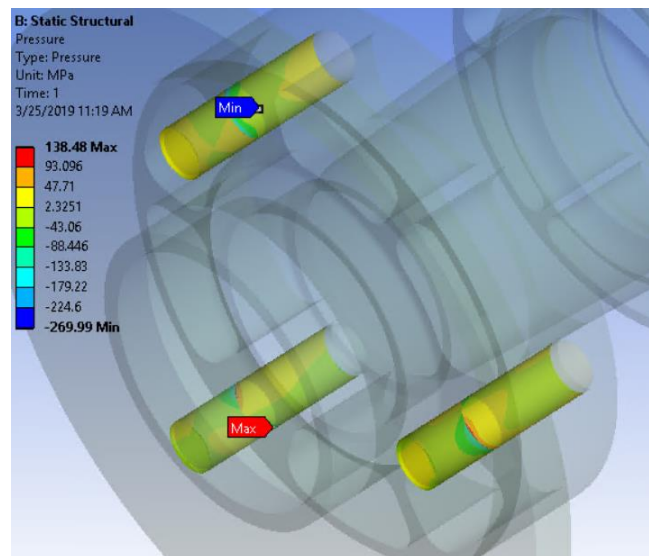


Figure 4.24: Contact pressure distribution between pins and holes.

In summary, as it can be observed in the results, this component satisfies all the requirements set before. For this reason, this is the component that has been presented to the producer as a preliminary final design. However, after a meeting with the producer, it has been decided to make some changes to obtain the final component. These changes are explained below in the design of the final component.

### 4.1.5.- Design of the final component

After the meeting with the producer and some simulations, a final solution for this component has been realized. In the following paragraphs, the process to get this final shape will be described.

#### 4.1.5.1.- Inner surface

As it was described before, inside this component, there are two bearings which allows to connect this part with the hub of the wheel and transmit the rotational movement.

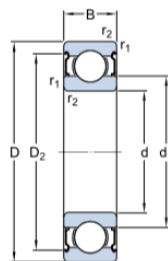
In the previous version of the car wheels, the bearings chosen had diameters of 30 mm and 35 mm respectively. During the tests with the accelerometer, it had been obtained high safety factor values, therefore, for this new design of the wheel, it has been decided to reduce its diameter. In addition, choosing smaller bearings reduces the weight of the wheel assembly and saves energy due to the friction action.

The bearings used for this wheel are shown in figure 4.25 and figure 4.26:

► **6004-2Z**

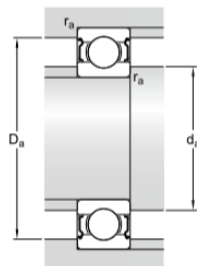
Popular item  
SKF Explorer

**Dimensioni**



d	20	mm
D	42	mm
B	12	mm
d <sub>1</sub>	≈ 27.2	mm
D <sub>2</sub>	≈ 37.19	mm
r <sub>1,2</sub>	min. 0.6	mm

**Dimensioni dello spallamento**



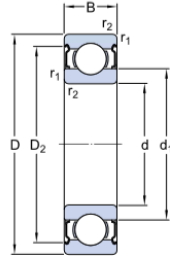
d <sub>a</sub>	min. 23.2	mm
d <sub>a</sub>	max. 27.1	mm
D <sub>a</sub>	max. 38.8	mm
r <sub>a</sub>	max. 0.6	mm

Figure 4.25: Dimensions of the bearing for the smaller diameter [46].

► 6005-2Z

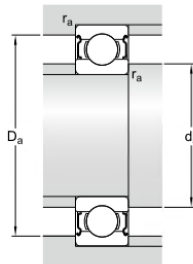
Popular item  
SKF Explorer

Dimensioni



d	25	mm
D	47	mm
B	12	mm
d <sub>1</sub>	≈ 32	mm
D <sub>2</sub>	≈ 42.2	mm
r <sub>1,2</sub>	min. 0.6	mm

Dimensioni dello spallamento



d <sub>a</sub>	min. 28.2	mm
d <sub>a</sub>	max. 31.9	mm
D <sub>a</sub>	max. 43.8	mm
r <sub>a</sub>	max. 0.6	mm

Figure 4.26: Dimensions of the bearing for the bigger diameter [47].

Considering these dimensions, it has been designed the correct location with the proper measures to achieve the expected performance of the bearings.

On the other hand, a seeger ring (figure 4.27) has been included to fix the displacement of the bigger bearing.

**Anillos elásticos para agujeros o interiores**

DIN 472  
(Ceta 30806)

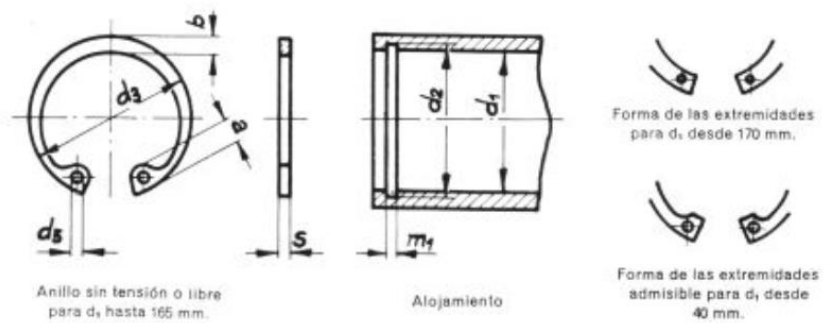


Figure 4.27: Main dimensions of the seeger DIN 472 for inner holes [48].

The dimensions for this specific seeger can be seen in table 4.1:

Dimensions of the seeger		
d_5 (min)	2.5	mm
d_3	50.5	mm
b	4.4	mm
a (max)	6.4	mm
s	1.75	mm
Dimensions of the hole		
m_1	1.85	mm
d_2	49.5	mm
d_1	47	mm

Table 4.1: Dimensions of the seeger used for this application [48].

With this bearing configuration, depending on the direction of the axial force acting on the hub, all that load will be absorbed by a single bearing.

In figure 4.28, the final shape of the inner part of the component is shown:

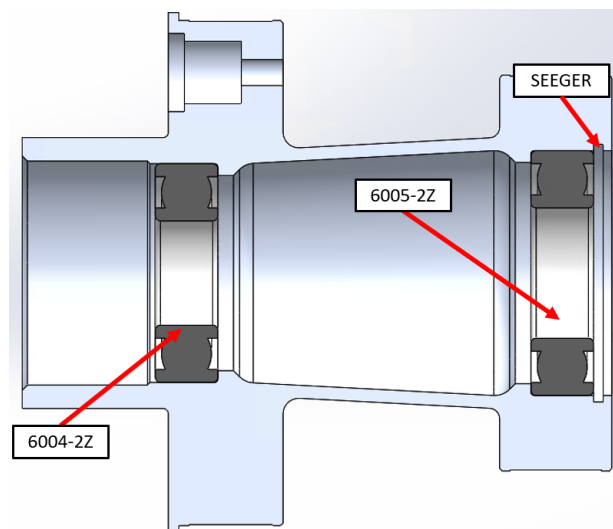


Figure 4.28: Cross-section view of the component.

#### 4.1.5.2.- External surface

On the outer part of this piece there are different surfaces that are in contact with other components of the assembly:

- The frontal plane where the holes of the pin are located is in contact directly with the wheel flange.

- On the two outer surfaces of the component, as it is said before, are glued directly to the motor hub. For this reason, as it can be seen in figure 4.29, there are gaps between that two components, these gaps allow to put the adhesive between that two surfaces. Moreover, there is a small step on the first surface which serves to centre better these two bodies.

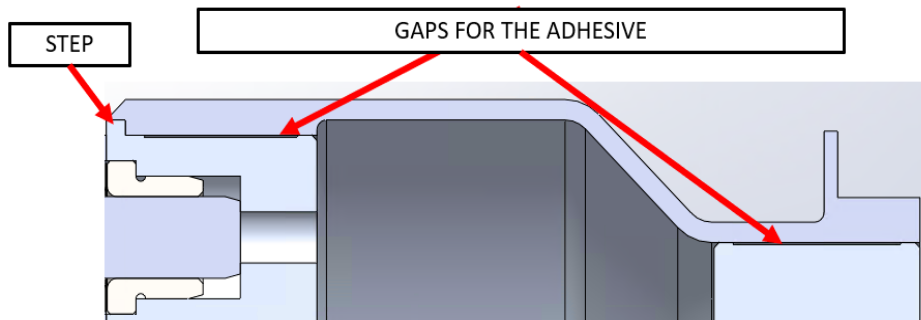


Figure 4.29: Detail of the external surface of the wheel housing.

- On the left side of the component that corresponds to the outer part of the wheel, to fix the flange wheel with the wheel housing, a ferrule is used (figure 4.30). This ferrule is threaded to the surface of the wheel housing to avoid gaps in the contact region between this component and the flange.

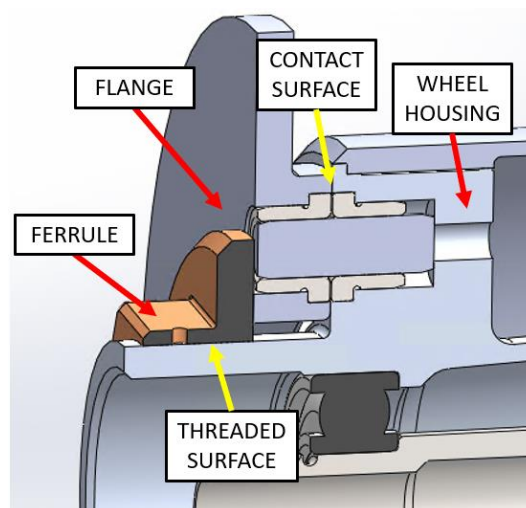


Figure 4.30: Detail of the assembly surfaces.

For this final design, the holes created in the second design have been enlarged to remove more material that is not useful for the resistance of the component (figure 4.31). Moreover, the thickness of the conical part between the location of the bearings have been

reduced to 2.5 mm. This thickness has this value because is the minimum thickness that the producer of this component can reach with his machining tools.

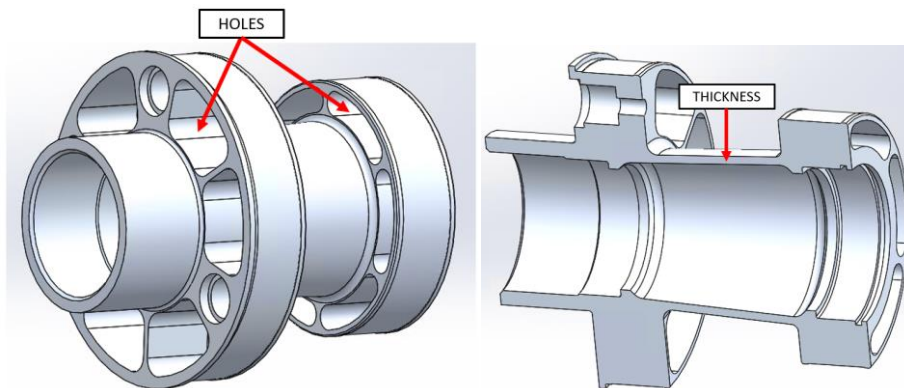


Figure 4.31: Holes and thickness performed to reduce the weight of the component.

#### 4.1.5.3.- Pins and its location

As it is said before, one of the targets to achieve the final component is to reduce the contact pressure between pins and the aluminium parts of the assembly (wheel housing and flange). To realize this, six bushes have been included in the assembly, three on each component, and in between these bushes, the pins are located. The bushes are made by steel, which has a bigger admissible pressure than aluminium.

Furthermore, bushes allow the operator who will assembly all these components together, to fix better the position of the holes for the pins and to avoid possible misalignments. In addition, threaded holes have been made on the back face of the wheel housing to fix the position of the pins inside the main holes. These threaded holes are used to put a screw and then tighten that screw against the pin (figure 4.32).

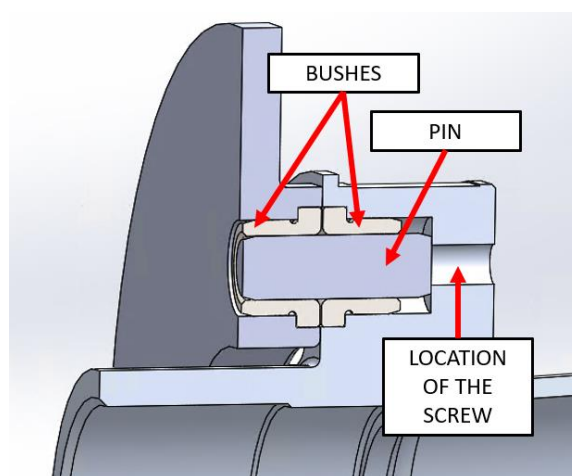


Figure 4.32: Detailed view of the bushes and pins locations.

These bushes are commercial components which geometric characteristics are shown in figure 4.33:



Figure 4.33: Datasheet of the bushes. [49]

#### 4.1.6.- FEM final simulation

As it has been done in the third simulation, the final simulation includes all the components of the complete wheel assembly.

##### 4.1.6.1.- Materials

In this case, the materials and components are the same as in the third simulation.

##### 4.1.6.2.- Loads & constraints

After introducing the materials, loads and constraints of this simulation have been determined.

For this model, all the contacts between the components have been considered as bonded except in two cases:

- Frictionless contact between the wheel housing and the ferrule: the surface in contact between these two bodies has been considered as frictionless because there is no adhesive or other element that joints them, they are simply in contact with each other.
- Frictional contact between the ferrule and the wheel housing: as it is said before, these two components have a screwed union between them. To model this performance, it has been considered a coefficient of friction of 0.2 between the two screwed surfaces. In addition, a bolt thread contact has been performed (figure 4.34).

Geometric Modification	
Interface Treatment	Adjust to Touch
Contact Geometry Correction	Bolt Thread
Orientation	Program Controlled
<input type="checkbox"/> Mean Pitch Diameter	50.05 mm
<input type="checkbox"/> Pitch Distance	3. mm
<input type="checkbox"/> Thread Angle	60. °
Thread Type	Single-Thread
Handedness	Right-Handed

Figure 4.34: Geometrical parameters of the bolt thread contact.

In this case, a M52x3 profile is used to join these two components. This means that the mean pitch diameter (as it is shown in Annex I) has a value of 50.05 mm.

The pitch distance is 3, the thread angle is 60° (metric profile) and the thread type is a right-handed single-thread screw.

The loads applied on the model are the same as in the previous simulations:

- Bending moment acting on the flange surface where the lens of the wheel is glued.
- Torsion moment acting on the same face where the bending moment is applied.
- Bolt pretension to simulate the performance of the threaded joint between the wheel housing and the ferrule. The considered preload of this bolt pretension has been 40000 N (calculations shown in Annex I).

In the case of the bending and torsion moment, they have the same value as in the previous simulations.

On the other hand, the constraints of cylindrical support and remote displacement, are the same as in the third simulation.

#### 4.1.6.3.- Results

In this case, to evaluate the results in terms of deformation is better to show the equivalent elastic strain of the component. This is because the rest of the components have an impact on the total deformation results of the wheel housing.

The equivalent strain results of this part are shown in figure 4.35:

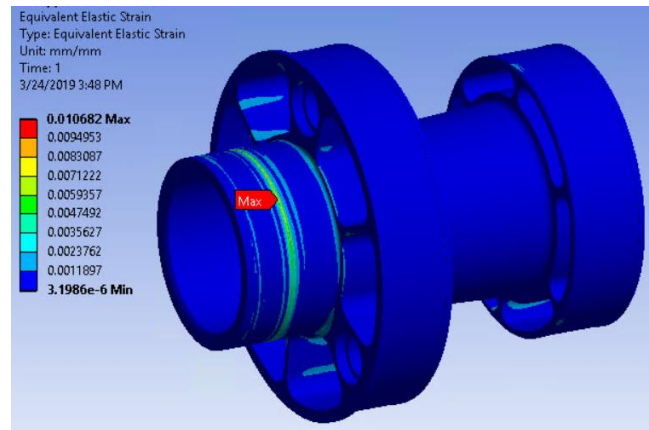


Figure 4.35: Equivalent strain results on the wheel housing.

The maximum equivalent stress on the wheel housing is 756.75 MPa. The material used for this component is Alclad Aluminium 7075-T6 which has an elastic limit of 462 MPa. This means that safety factor in the most requested area of the component is less than one (figure 4.36)

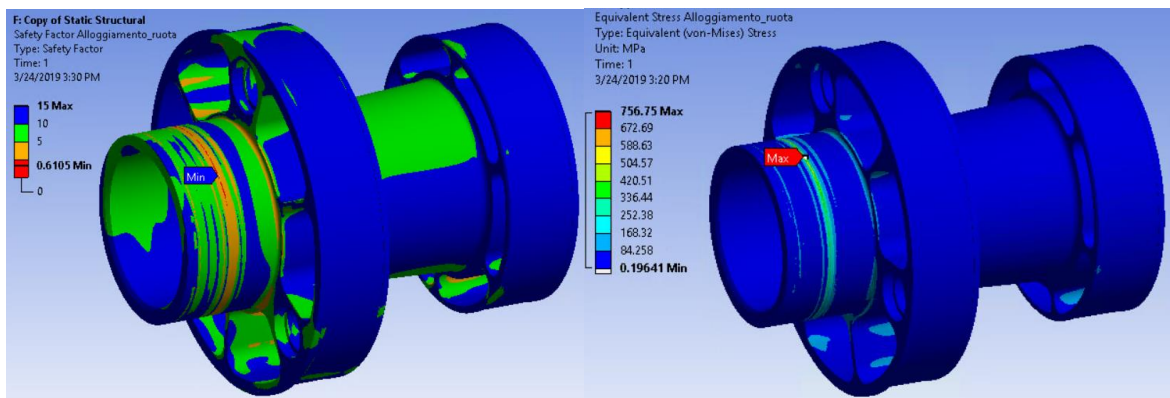


Figure 4.36: Safety factor and equivalent stress results of the wheel housing.

Despite this, it has to be considered that during the tightening of a component which is threaded it is normal to reach the elastic limit of the material and to have a plastic deformation in some areas of the screw. This is the explanation why in this component there are areas of the threaded surface, where there is a safety factor less than one. On the rest of the component parts, the safety factor is always more than one, so, it can be concluded that in terms of stresses, the component is completely validated.

Finally, as it is mentioned before, one of the most critical aspects to study is the contact pressure between the pins and bushes to transmit the rotational movement.

As it has been performed in previous simulations, a complete analysis of the contact pressure has been realized (figure 4.37).

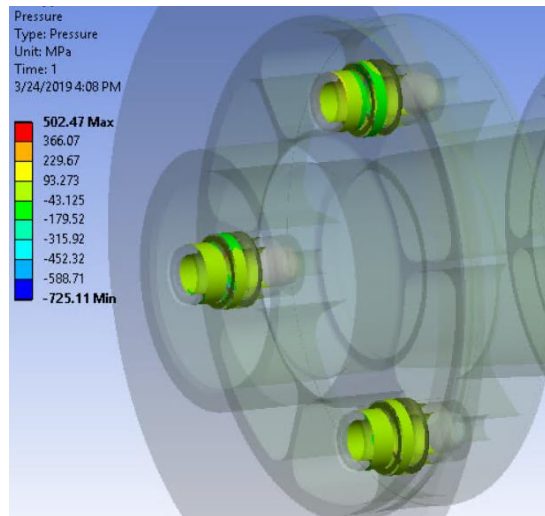


Figure 4.37: Pressure distribution on the pins and bushes locations.

The maximum value of this pressure is 725.11 MPa located on the inner surface of one of the bushes. Considering that the bushes are made of UNI 18NiCrMo5 steel, which has an admissible contact pressure of 1400 MPa [50], the components work below their allowable pressure values.

In summary, all the safety requirements are satisfied for this component. This means that the materials selected and the considerations taking during the design process are validated for this application. In table 4.2, a summary of the different versions has been done with the main results of the simulations. Finally, some pictures of the final component produced have been included (figure 4.38).



Figure 4.38: Final wheel housing produced.

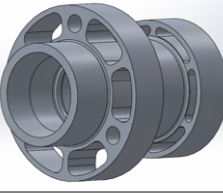
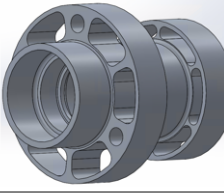
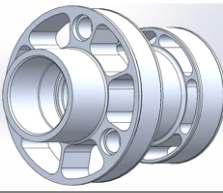
	VERSIONS			
	v 1.0	v 2.0	v 2.1	v 2.2 (Final version)
				
Mass (g)	851.3	484.1	392.5	359.6
Mass variation (%)	REFERENCE	-43%	-54%	-58%
Max deformation (mm)	0.04	0.05	0.67	-
Max stress (MPa)	241.71	206.40	245.90	756.75* (*this value is due to the bolt pretension)
Max contact pressure (MPa)	359.8	321.46	269.99	725.11

Table 4.2: Summary of the different simulation results.

## 4.2.- WHEEL LENS

In this section is explained how the design of some components related with the external part of the wheel, as the lens and rim, have been performed. The objective in this case is to find the optimal shape of the wheel lens, to perform the simulations to validate the lens and rim plybooks, and after that, to make the molds to produce all these parts.

To produce the rim and the lens, only one curing process has been done to join these two components made of composite materials. This is because in the previous Emilia 4 car, the producer of these components decided to cure the lens and the rim separately, having many problems when both elements had been joined.

### 4.2.1.- Lens design

In the main assembly of this wheel, there is only space for one lens to join the central part of the assembly (hub, wheel housing etc) with the rim. Therefore, with only one lens, the wheel must be rigid enough to support the loads acting on it.

A well-designed wheel always incorporates stiffness and compliance, or more specifically, wheels that are laterally stiff and vertically compliant. In engineering terms, this means that the wheel has minimal deflection side-to-side and at the same time moderate to large deflection in the up and down direction [51]. Therefore, the aim of the lens design is to

produce a wheel vertically compliant but trying to increase the lateral stiffness due to the bending moment acting on it.

Following these guidelines, it has been decided to make different lens shapes, and then, using the FEM analysis, determine which lens has a better performance. For the comparison of the different lens models, two different simulations have been carried out. The first one, is related to radial stiffness, and the second is related to lateral stiffness.

In the next paragraphs is described how these lenses are built, and the results comparison between different versions.

#### 4.2.1.1.- Straight lens

For the first case, the lens shape follows a nearly straight path from the flange to the rim. This lens serves as a first design on which the comparisons of the rest of the wheels have been made.

The shape of this straight lens is represented in figure 4.39:

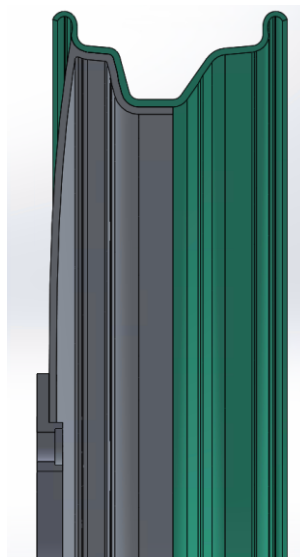


Figure 4.39: Wheel assembly and cross-section detail of the straight lens.

As it can be seen in the cross-section figure of the assembly, the lens directly connects the flange with the rim. The contact region between the lens and the rim will be described in later sections, where the design process of the molds to make both components is explained.

To compare the different versions in the simulations, these lenses have the same contact area with respect to the other components, and also the same thickness which is 3 mm.

#### 4.2.1.2.- Curved lens

In this design, the shape of the lens has been done using a spline curve as it is can be seen in figure 4.40:

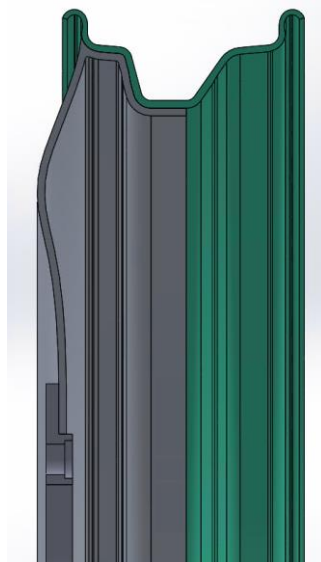


Figure 4.40: Cross-section of the curved lens assembly.

#### 4.2.1.3.- Straight+angle lens

In this case, the shape of the wheel has been done using a straight trajectory, and after that, another straight part including an inclination angle to reach the contact with the rim (figure 4.41).

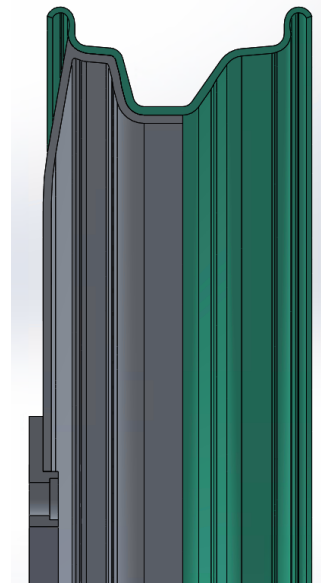


Figure 4.41: Cross-section of the straight+angle lens.

#### 4.2.1.4.- Radial stiffness simulation comparing different designs

To evaluate which is the optimal shape of these lenses, a FEM simulation has been performed to compare them in terms of deformation and stresses. This simulation is useful to understand the performance of the lenses in radial stiffness.

##### 4.2.1.4.1 Materials

To realize the simulation, the flange is done with Alclad Aluminium 7075- T6 and the lens and the rim with T800 Twill. It must be considered that this simulation is only an approximation of the real performance of the composite components because this is done considering these pieces as isotropic homogeneous bodies.

##### 4.2.1.4.2 Loads & constraints

In this model, the aim is to evaluate the maximum vertical displacement suffered by the lens. To obtain this, it has been represented the reaction force of the ground as two forces acting on the contact surface between the pneumatic and the rim.

In this case, the real values of these forces have not been included, it has simply been decided that each of them has a value of 500 N (-Y direction). In addition, it has been fixed the inner diameter of the flange to see the displacement of the rest of the lens (figure 4.42).

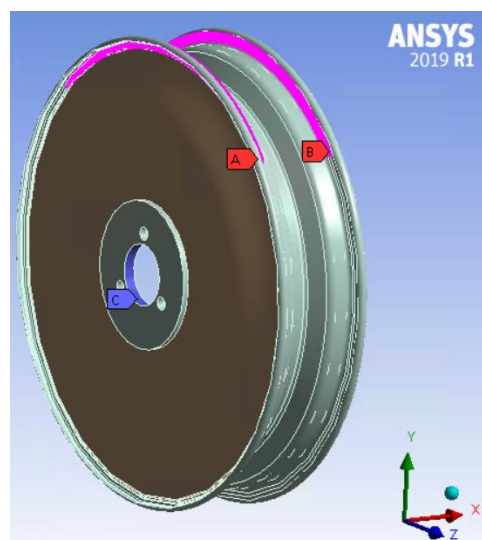


Figure 4.42: Loads & constraints of the radial stiffness simulation.

To obtain a direct comparison between the various simulations, the same boundary conditions have been used, using different lens shapes for each simulation.

### 4.2.1.4.3 Results

#### 4.2.1.4.3.1 Curved lens

The vertical deformation results are shown in figure 4.43. The maximum absolute value is 0.59 mm located in the outer surface of the rim that is not in contact with the lens. The maximum equivalent stress of this model is 31.9 MPa.

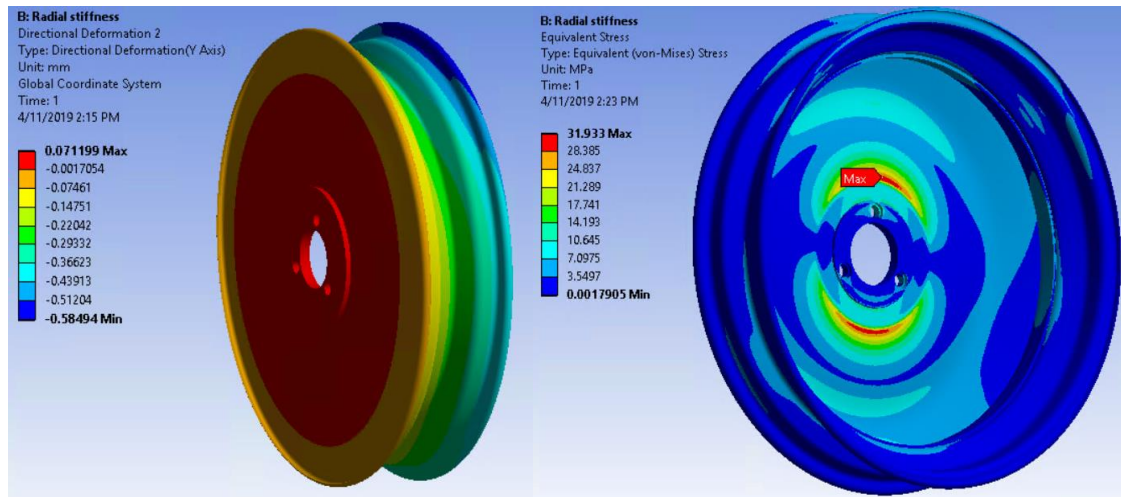


Figure 4.43: Vertical deformation and equivalent stress results of the curved lens.

#### 4.2.1.4.3.2 Straight lens

The maximum deformation for this simulation is 0.84 mm and the maximum equivalent stress is 46.2 MPa (figure 4.44)

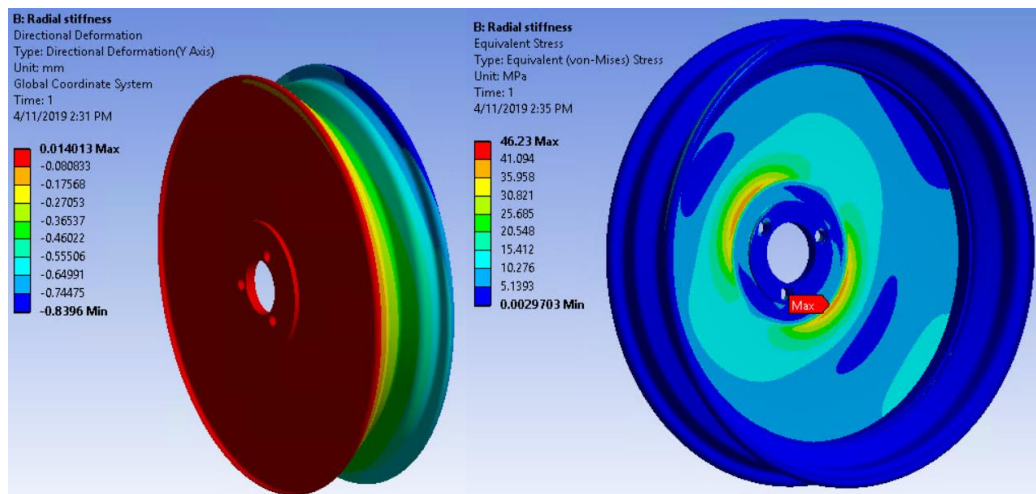


Figure 4.44: Vertical deformation and equivalent stress results of the straight lens.

#### 4.2.1.4.3.3 Straight+angle lens

The maximum displacement is 0.94 mm and the maximum equivalent stress is 61.3 MPa (figure 4.45).

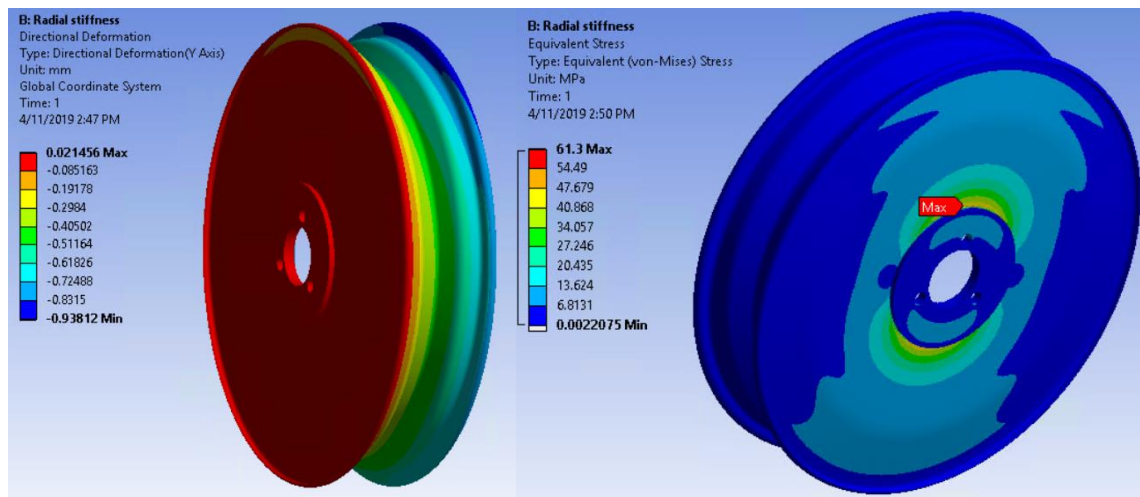


Figure 4.45: Vertical deformation and equivalent stress results of the straight+angle lens.

#### 4.2.1.5.- Bending stiffness simulation comparing different designs

After performing the radial stiffness test, another simulation has been done to understand the performance of these lenses referred to its bending stiffness. This simulation is used to know which lens design has a lower lateral displacement and therefore, to determine which shape is more optimal. Moreover, an equivalent stress analysis has been done to compare all versions.

##### 4.2.1.5.1 Materials

The materials used for this simulation are the same as in the radial stiffness simulation.

##### 4.2.1.5.2 Loads & constraints

In this model, the aim is to evaluate the maximum displacement suffered by the lens. To obtain this, the rotating bending test, carried out at TÜV E/ECE 324 standard [3.2] , has been performed. Thus, the rim is fixed on the vertical surface farthest from the lens and, a bending moment is applied on the axis perpendicular to the axis of revolution of the wheel (figure 4.46). In this case, the magnitude of this moment has an arbitrary value of 100 Nm and has been applied on the back face of the flange (+Z direction).

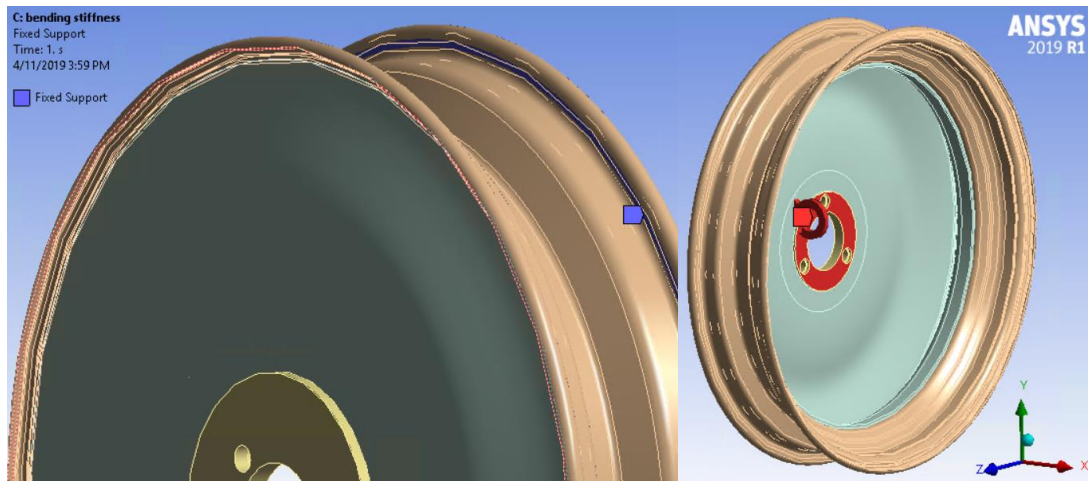


Figure 4.46: Loads and constraints applied in the bending stiffness simulation.

#### 4.2.1.5.3 Results

##### 4.2.1.5.3.1 Curved lens

The maximum total deformation is 0.63 mm and the maximum equivalent stress of this model is 67.7 MPa (figure 4.47).

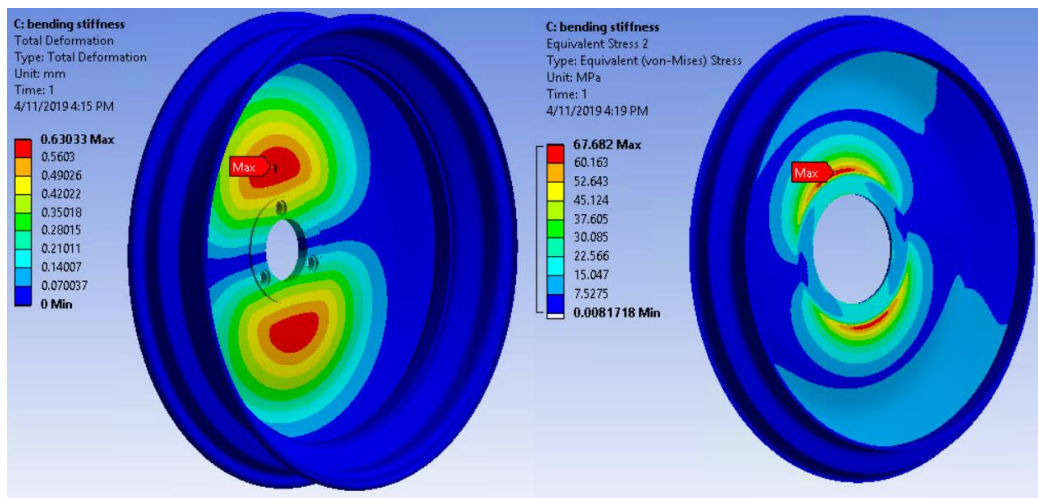


Figure 4.47: Total deformation and equivalent stress results of the curved lens.

##### 4.2.1.5.3.2 Straight lens

The maximum deformation for this simulation is 1 mm. On the other hand, the maximum equivalent stress is 94.8 MPa (figure 4.48).

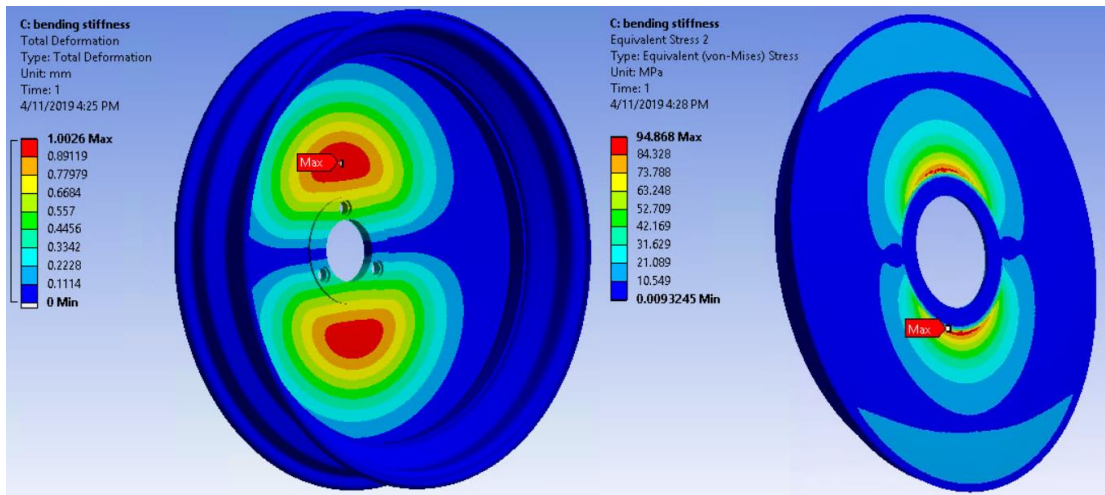


Figure 4.48: Total deformation and equivalent stress results of the straight lens.

#### 4.2.1.5.3.3 Straight+angle lens

The maximum displacement is 1.17 mm and the maximum stress is 111.74 MPa (figure 4.49)

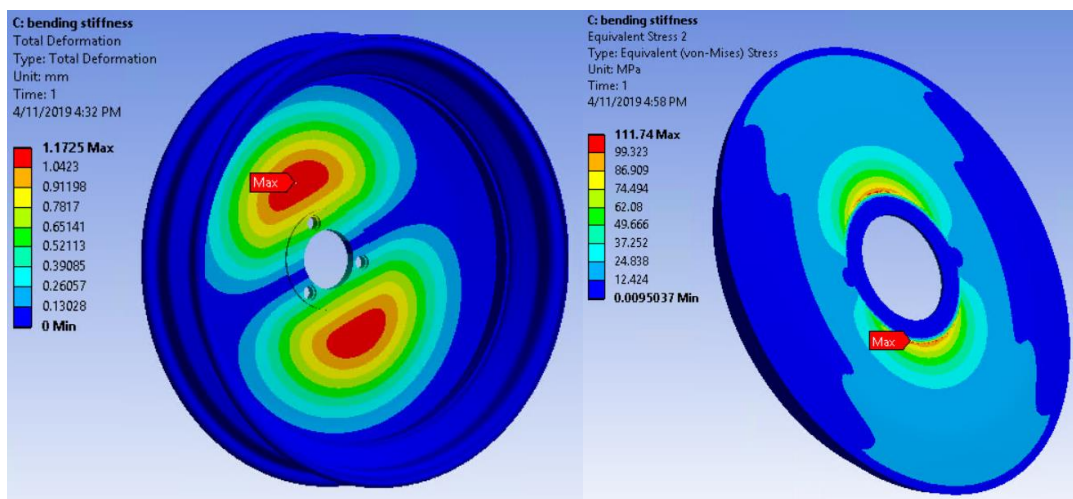


Figure 4.49: Total deformation and equivalent stress results of the straight+angle lens.

#### 4.2.1.6.- Conclusions

To sum up and to have a better compression of the results, table 4.3 and table 4.4 have been done collecting all data from the simulations:

Version	Mass (g)	Thickness (mm)	Shape of the len	Load type	Load value		Max vertical displacement (mm)	Max bending displacement (mm)	Max eq stress radial (MPa)	Max eq stress bending (MPa)
v1.0 (REF)	1035	3	curved (spline)	Radial	1000	N	0.59	-	31.9	-
				Bending	100	Nm	-	0.63	-	67.7
v1.1	1021	3	straight	Radial	1000	N	0.84	-	46.2	-
				Bending	100	Nm	-	1.00	-	94.9
v1.2	1023	3	straight+angle (straight & 10° + R100)	Radial	1000	N	0.94	-	61.3	-
				Bending	100	Nm	-	1.17	-	111.7

Table 4.3: Results summary of each simulation.

Version	Variation % radial compliance	Variation % bending compliance	Variation % stress respect to the reference (radial)	Variation % stress respect to the reference (bending)	Variation % mass respect to the reference
v1.0 (REF)	-	-	-	-	-
	-	-	-	-	-
v1.1	42.4%	-	44.8%	-	-1.4%
	-	58.7%	-	40.2%	-
v1.2	59.3%	-	92.2%	-	-1.2%
	-	85.7%	-	65.0%	-

Table 4.4: Comparison table between simulations.

As it can be observed in table 4.4 the shape that has obtained the best results has been the curved lens. With this configuration, stress and deformation levels are lower than the rest of the versions although it is the heaviest lens.

For these reasons, the curved lens has been chosen as a first approach of the final version. In the following steps, the optimization of this shape type will be done.

#### 4.2.2.- Adhesive bond assessment

Before carrying out the optimization of the final shape of the curved lens, it is necessary to validate the type of union that exists between the flange and the lens.

As it is said before, the union between the flange and the lens is done with an adhesive. Therefore, it must be considered that if the contact area between these two elements is increased, this union will suffer less stress level. Consequently, before starting the optimization of the curved lens, some changes in the flange must be performed to increase this contact area.

In figure 4.50, as it can be observed, an increment of the external diameter of the flange has been done to reach this purpose. On the other hand, some holes have been done to reduce its weight.

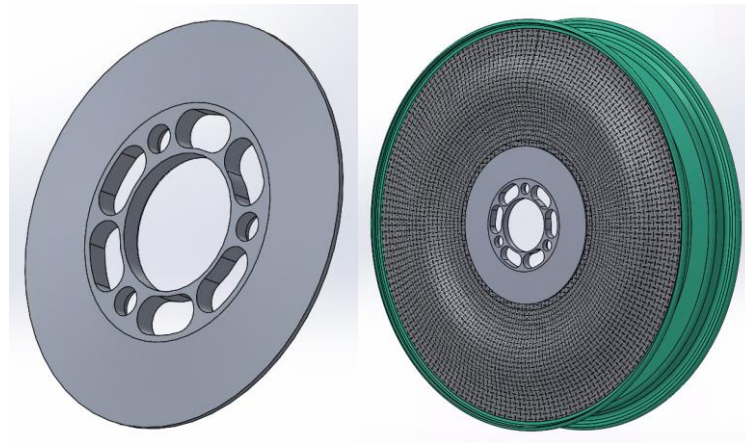


Figure 4.50: New design of the flange included in the wheel assembly.

The next step is to analyse the stress distribution in the glued area to determine if this type of union is possible or not. As it is known, adhesives have a good performance when they work supporting shear loads, but in this case, the loads produce bending moments which try to separate these two elements. For this reason, a stress analysis has been performed in the contact area between these two pieces.

For this simulation, it has been only studied the bending stiffness case keeping all boundary conditions equal to previous simulations. The only difference is that, for this simulation, it has been included the maximum bending moment acting on the wheel (730 Nm).

#### 4.2.2.1.- Results

In figure 4.51 it is shown the stress distribution on the contact surfaces between the flange and the lens:

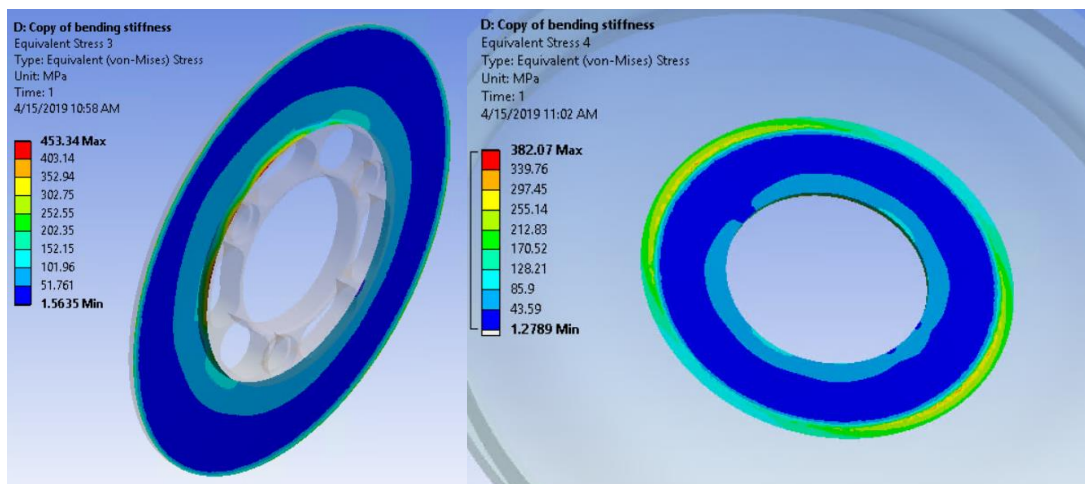


Figure 4.51: Equivalent stress results on the flange and lens contact surfaces.

As it can be observed in the results, the stresses in some regions are too high to be supported by an adhesive, therefore, an alternative solution has to be done to solve this problem.

#### 4.2.3.- New contact bond between flange and lens

The solution that has been done to solve this problem is to integrate the lens component with the bushes and pins already used in the wheel housing. The adhesive between the flange and the lens is still maintained but, in this case, the rotation movement is transmitted by the pins. Moreover, this solution avoids separation problems due to the bending load acting on the wheel. To perform this, a new flange, which is just a simple plate, has been designed (figure 4.52).

After the production of the lens, this plate will be glued to the lens using an adhesive, and finally, drilled together to locate the bushes inside.

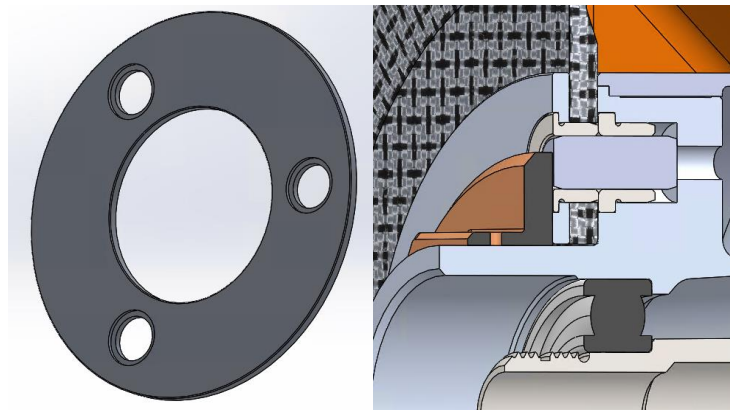


Figure 4.52: Final design of the flange in the final wheel assembly.

#### 4.2.4.- Shape optimization of the curved lens

In this section, it has been done the shape optimization of the curved lens. To avoid problems with the CAD file, the spline used for the first approach has been replaced by several tangent circles trying to maintain its original curvature (v2.0).

To optimize this shape, different lens versions have been done only changing some parameters of the original one to compare them. These parameters are the main circumference diameter of the sketch and the location of its center with respect to the origin.

In figure 4.53, it is shown the complete sketch of the v2.0 design. In this case, the diameter of the circumference is 90 mm and its location respect to the origin is (11.80,145)

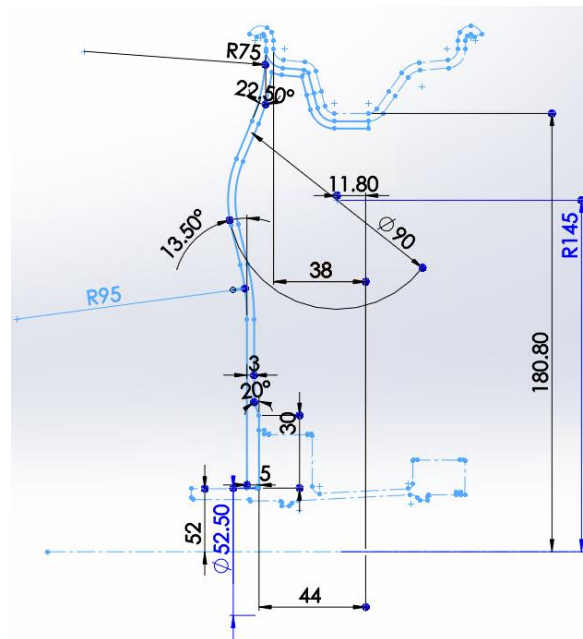


Figure 4.53: Sketch of the lens v2.0.

Below, in table 4.5, the different versions of the lenses are shown with its corresponding parameters:

Version	Shape of the lens
v2.0 (REF)	as the curved (spline) but with circles (D90, 11.8, 145)
v2.1	D90, 12, 140
v2.2	D100, 3, 132
v2.3	D90, 12, 145

Table 4.5: Parameters of the different shapes.

The next step is to perform different simulations to compare all the results. To do this, it has been only studied the bending stiffness case keeping all boundary conditions as in previous simulations. The results and conclusions are shown in the following paragraphs.

#### 4.2.4.1.- Results

##### 4.2.4.1.1 v2.0

In this case, the stresses that must be analysed to determine which lens is better, are the stresses located in the section where the lens suffers more due to the bending moment. This region is located closed to the lens inner circumference. The maximum stress located on

that region is approximately 94.3 MPa with a maximum total deformation of 0.82 mm (figure 4.54).

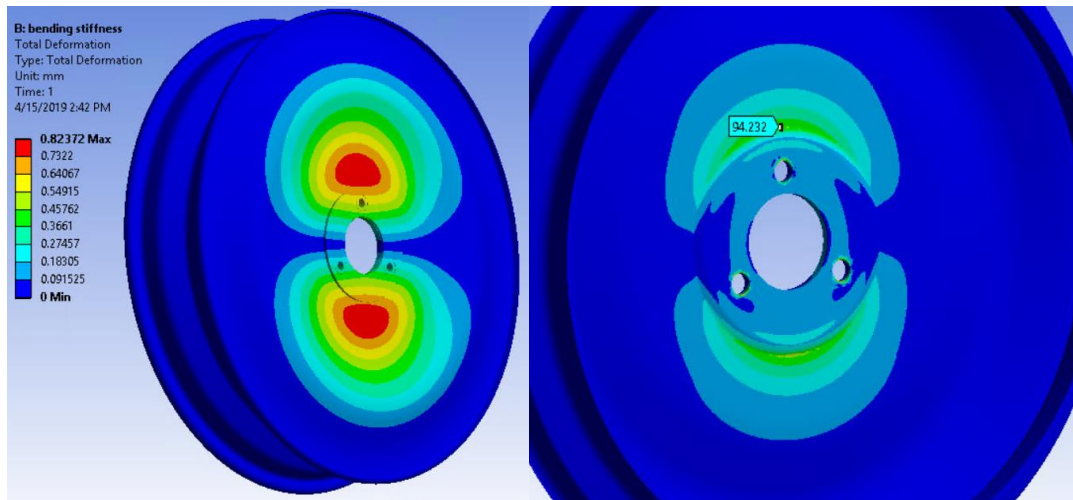


Figure 4.54: Total deformation and equivalent stresses results in v2.0.

#### 4.2.4.1.2 v2.1

The maximum deformation is almost 0.73 mm and the equivalent stress has an approximately value of 88.5 MPa (figure 4.55).

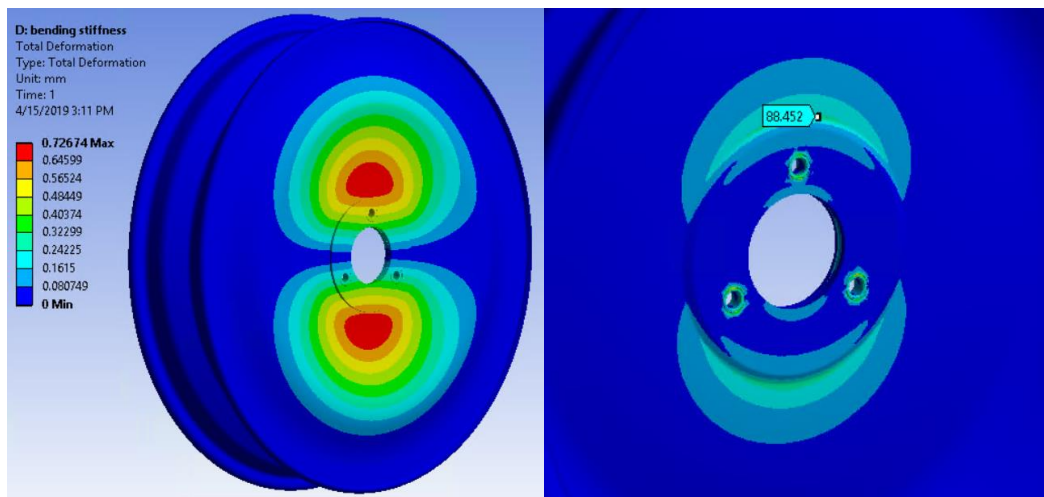


Figure 4.55: Total deformation and equivalent stress results in v2.1.

#### 4.2.4.1.3 v2.2

In this case, the maximum total deformation is almost 1.02 mm and the equivalent stress has a value of 109.3 MPa (figure 4.56):

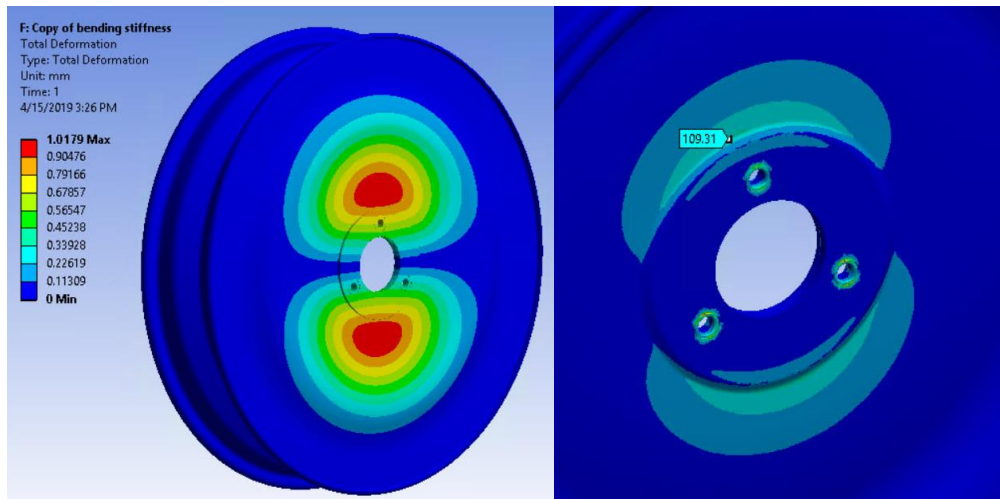


Figure 4.56: Total deformation and equivalent stress results in v2.2.

#### 4.2.4.1.4 v2.3

The maximum total deformation is approximately 0.75 mm and the equivalent stress in that region has a maximum value of 89.01 MPa (figure 4.57).

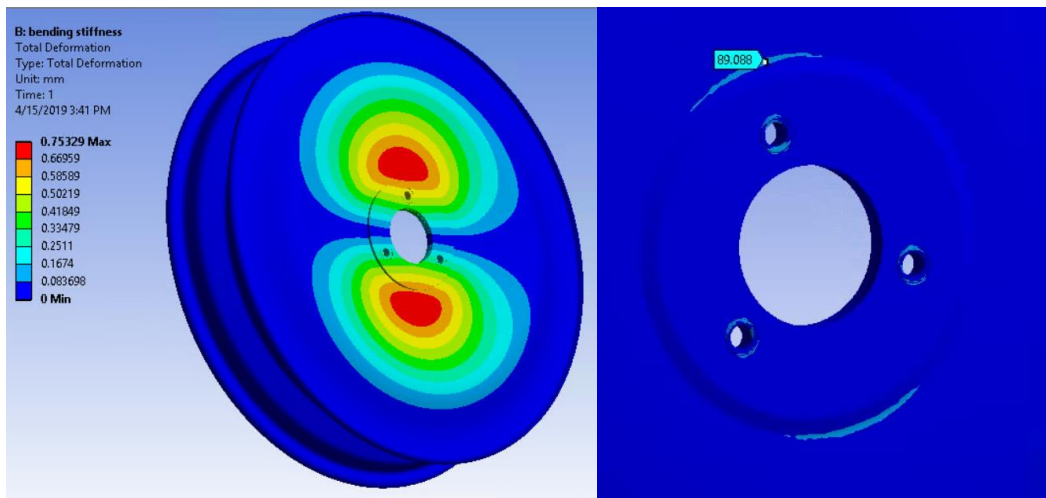


Figure 4.57: Total deformation and equivalent stress results in v2.3.

#### 4.2.4.2.- Conclusions

In table 4.6 and table 4.7, all the results have been collected to compare the different versions of the lenses.

Version	Shape of the lens	Load type	Load value		Max bending displacement (mm)	Max eq stress bending (MPa)
v2.0 (REF)	as the curved (spline) but with circles (D90, 11.8, 145)	Radial	1000	N	-	-
		Bending	100	Nm	0.82	94.3
v2.1	D90, 12, 140	Radial	1000	N	-	-
		Bending	100	Nm	0.73	88.5
v2.2	D100, 3, 132	Radial	1000	N	-	-
		Bending	100	Nm	1.02	109.3
v2.3	D90, 12, 145	Radial	1000	N	-	-
		Bending	100	Nm	0.75	89.1

Table 4.6: Result comparisons between different lens versions.

Version	Variation % bending compliance	Variation % stress respect to the reference (bending)	Variation % mass respect to the reference
v2.0 (REF)	-	-	-
	-	-	-
v2.1	-11.0%	-6.2%	-0.3%
v2.2	24.4%	15.9%	-0.9%
v2.3	-8.5%	-5.5%	-0.9%

Table 4.7: Variations between different lens shapes.

As it can be observed in the previous tables, the best solution in terms of displacement and stresses is the v2.1. However, it has been decided to take the version v2.3 as the final shape of the lens because it is lighter than the v2.1 although its results are not the best.

Since the final shape of the lens has already been decided, the next step is to determine the rim and lens plybooks.

# 5.- COMPOSITE COMPONENTS

## OPTIMIZATION

### 5.1.- COMPOSITE MATERIALS

#### 5.1.1.- Composite material definition

A composite material is a heterogeneous material consisting of two or more materials combined at a macroscopic level and not soluble in each other, whose resulting mechanical and physical properties are designed to be superior to those of their individual constituents.

The usual composite materials have two different components (figure 5.1):

- Reinforcement: discontinuous and resistant phase.
- Matrix: continuous and less resistant phase that bond the reinforcement.

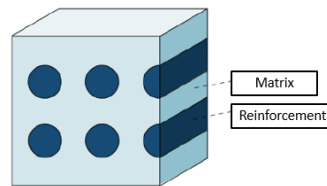


Figure 5.1: Simple structure of a composite material. [52]

#### 5.1.2.- Classification of composite materials

The most used classification of composite materials is the one that is related to shape and orientation of the reinforcement (figure 5.2).

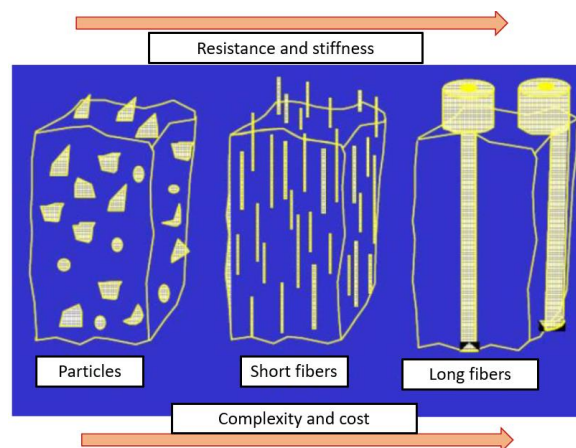


Figure 5.2: Classification of composite materials related to shape and orientation of the reinforcement. [52]

### 5.1.2.1.- Particle reinforced composite

In these types of composite materials, the increase in mechanical properties is very limited since the load is transmitted equally between the matrix and the reinforcement. Moreover, in these materials, the increase in stiffness and strength is in all directions (isotropic).

Some examples of particle reinforced composite materials are talc, silica, glass, rubber...

### 5.1.2.2.- Reinforced composite with short fibers

For these materials, the increase in stiffness and resistance in the case of random alignment is in all directions (isotropic). In these materials, the increase in mechanical properties is greater than the previous composite type but it is still low.

Inside this category, some examples of reinforced composite materials with short fibers are glass fiber, carbon fiber (SMC)...

### 5.1.2.3.- Reinforced composite with long fibers

In this case, the fiber length is comparable with the size of the artefacts. For these composite materials (figure 5.3), it can be assumed that the load applied in the fiber parallel direction is entirely supported by them.

On the other hand, the function of the matrix is to hold the fibers together and distribute the load between them as well as protecting the fibers from environmental and corrosive agents.

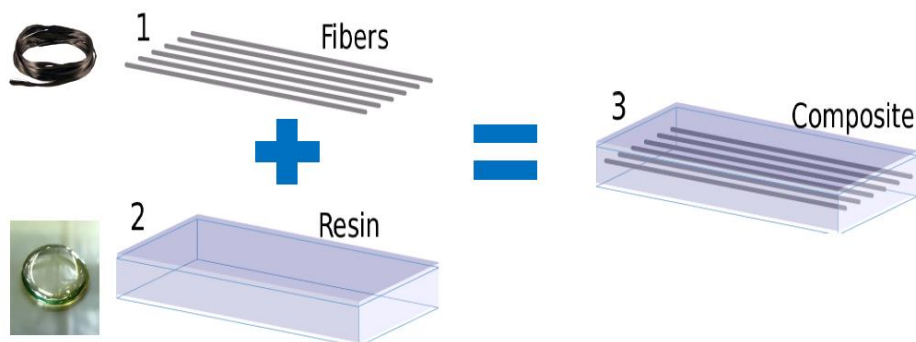


Figure 5.3: Structure of a reinforced composite with long fibers. [52]

There are two types of long fiber composites depending on the number of layers used to form them:

#### 5.1.2.3.1 Ply

Fibers aligned in a specific direction and incorporated in the matrix forming an element considered as a single sheet. This single sheet is very strong in the parallel direction of the

fibers but has low resistance in the transversal one since the loads are only supported by the matrix (orthotropic material).

#### 5.1.2.3.2 Composite laminate

It is produced stacking some sheets in different directions (figure 5.4). Depending on the orientation of the different sheets, a composite laminate can be obtained with more or less balanced stiffness and resistance in different directions (anisotropic material).

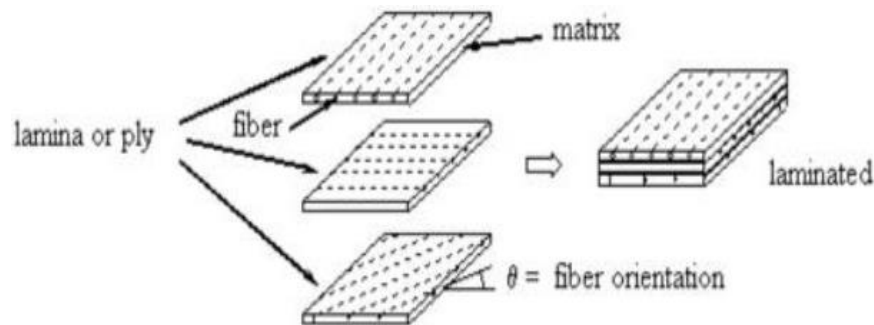


Figure 5.4: Example of a composite laminate. [52]

##### 5.1.2.3.2.1 Advantages of composite laminates

The main advantages of the composite laminates are described below:

- Versatility to design laminates with different stiffness and strength in the different directions based on the specifications required by the project.
- Almost no thermal expansion in the direction of the carbon fibers.
- Flexibility to generate laminated components with complex shapes with a low cost.
- Excellent corrosion and fatigue resistance.
- Low initial investment cost to build a production plant for composite laminates.

##### 5.1.2.3.2.2 Disadvantages of composite laminates

Although these materials have many advantages, they also have negative aspects that must be considered:

- The anisotropy characteristics of the laminate requires a complex planning design.
- Low resistance to loads applied outside of the laminate plane. These laminates are not suitable for geometries subjected to three-dimensional loads or shear stresses.
- Limited maximum operating temperature (up to 120-250 °C).
- High variability of the mechanical properties due to the poor repeatability of the process.
- Brittle and catastrophic failure (no ductile material).

- It is difficult to assess the occurrence of damage (before it is catastrophic) through non-destructive inspection techniques.

### 5.1.3.- FRP materials

Long fiber composite materials and polymer matrix (Fiber Reinforced Plastic, FRP) are obtained by combining high stiffness and strength fibers called reinforcement, with a weaker polymeric matrix:

- Reinforcement: Glass fiber, carbon o Kevlar ( $\varnothing$  720  $\mu\text{m}$ )
- Matrix:
  - Termosetting: Epoxy, polyester, vinyl, polyamide...
  - Termoplastic: PEEK, Nylon...

As it can be seen in figure 5.5, the high strength and specific stiffness of these composites is linked to the high strength and stiffness of the fibers. Despite this, the fibers cannot be used individually because they cannot support compressive loads (buckling) and shear loads. The function of the matrix is to bind the fibers together by supporting them laterally (preventing them from buckling) and to transmit the load between them.

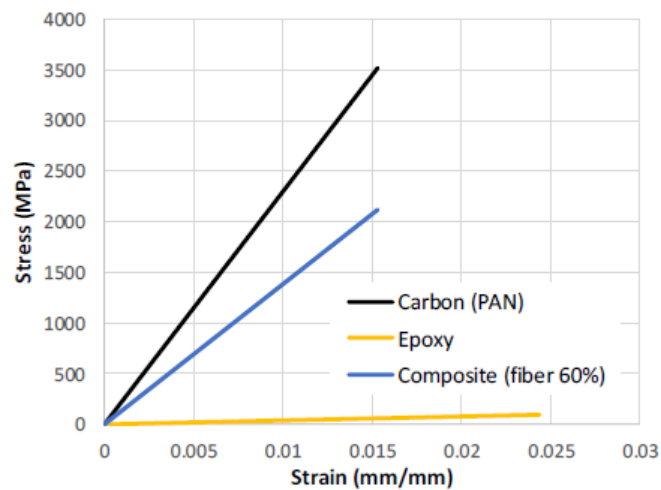


Figure 5.5: Stress-strain curves comparison. [52]

### 5.1.4.- Prepregs

Prepregs are composite materials in which a fiber is pre-impregnated with a thermoset or thermoplastic resin matrix in a certain ratio. Prepregs have singular properties since they are cured under high pressures and temperatures. These are materials used to do the Emilia 4 composite wheel.

Frequently, the resin matrix in prepregs is not completely cured for easy handling and is kept in a cool place to prevent the complete polymerization. This prepreg will need to be heated in an oven or autoclave to obtain a full polymerization during the manufacturing process. The reinforcement in a prepreg can be a fabric or unidirectional fibers (figure 5.6): [53]

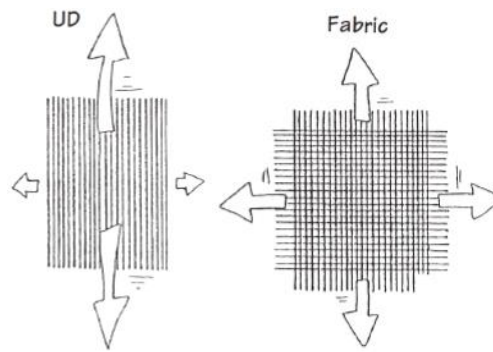


Figure 5.6: Different types of prepregs [52]

- Unidirectional fibers (UD): these fibers are oriented in a single direction and have superior mechanical characteristics compared with fabrics. In addition, its cost is lower since there is no weaving process.
- Fabrics: the fibers are woven to form a bidirectional reinforcement. These materials have a great ease of handling, a good adaptability to complex surfaces and a superior tolerance to damage and impact compare with unidirectional fibers.

Within the fabrics, there are different weaving patterns with different characteristics (figure 5.7):

- Drapeability: ability to cover (adapt) surfaces with double curvature.
- Crimp: fiber curvature with consequent reduction of mechanical properties.

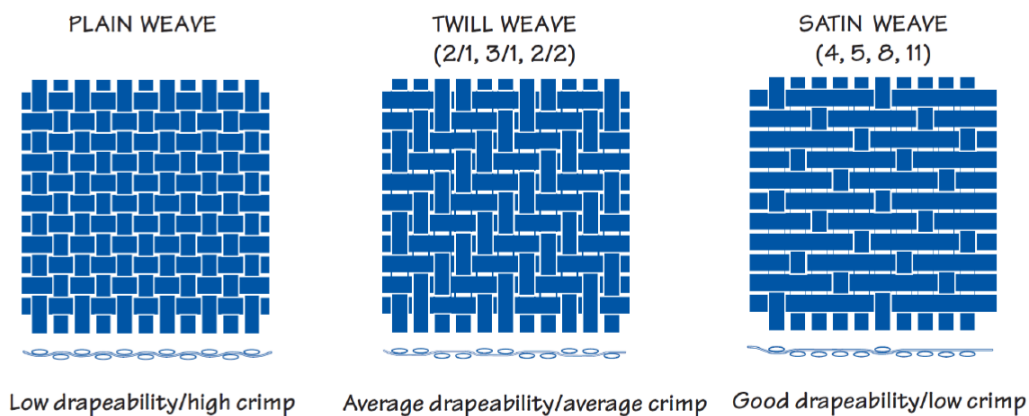


Figure 5.7: Most common fabrics used with different weaving patterns. [52]

### 5.1.5.- Failure criteria

The prediction of the mechanical resistance of the lamina by micromechanics is often imprecise and not very reliable. Therefore, it is more reliable to perform experimental tests on individual laminae in the main directions of the main reference system, distinguishing between tension and compression (figure 5.8). In spite of this, only the classical theories of failure of composite materials have been used since there has not been enough time to perform experimental tests directly with the real wheel components.

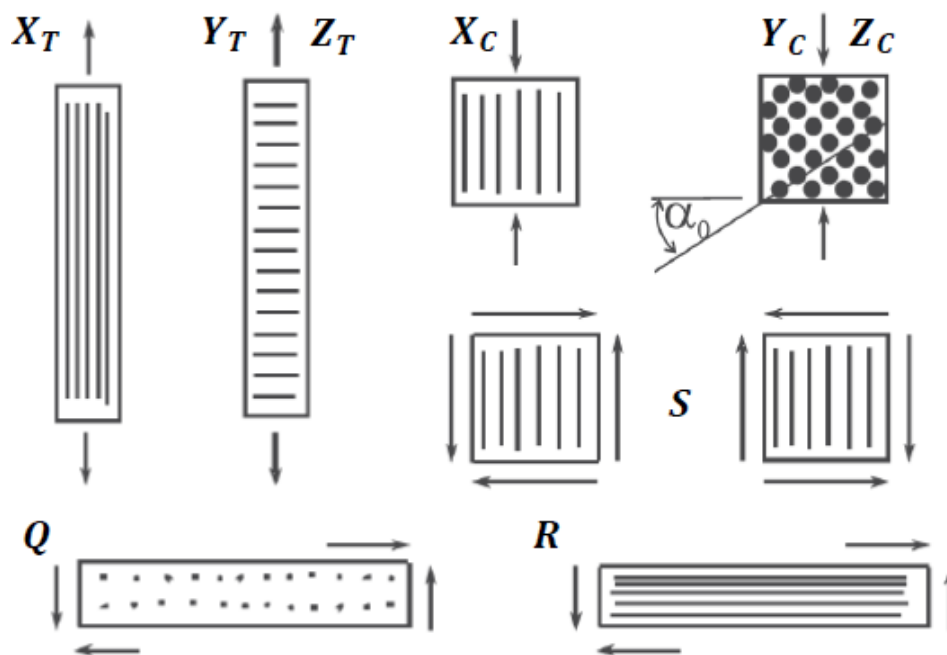


Figure 5.8: Different experimental tests of tension and compression. [52]

- $X$ ,  $Y$  and  $Z$ : ultimate resistance to normal stresses in the fibers direction (1) and transversal (2) and (3).
- $S$ ,  $Q$  and  $R$ : the ultimate resistance to shear stresses in the plane (1-2) and perpendicular to it (2-3) and (1-3).
- $T$  and  $C$  distinguish between tension and compression.

#### 5.1.5.1.- Tsai-Hill criterion

In this criterion [54], either compressive or tensile strengths are used to determine the  $F$  coefficients depending on the loading condition. These coefficients are calculated as follows:

$$F_{11} = \frac{1}{X^2}$$

$$F_{22} = \frac{1}{Y^2}$$

$$F_{44} = \frac{1}{Q^2}$$

$$F_1 = 0$$

$$F_2 = 0$$

$$F_{55} = \frac{1}{R^2}$$

$$F_{12} = -\frac{1}{2X^2}$$

$$F_{66} = \frac{1}{S^2}$$

Where X and Y values are:

$$\sigma_1 \geq 0 \Rightarrow X = X_t$$

$$\sigma_1 < 0 \Rightarrow X = X_c$$

$$\sigma_2 \geq 0 \Rightarrow Y = Y_t$$

$$\sigma_2 < 0 \Rightarrow Y = Y_c$$

The Tsai-Hill criterion differentiates between woven plies and UD. The UD Tsai-Hill criterion can be written as follows:

$$f = \left(\frac{\sigma_1}{X}\right)^2 + \left(\frac{\sigma_2}{Y}\right)^2 + \left(\frac{\tau_{12}}{S}\right)^2 - \frac{\sigma_1\sigma_2}{X^2}$$

For woven plies, the function becomes:

$$f = \left(\frac{\sigma_1}{X}\right)^2 + \left(\frac{\sigma_2}{Y}\right)^2 + \left(\frac{\sigma_{12}}{S}\right)^2 - 2H\sigma_1\sigma_2$$

$$H = \frac{1}{2} \left( \frac{1}{X^2} + \frac{1}{Y^2} \right)$$

For a full 3-D case, another formulation is used [55]:

$$(G+H)\sigma_1^2 + (F+H)\sigma_2^2 + (F+G)\sigma_3^2 - 2H\sigma_1\sigma_2 - 2G\sigma_1\sigma_3 - 2F\sigma_2\sigma_3 \dots \\ + 2L\tau_{23}^2 + 2M\tau_{13}^2 + 2N\tau_{12}^2 = 1$$

where

$$F = \frac{1}{2} \left( -\frac{1}{X^2} + \frac{1}{Y^2} + \frac{1}{Z^2} \right)$$

$$G = \frac{1}{2} \left( \frac{1}{X^2} - \frac{1}{Y^2} + \frac{1}{Z^2} \right)$$

$$H = \frac{1}{2} \left( \frac{1}{X^2} + \frac{1}{Y^2} - \frac{1}{Z^2} \right)$$

### 5.1.5.2.- Tsai-Wu criterion

For the plane stress-state, the F coefficients for the Tsai-Wu criterion [56] have the following values:

$$F_{11} = \frac{1}{X_t X_c}$$

$$F_{22} = \frac{1}{Y_t Y_c}$$

$$F_{44} = \frac{1}{Q^2}$$

$$F_{66} = \frac{1}{S^2}$$

$$F_1 = \frac{1}{X_t} - \frac{1}{X_c}$$

$$F_2 = \frac{1}{Y_t} - \frac{1}{Y_c}$$

$$F_{55} = \frac{1}{R^2}$$

Therefore, this criterion can be formulated as follows:

$$f = \frac{\sigma_1^2}{X_t X_c} + \frac{\sigma_2^2}{Y_t Y_c} + \frac{\tau_{23}^2}{Q^2} + \frac{\tau_{13}^2}{R^2} + \frac{\tau_{12}^2}{S^2} + \left( \frac{1}{X_t} - \frac{1}{X_c} \right) \sigma_1 + \left( \frac{1}{Y_t} - \frac{1}{Y_c} \right) \sigma_2 + 2F_{12} \sigma_1 \sigma_2$$

The  $F_{12}$  can't be obtained directly from uniaxial load cases studying its failure stresses. For more accurate results it should be calculated through biaxial load tests.

### 5.1.5.3.- Hashin criterion

In this criterion [57], the expression which predicts the criticality of tensile loads in the fiber direction is formulated as follows:

$$2\text{-D: } f_f = \left( \frac{\sigma_1}{X_t} \right)^2 + \left( \frac{\tau_{12}}{S} \right)^2, \quad \sigma_1 \geq 0$$

$$3\text{-D: } f_f = \left( \frac{\sigma_1}{X_t} \right)^2 + \left( \frac{\tau_{12}}{S} \right)^2 + \left( \frac{\tau_{13}}{R} \right)^2, \quad \sigma_1 \geq 0$$

The failure is predicted with an independent stress condition if there are compressive loads in the fiber direction:

$$f_f = -\frac{\sigma_1}{X_c}, \quad \sigma_1 < 0$$

In the case of tensile transverse stress, the formulation for predicting matrix failure is:

$$2\text{-D: } f_m = \left(\frac{\sigma_2}{Y_t}\right)^2 + \left(\frac{\tau_{12}}{S}\right)^2, \quad \sigma_2 \geq 0$$

$$3\text{-D: } f_m = \left(\frac{\sigma_2}{Y_t}\right)^2 + \left(\frac{\tau_{23}}{Q}\right)^2 + \left(\frac{\tau_{12}}{S}\right)^2 + \left(\frac{\tau_{13}}{R}\right)^2, \quad \sigma_2 \geq 0$$

When the transverse stress is compressive, a more complex expression is used:

$$2\text{-D: } f_m = \left(\frac{\sigma_2}{2S}\right)^2 + \left(\frac{\tau_{12}}{S}\right)^2 + \left[\left(\frac{Y_c}{2S}\right)^2 - 1\right] \frac{\sigma_2}{Y_c}, \quad \sigma_2 < 0$$

$$3\text{-D: } f_m = \left(\frac{\sigma_2}{2Q}\right)^2 + \left(\frac{\tau_{23}}{Q}\right)^2 + \frac{\tau_{12}^2}{S^2} + \left[\left(\frac{Y_c}{2Q}\right)^2 - 1\right] \frac{\sigma_2}{Y_c}, \quad \sigma_2 < 0$$

Delamination (compression and tension) is predicted with the following formula:

$$3\text{-D: } f_d = \left(\frac{\sigma_3}{Z}\right)^2 + \left(\frac{\tau_{13}}{R}\right)^2 + \left(\frac{\tau_{23}}{Q}\right)^2$$

The most critical of the failure modes is selected under the following condition:

$$f = \max(f_f, f_m, f_d)$$

#### 5.1.5.4.- Maximum Stress criterion

In this criterion [58], considering the ply principal coordinate system, the ratios of the actual stresses to the failure stresses are compared. Thus, the failure function is:

$$f = \max\left(\left|\frac{\sigma_1}{X}\right|, \left|\frac{\sigma_2}{Y}\right|, \left|\frac{\sigma_3}{Z}\right|, \left|\frac{\tau_{12}}{S}\right|, \left|\frac{\tau_{13}}{R}\right|, \left|\frac{\tau_{23}}{Q}\right|\right)$$

where

$$\sigma_1 \geq 0 \Rightarrow X = X_t \quad ; \quad \sigma_1 < 0 \Rightarrow X = X_c$$

$$\sigma_2 \geq 0 \Rightarrow Y = Y_t \quad ; \quad \sigma_2 < 0 \Rightarrow Y = Y_c$$

$$\sigma_3 \geq 0 \Rightarrow Z = Z_t \quad ; \quad \sigma_3 < 0 \Rightarrow Z = Z_c$$

### 5.1.6.- Manufacturing process

The choice of the manufacturing method is one of the first considerations to do in the design of a composite component or structure. The designer must understand which method is the most suitable on each particular case. This means to know all the advantages, disadvantages, costs and production volumes of each manufacturing process.

The production of a composite material requires the following operations:

- Positioning of the fiber oriented according to the required directions.
- Impregnation of the fibers using resin.
- Consolidation of the impregnated elements to remove excess of air, resin and volatile substances.
- Polymer solidification or cure.
- Extraction of the composite from the mold.
- Cutting and final operations.

The different processes differ in the way that these operations are performed but, in any case, all of these must be done.

Below, only the vacuum bag molding cured in Autoclave is explained since that is the method used to manufacture the Emilia 4 composite wheels.

The vacuum bag molding technique (figure 5.9) allows the production of large composites components of any shape with a low cost and high quality. The main steps to perform this technique are the following:

- The fiber is laid on the mold and the resin is distributed. If a prepreg is used, it can be directly laid on the mold without adding resin.
- A film or release element is placed on both sides of the laminate to prevent it from sticking to the mold.
- The breather or bleeder is placed over it to distribute the vacuum.
- Finally, the laminate is covered with a flexible bag, which perfectly seals the mold.

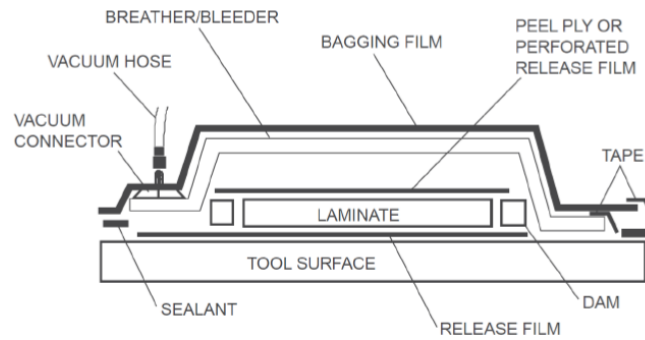


Figure 5.9: Components used in the vacuum bag molding technique. [52]

The main advantage of this method is that, applying the vacuum, atmospheric pressure acts on the composite compacting it uniformly and also helps to remove resin residual solvent and air.

After this process, the autoclave curing is performed to obtain the final composite component. Autoclave curing process of composite materials is an extension of the vacuum bag technique in which a higher pressure is used (figure 5.10).

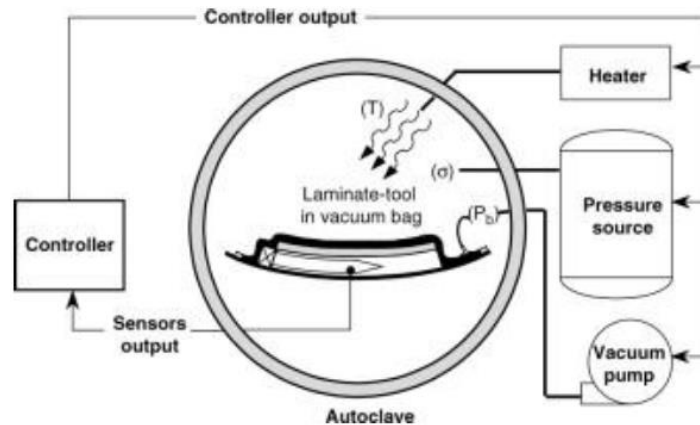


Figure 5.10: Autoclave curing process. [52]

The main steps to perform this curing process are the following:

- The composite is placed with the mold and the vacuum bag in an autoclave.
- The vacuum is applied to the bag and externally a higher pressure than the atmospheric one. The temperature is increased in order to start the curing process (the resin curing).

The biggest advantage of this method is that by applying a higher pressure than the atmospheric one, a greater compaction is achieved.

The boundary conditions applied during the Autoclave curing process are defined by the cure cycle. This describes the evolution of the variables that are involved in the process. In figure 5.11, it is shown the graph which describes a typical cure cycle for a thermosetting matrix prepreg.

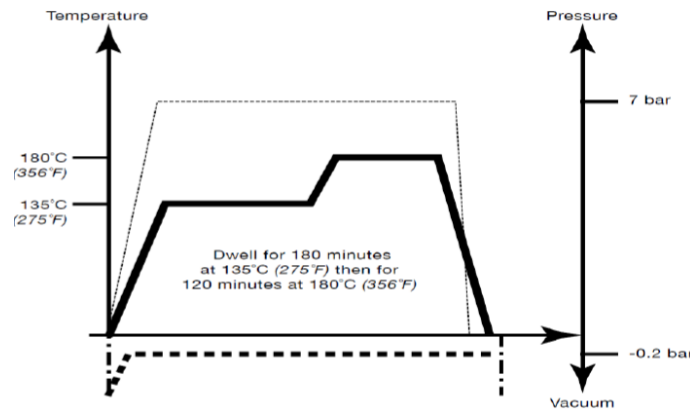


Figure 5.11: Cure cycle. [52]

This cycle has the following phases:

- Vacuum and pressure: during the entire cycle, the vacuum and a pressure between 4 and 7 bar are applied.
- Cure: once the cure temperature has been reached (between 80-150 °C) the resin impregnates the fibers.
- Post-cure: phase not always necessary in which the temperature is increased further in order to decrease any possible residual stresses.

## 5.2.- COMPOSITE DESIGN & DOE

### 5.2.1.- Rim design & plybook

The rim shape selected for this wheel is the WSC Michelin tire 95-80 R16 (figure 5.12). This rim is only used to produce custom wheels for solar races on public roads.

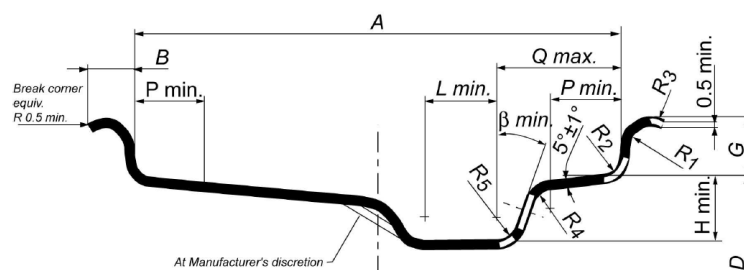
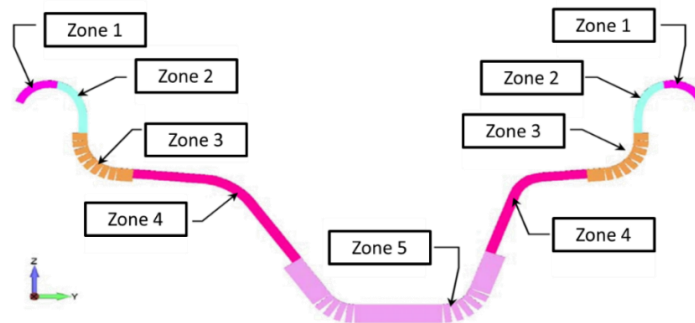


Figure 5.12: WSC Michelin rim 95-80 R16 dimensions. [42]

In table 5.1, it is shown the lamination sequence of the rim used in the previous version of the Emilia 4 vehicle. As it can be observed, this sequence had been done performing a differentiated lamination in which it is possible to distinguish several different zones in the shape of the rim. Thus, each of these zones had a different thickness with a different stacking lamination.

Despite being a very optimized tire in terms of thickness, during the American Solar Challenge competition, an important problem had been observed. There was a considerable loss of the tire pressure due to the appearance of cracks in the fibers.

As it can be observed in the stacking lamination, only two plies of Twill had been used, one at the beginning and one at the end of the process. In the intermediate zone, there were only unidirectional fibers, where if a crack is formed, it would be propagated easily through these fibers.



Lamination sequence	Zone 1	Zone 2	Zone 3	Zone 4	Zone 5
	n° plies / ply type / ° respect to the circumferencial direction				
↑	1 Twill T300 200g 145x1350 (0°/90°)				
					2 UD M40J 90°
				1 UD M40J 90°	
			2 UD T800 0°		
		2 UD M40J 0°		4 UD T800 90°	
			2 UD T800 90°		
			2 UD T800 0°		
			2 UD T800 90°		
		3 UD M40J 0°		2 UD T800 0°	
	8 UD T800 90°				
1 Twill T300 200g 145x1350 (0°/90°)					
Mold surface					
Thickness of different zones	1.65	1.58	2	2.21	2.63
	Zone 1	Zone 2	Zone 3	Zone 4	Zone 5

Table 5.1: Plybook of the old rim.

For this reason, a new study of the lamination sequence has been carried out. In this case, a possible alternative has been made using FEM tools for composite materials. In table 5.2, the plybook of the first version of the rim stacking lamination is shown:

Lamination sequence	n° plies	RIM PLYBOOK	
		ply type	/ ° respect to the circumferencial direction
	1	Twill T300 200g (0°)	
	2	UD M40J (0°)	
	1	Twill T300 200g (0°)	
	2	UD M40J (90°)	
	1	Twill T300 200g (0°)	
	3	UD M40J (90°)	
	1	Twill T300 200g (0°)	
	3	UD M40J (90°)	
	1	Twill T300 200g (0°)	
			Mold surface
n° tot plies	15		
Thickness	3.25	mm	

Table 5.2: Rim plybook v1.0.

This rim plybook shown above has been done considering some important aspects:

- The composite materials used to produce this piece are:
  - Unidirectional fiber M40J.[59]
  - T300 Twill.[60]
- All the plies cover the entire surface of the rim.
- Two different orientations of the fibers have been decided:
  - 0° (following the circumferencial direction of the rim).
  - 90° (transverse direction which is coincident with the wheel axis).
- It is preferable to place the UD M40J 90° near the surface of the mold to increase the rim stiffness due to the pressures acting on it. The UD M40J 0° and UD M40J 90° have a different coefficient of thermal expansion, which may produce gaps between them if they are grouped together during the curing process.
- All UD M40J layers are covered by two plies of Twill T300 in the intermediate plies. In this way, if a crack is formed, it is easier to stop its propagation.
- It is necessary to apply a greater number of UD M40J 90° than UD M40J 0° in the lamination process. This is due to the existence of stresses in the transverse direction that could make a separation between the UD M40J 0° resin and its fibers.
- The plies have been stacked as much symmetrically as possible to prevent warping.

**5.2.2.- Lens design & plybook**

In table 5.3, it is described the first version of the lamination process of the lens:

Ply type	N° of plies	Orientation	Zone
Twill T300	1	0° (R1)	All the external part of the lens (Lens1)
UD M40J	3 (x5 radius)	radial	Radius of the lens
Twill T300	1	144° (R3)	All the external part of the lens (Lens1)
Ply type	N° of plies	Orientation	Zone
UD M40J	3 (x5 radius)	radial	Radius of the lens
Twill T300	1	288° (R5)	All the internal part of the lens (Lens2)
UD M40J	3 (x5 radius)	radial	Radius of the lens
Twill T300	1	72° (R2)	All the internal part of the lens (Lens2)
UD M40J	3 (x5 radius)	radial	Radius of the lens
Twill T300	1	216° (R4)	All the internal part of the lens (Lens2)

Table 5.3: Lens plybook v1.0.

The lamination process of the lens has been done considering these aspects:

- The blue table represents the plies that must be applied to obtain the Lens1 surface. On the other hand, the orange table represents the plies that are included in the Lens2 surface. These two surfaces will be described later in detail.
- As it can be seen in the lens plybook, the ply types used are the same to produce the rim.
- Twill T300 plies orientation have been decided following a circular pattern described in figure 5.13. These plies are applied on the entire surface of the lens.

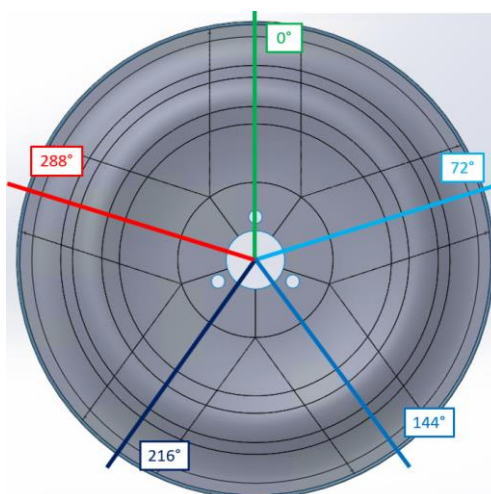


Figure 5.13: Orientation of the Twill T300 plies.

- UD M40J plies are applied on the red areas shown in figure 5.14:

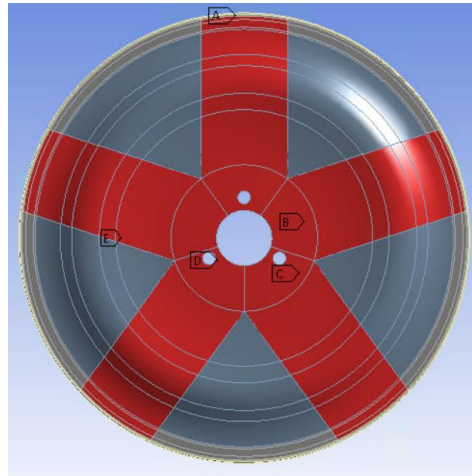


Figure 5.14: Region where UD M40J plies are applied.

- All UD M40J layers are covered by two plies of Twill T300 as in the rim plybook.
- As in the case of the rim plybook, this is a first version of the stacking sequence that needs to be validated using FEM simulations.

#### 5.2.2.1.- Detailed lamination process of the lens

Considering that the shape of the lens is more complex and therefore its lamination process is more complicated to carry out, the scheme of the figure 5.15 has been done for a better compression of the manufacturing process:

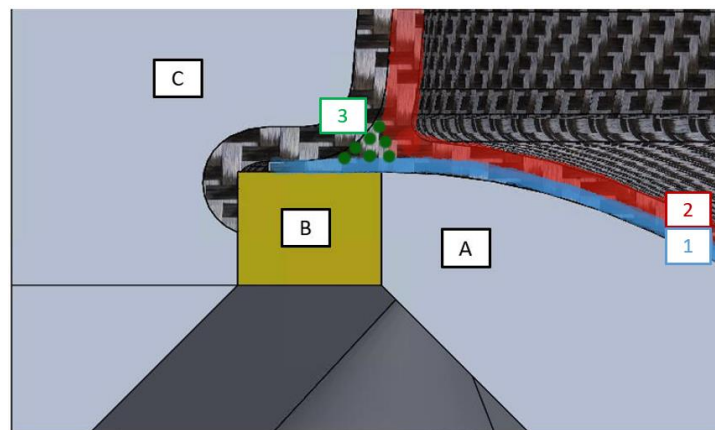


Figure 5.15: Detail of the molds assembly.

##### 5.2.2.1.1 Phase 1

The first step is to produce the rim using only the rim mold (C). All the plies have to be applied following the shape of this mold, layer by layer, as it is shown in the rim plybook, until getting its final shape.

#### 5.2.2.1.2 Phase 2

When the rim piece is produced, the next step is to apply the first three layers of the lens plybook (1 Twill T300 0° - 3 UD M40J - 1 Twill 300 144°) directly on the lens mold (A&B). These layers allow a better load transmission directly from the rim to the lens.

In figure 5.16, it is represented the total surface where these 3 layers are applied.

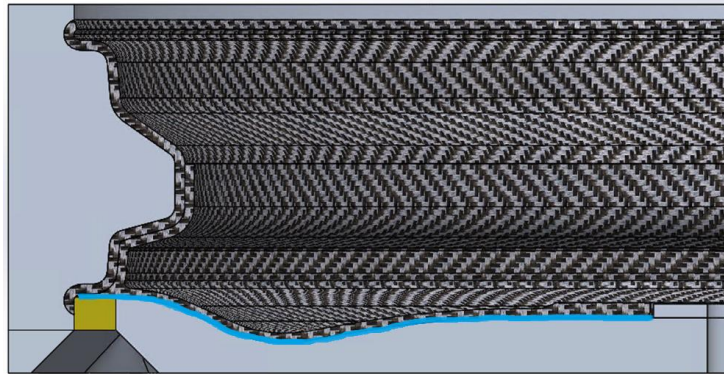


Figure 5.16: Total surface where the plies are applied during the phase 2 (Lens1).

A relevant detail to consider is that, the overall thickness of these three layers combined is 1.09 mm. This distance is important during the design process of the molds to obtain a good fit between the different parts that compose the final mold assembly.

#### 5.2.2.1.3 Phase 3

After that, the rim mold with the rim piece already produced, is placed on top of the lens mold as it is shown in the figure above. Once this has been done, it is necessary to fill the gap (3) between the rim and the Lens1 plies using unidirectional fibers with a high resin percentage, following the circumferential shape of the rim.

#### 5.2.2.1.4 Phase 4

The final step is to apply the rest of the plies following the red path shown in the scheme (2) until completing the total lens shape. The total surface that these plies cover is shown in figure 5.17:

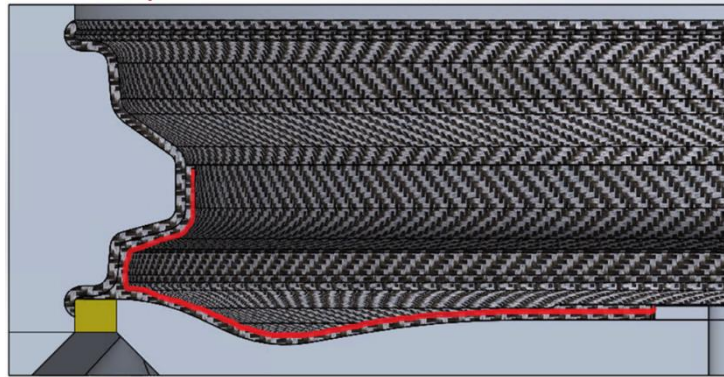


Figure 5.17: Total surface where the plies are applied during the phase 4 (Lens2).

### 5.2.3.- Design of the molds

In this section is explained how the mold is done to produce the rim and the lens pieces. This mold is composed by different parts which are explained as follows:

#### 5.2.3.1.- Rim mold

To obtain the rim piece, a mold has been performed dividing it, in three different parts. One of these parts, as it can be seen in figure 5.18 contains a hole where the valve of the wheel is located:

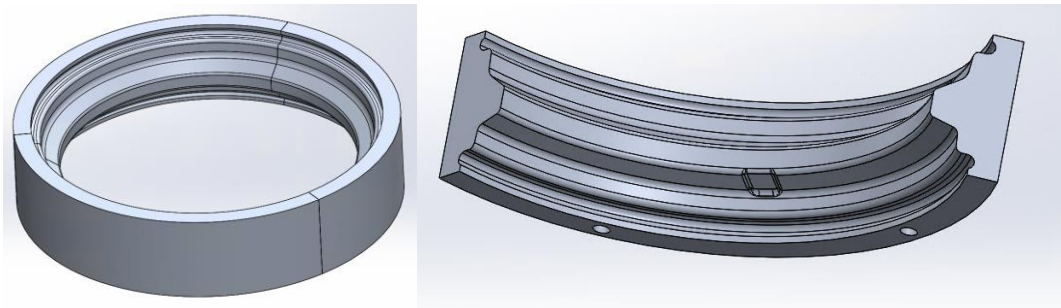


Figure 5.18: Molds to produce the rim.

Moreover, as it can be seen in figure 5.10, this hole has been made in such a way that none of the fibers are damaged in delicate areas of the rim shape. Finally, some holes have been performed following a circular pattern on the bottom face of the molds. These holes are used to connect, as it is explained before, this mold with the lens mold, using pins.

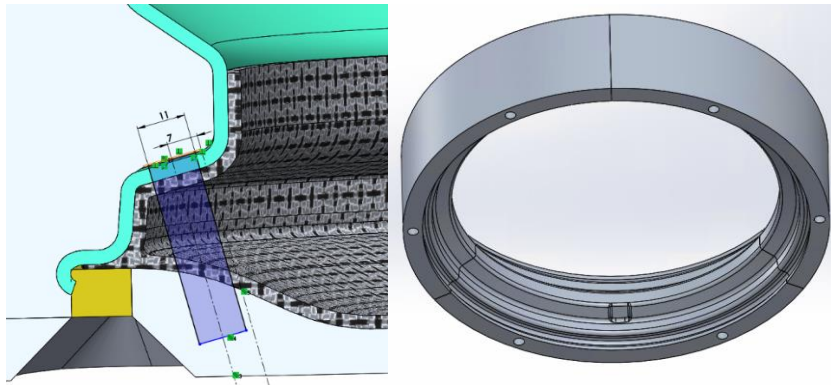


Figure 5.19: Detail of the valve hole location and the bottom face of the rim mold.

### 5.2.3.2.- Lens mold

In this case, the mold is divided in two different parts as it is represented in figure 5.20.

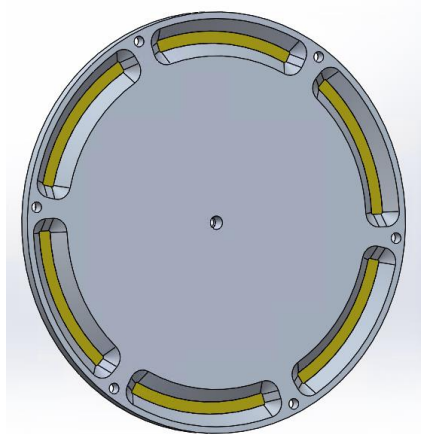


Figure 5.20: Lens mold.

The yellow silicone ring is used to push the lens fibers against the rim and in this way, to make a perfect connection between the two pieces. To do this, some holes have been done in the bottom part of the mold to allow the person who makes these components, to press the yellow ring against the rim mold without any problem.

On the other hand, the grey part of the mold represents the external shape of the lens, and besides that, it is used to fix the entire wheel mold as it has been explained before.

In figure 5.21, these mold parts can be observed in detail:

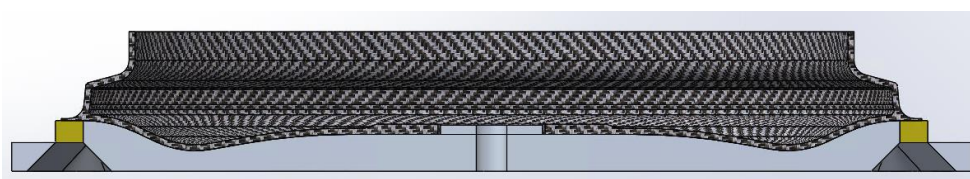


Figure 5.21: Cross-section detail of the lens mold including the final shape of the lens.

### 5.2.4.- Rotating bending test (modified from TÜV E/ECE324) simulation (v1.0)

As it is mentioned before, the lamination process for both components must be validated before starting the manufacturing process. All the steps followed to build the FEM model to determine if the previous plybooks are suitable for its application have been explained.

The project schematic to perform this FEM model is represented in figure 5.22:

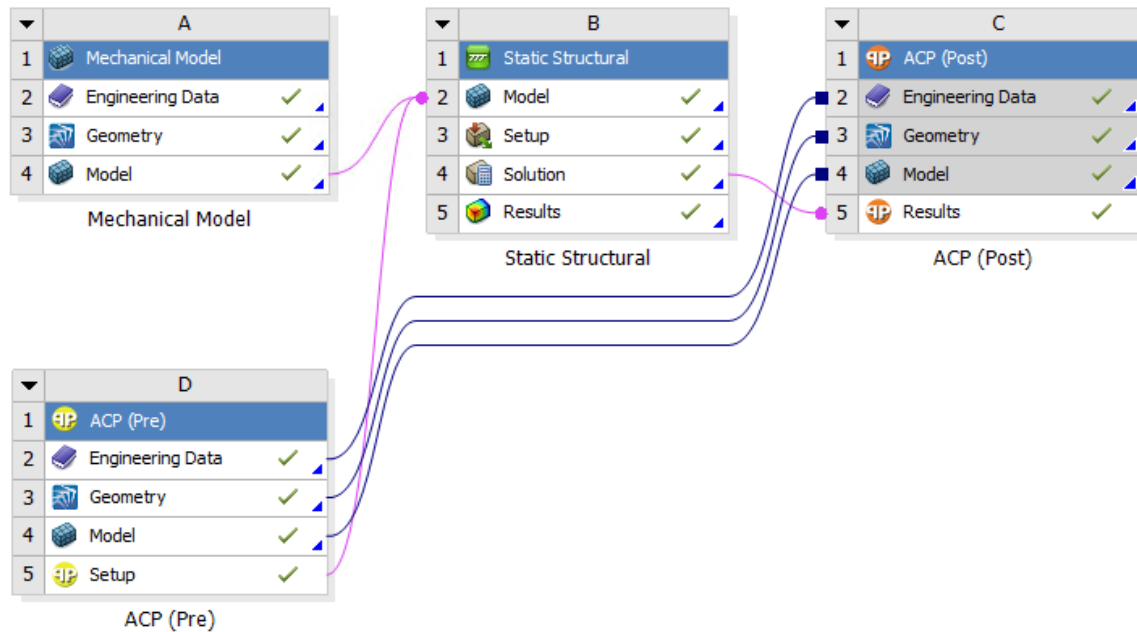


Figure 5.22: Project schematic.

This project is divided in four different modules:

- Mechanical model: Within this section, flange and bushes are included as solid components. The corresponding materials of these components have been mentioned in the wheel housing design.
- ACP (Pre): This module is used to create a solid component using composites materials. In this case, it has been used to create a single solid body containing the rim and lens.
- Static structural: In this module, all the solids from the mechanical model and the ACP (Pre) are included to perform the results of the simulation.
- ACP (Post): This section is useful to know the results in a particular zone of the model. It is useful, for example, to study the performance of one single ply inside the model.

Only the modules of ACP (Pre) and Static Structural are explained below since they are the most important parts for the development and analysis of the model.

### 5.2.4.1.- ACP (Pre)

#### 5.2.4.1.1 Geometry

Inside the geometry cell in SpaceClaim, the three surfaces needed to create the solid are included (figure 5.23). One of them represents the shape of the rim, and the other two are used to recreate the lens shape. The shape of these surfaces has been described before in the figure 5.16 and figure 5.17, on the detailed lamination of the lens section.

After that, it is necessary to combine these three surfaces to get a single surface. In this way, the program during the lamination process which will be explained later, is able to consider all these surfaces as an entire body. The tool used to do this is the share topology, which identifies topology parameters that can be shared among bodies in the model.

In this geometry, the shared elements are the faces and edges that these three surfaces have in common. Thus, the program directly recognises that, these elements are part of a single body and they are not superimposed on top of each other.

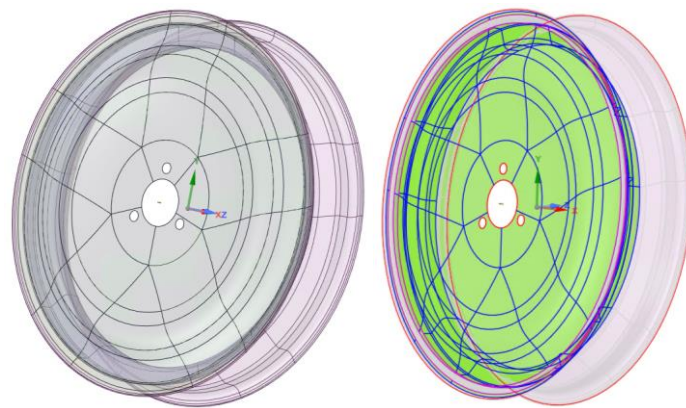


Figure 5.23: Surfaces used inside ACP (Pre) and shared elements using the shared topology tool.

#### 5.2.4.1.2 Model

Inside this section is important to define the mesh of the model but also to determine the proper named selections that will be used inside the setup section. It is necessary to define all the geometrical elements needed to apply all the plies in the right location and orientation.

These different named selections are shown in figure 5.24:

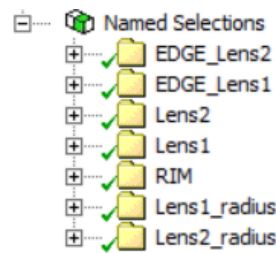


Figure 5.24: All named selections defined for the model.

- EDGE\_Lens2: All edges that will serve to orient all the M40J UD fibers in the different directions of the Lens2 radius (figure 5.25). Lens2 refers to the surface of the lens that is in contact with the innermost part of the rim. This surface has been represented before in figure 5.17.
- EDGE\_Lens1: All the edges that will serve to orient all the M40J UD fibers in the different directions of the Lens1 radius (figure 5.25).

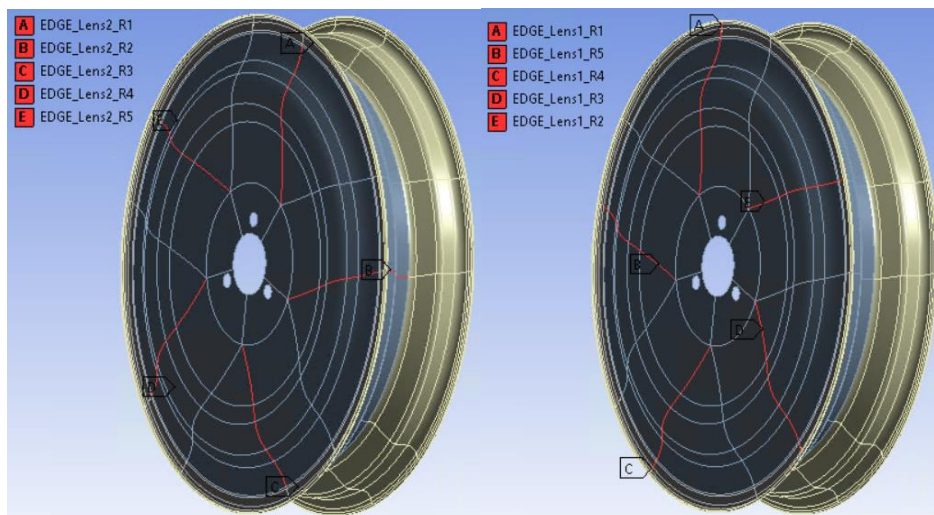


Figure 5.25: EDGE\_Lens2 and EDGE\_Lens1 named selections.

- Lens2: is used to apply the T300 Twill plies on the Lens2 surface (figure 5.26).
- Lens1: is used to apply the T300 Twill plies on the Lens1 surface (figure 5.26).

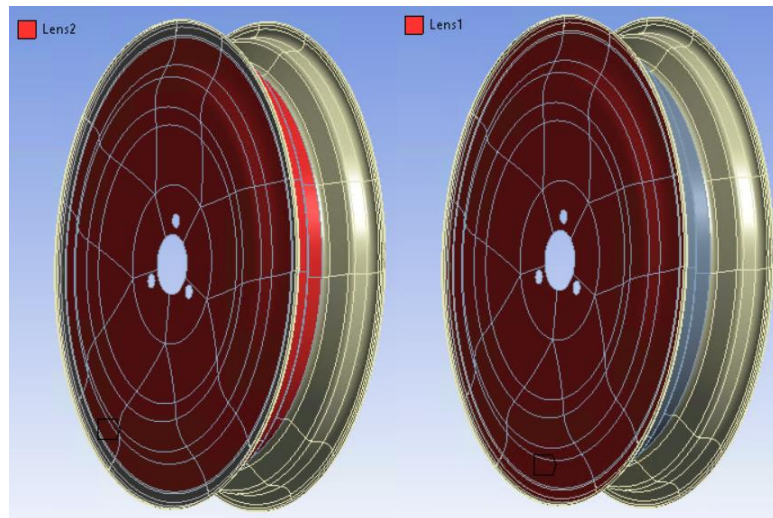


Figure 5.26: Lens2 and Lens1 surfaces.

- RIM: All the surfaces that represent the rim shape and the rim edge which will be used as reference to orientate all the rim plies (figure 5.27).

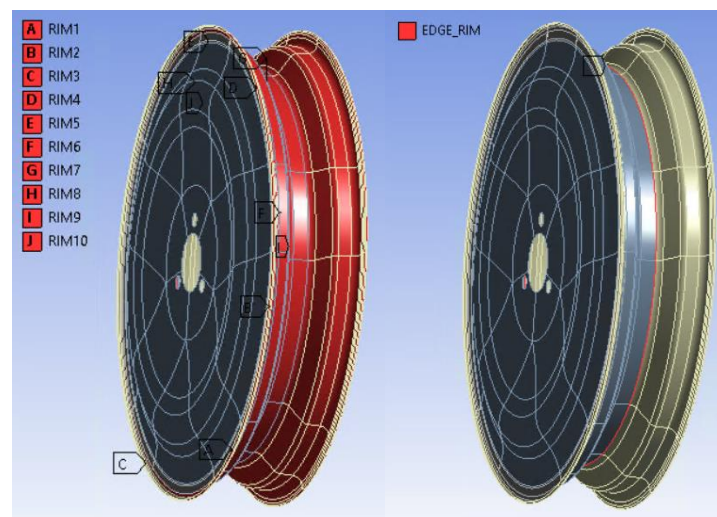


Figure 5.27: Named selections used for the rim.

- Lens1\_radius: this folder contains all the radius surfaces that belong to the Lens1 surface. These regions will be useful to put the UD M40J plies on the Lens1 surface (figure 5.28).
- Lens2\_radius: contains all the radius surfaces that belong to the Lens2 surface. These regions will be useful to apply the UD M40J plies on the Lens2 surface (figure 5.28).

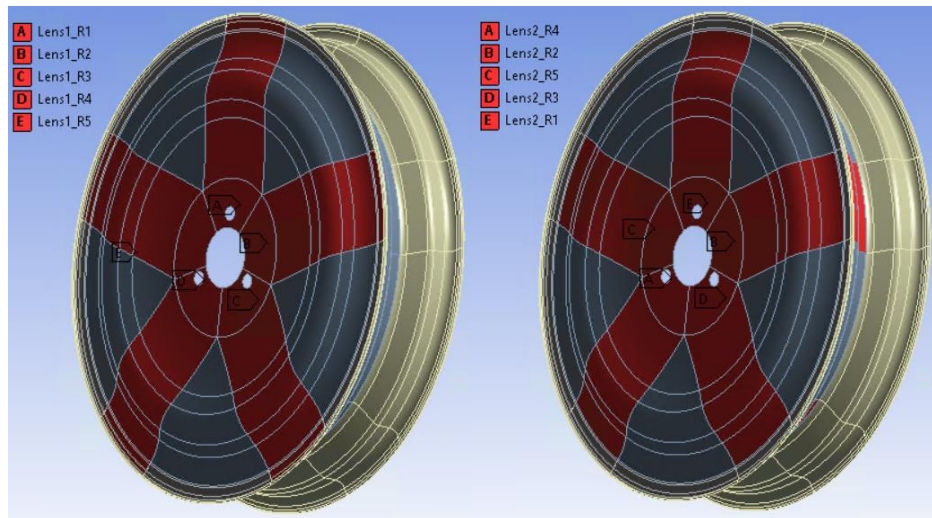


Figure 5.28: Lens1\_radius and Lens2\_radius named selections.

#### 5.2.4.1.3 Setup

This module allows to define the composite fabrics, the element orientation, the ply sequence, etc. Below, it is explained step by step the implementation of the composite solid model that has been imported later into static structural.

- Material data: in this section, all the materials have to be defined. In figure 5.29 all the material parameters used in this model are shown.
- Element sets: this section includes all the surface named selections that have been defined previously (figure 5.29).
- Edge sets: this section includes all the edge named selections that have been defined (figure 5.29).
- Rosettes: they are coordinate systems that used to set the reference direction of oriented selection sets. These coordinate systems define the 0° direction for the composite lay-up. There are different types of rosettes depending on the orientation that fibers must have [61].

In this particular case, all the rosettes applied are edge wise (figure 5.29). This means that the reference direction is given by a projection of the Rosette's X direction and the path of the Edge Set. In this way it is easier for the program to follow the circumferential shape of the rim or the orientation of each lens radius.

The RIM\_rosette (figure 5.30) is oriented in such a way that the plies in the 0° direction follow the direction of the EDGE\_RIM. On the other hand, the Lens1 and Lens2 rosettes are oriented matching the 0° direction with the orientation of its

correspondent radius edge. In figure 5.31, as an example, it is represented the position of the Lens1\_R1\_rosette.

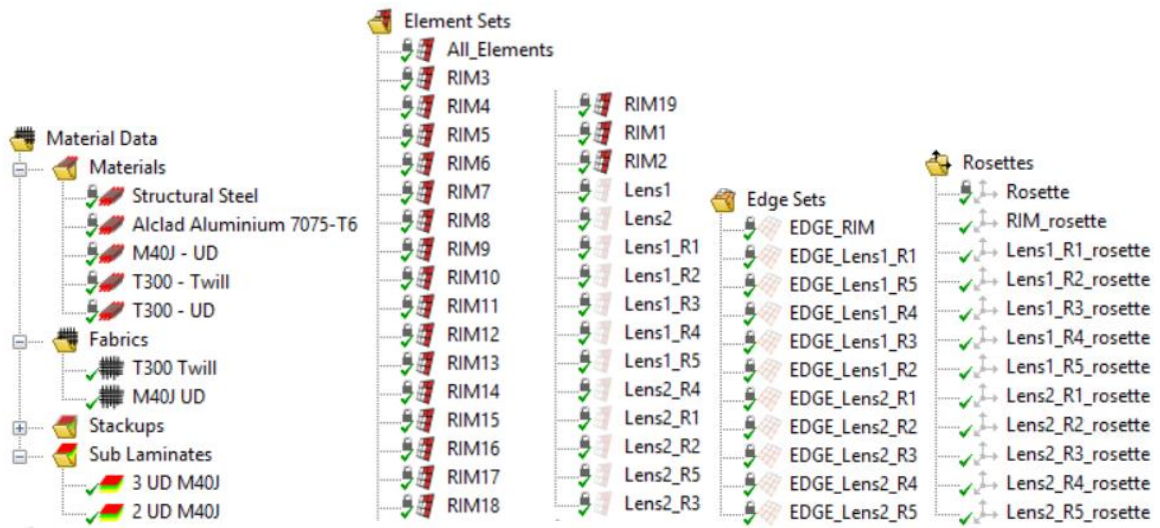


Figure 5.29: Material Data, Element Sets, Edge Sets and Rosettes in Setup.

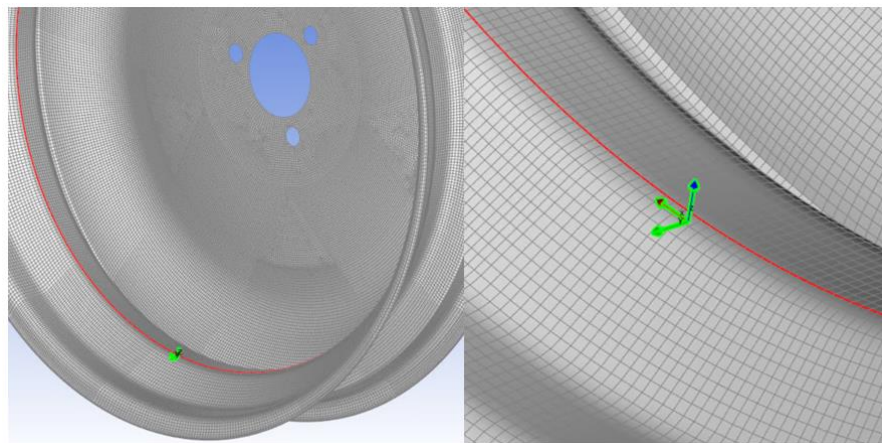


Figure 5.30: RIM\_rosette.

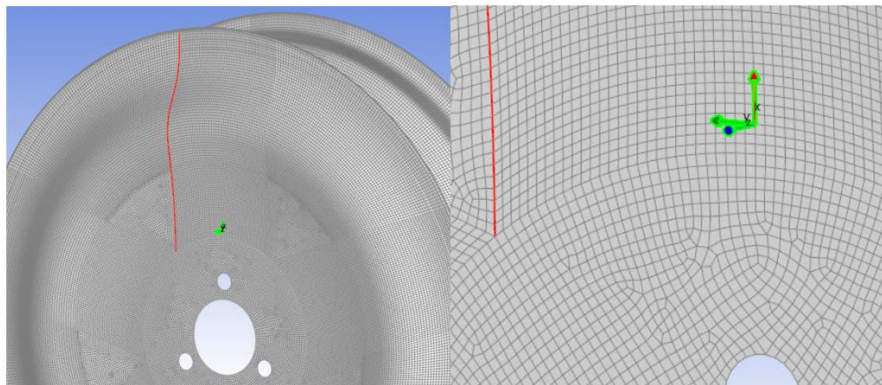


Figure 5.31: Lens1\_R1 rosette.

- Oriented selection sets: in this section, the element orientation of the Element Set is decided. Moreover, it is necessary to determine the stacking direction of the associated lay-up. In this model, not all the stacking directions follow the same orientation (figure 5.32) [62].

All the plies that belong to Lens1 have an opposite stacking direction because the imported Lens1 surface in the geometry represents the last of its plies in the lamination process. The case of the rim is similar because the surface that is considered as the starting surface in the model, in reality, is the last ply that is applied in the lamination process. However, the stacking direction of the Lens2 follows the order of the plies in the lay-up process.

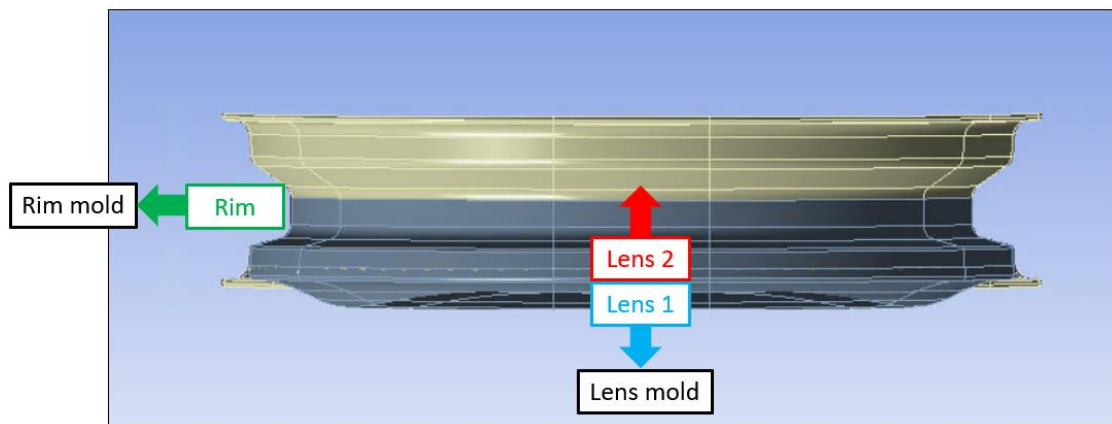


Figure 5.32: Stacking directions of each Element Set group.

- Modeling groups: the desired composite lay-up can be defined. Beforehand, it is necessary to specify at least an Oriented Element Set and a material. In addition, the ply angle referred to the corresponding rosette system needs to be determined [63]. In this case, as it is mentioned before, the order of the plies in the Lens1 and RIM have to be inverted (figure 5.33).
- Solid Model: this section is used to create the solid model which will be exported to static structural later. The general tab to build this solid has the following properties (figure 5.33):

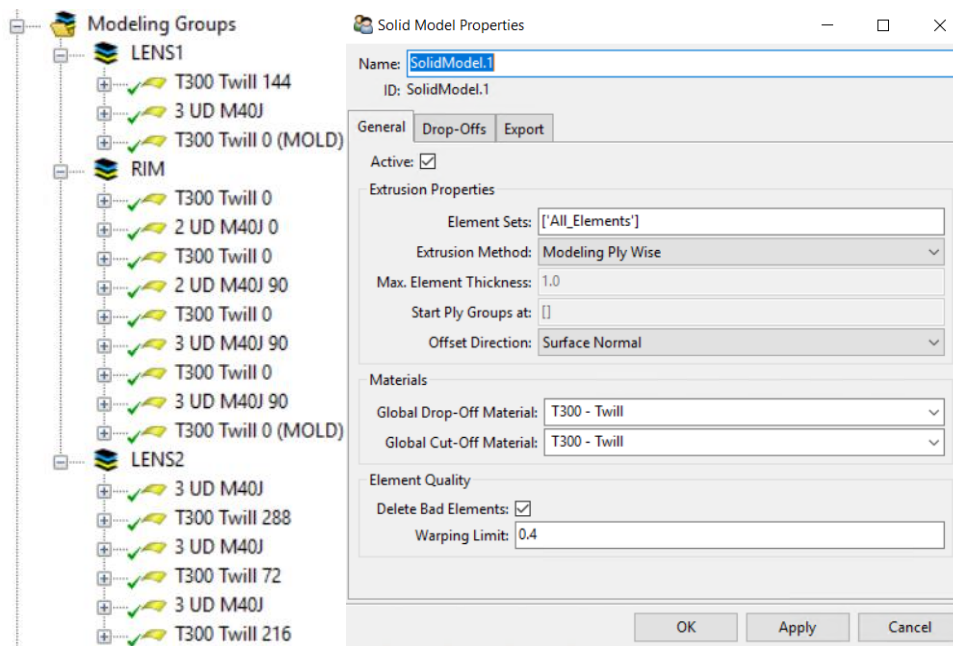


Figure 5.33: Modeling groups and solid model properties.

The extrusion method used is modeling ply wise. This method extrudes each Modeling Ply as one solid element layer. The offset direction to put all the plies is surface normal. With this option, the extrusion direction is reevaluated after each row of solid elements.

In the drop-off option, it has been selected the outside ply drop-off, which creates an union element between layers that are not joined (figure 5.34). The material used to join the layers is the T300 Twill.

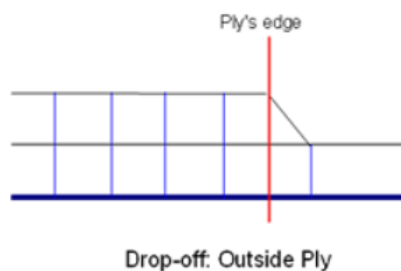


Figure 5.34: Outside ply drop-off [64].

Finally, after updating the model, ACP (Pre) generates the solid body that will be study in static structural (figure 5.35).

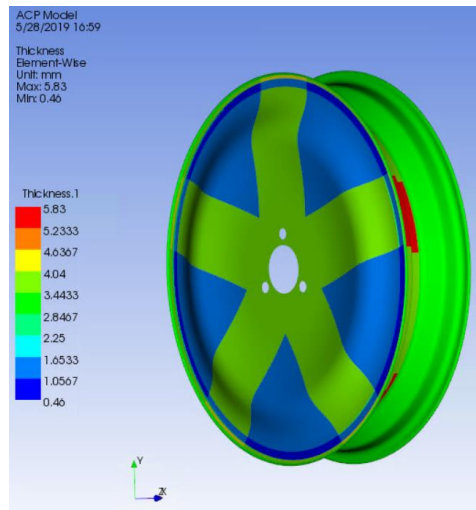


Figure 5.35: Solid model created in ACP (Pre).

### 5.2.4.2.- Static structural

#### 5.2.4.2.1 Materials

For this model, as it has been done before in previous simulations, the bushes material is structural steel and for the flange, Alclad Aluminium 7075-T6 has been used. This material assignment has been done previously in the mechanical model. In the case of the lens and rim, the program gets all the information obtained from ACP (Pre).

#### 5.2.4.2.2 Loads & constraints

A similar test like the one carried out at the bending stiffness simulation (bending TÜV test), has been performed. Thus, the rim has been fixed on the vertical surface farthest from the lens and, a bending moment has been applied on the axis perpendicular to the axis of revolution of the wheel (figure 5.36). In this case, the magnitude of this moment has a value of 730 Nm and has been applied on the front face of the flange (+Z direction).

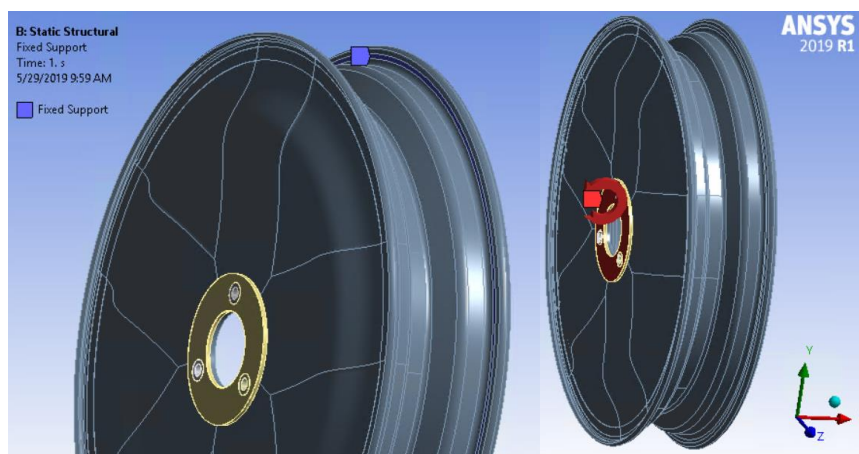


Figure 5.36: Loads and constraints in the simulation.

### 5.2.4.2.3 Results

To validate the plybooks of the rim and lens, it has been used the composite failure tool evaluating the inverse reserve factor. The theories used to perform the inverse reserve factor are the Tsai-Wu, Tsai-Hill, and Hashin failure criteria. In this way, the program evaluates all these criteria and shows the results of the most critical failure mode on each element.

This analysis has been done using the 3D value for all the configurations inside the composite failure tool. Using the 3D configuration allows the program to consider the shear stresses between the different plies in contact and therefore, to obtain a more realistic model.

Once the simulation is done, the results show that in several regions of the lens geometry, the inverse reserve factor is over one (figure 5.37). This means that, in many plies of the model would have problems under these load conditions. In some cases, the most critical failure criteria for these regions are the Tsai-Wu and Tsai-Hill criteria which normally are a bit conservative than what happens in reality. Despite this, it is necessary to change the lens plybook to get better results.

On the other hand, as it can be seen in the results, the maximum reverse factor of the rim is under one which means that this rim has a good performance under these conditions (figure 5.37).

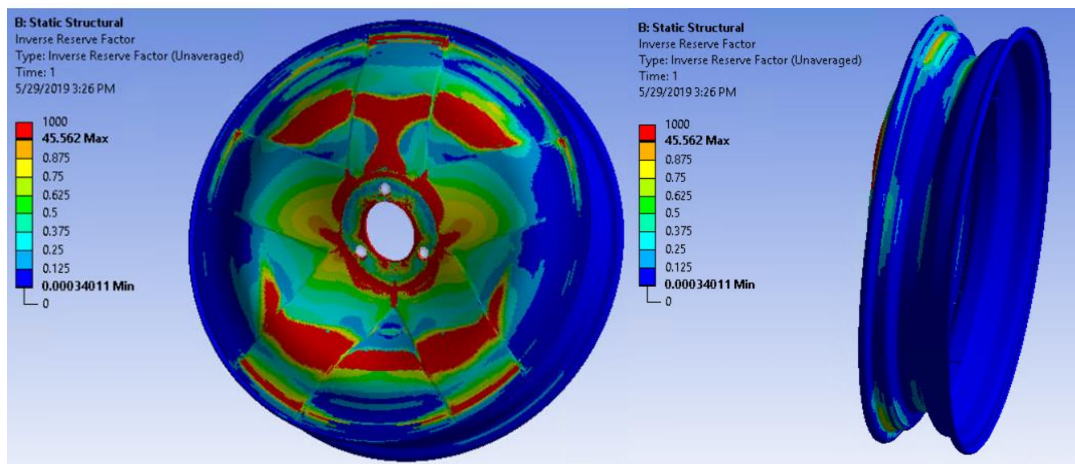


Figure 5.37: Inverse reserve factor results.

Observing the results more in detail, it is possible to appreciate some important aspects that need to be changed in the next model:

- The maximum value of the lens inverse reserve factor is 45.56. This value is not real due to a failure of the model. As it is mentioned before, on the detailed lamination process of the lens (figure 5.15), during the manufacturing process, the gap with the triangular shape in the model, needs to be filled with unidirectional fibers. However, in ACP (Pre), it is impossible to cover that part correctly and, for this reason, in the model there is a gap in that region (figure 5.38).

A possible solution to enhance for the following simulation is to cover that gap with a solid body (using the T800 Twill homogeneous material). This body must have similar characteristics to those of the unidirectional fibers that will be used for the lamination. In this way, it is possible to make a model that is more suited to reality.

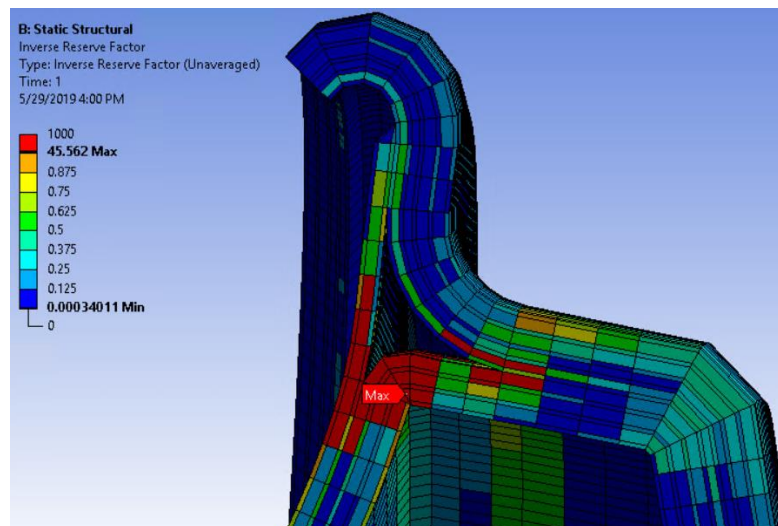


Figure 5.38: Gap between the lens and rim shapes.

- In addition, there is an overlap of fiber elements in an area close to that gap (figure 5.39). This overlap is produced due to the application of a great number of fibers using a small radius to represent that curve of the Lens2 surface.

One possible solution to avoid this problem for the next simulation is to increase that radius. In this way, the program will generate the composite solid without any interference problem.

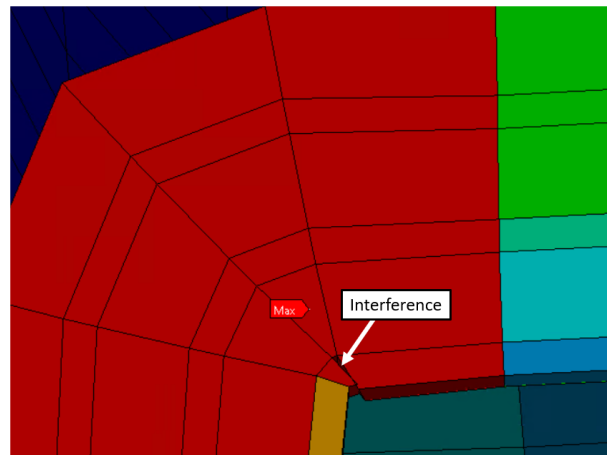


Figure 5.39: Overlap between fibers.

**5.2.5.- Rotating bending test (modified from TÜV E/ECE324) simulation (v1.1)**

As it has been described before, the results of the previous simulation showed that it was necessary to perform a new lens plybook (table 5.4) and change some characteristics of the model. This simulation has been carried out maintaining the same boundary conditions as the previous simulation. The only differences are that for this new simulation, the lens plybook has been changed and the model problems previously mentioned have been solved.

Ply type	N° of plies	Orientation	Zone
Twill T300	1	0° (R1)	All the external part of the lens (Lens1)
Twill T300	1	45° (R1 + 45°)	Central disk (diameter=240mm)
UD M40J	4 (x5 radius)	radial	Radius of the lens
Twill T300	1	144° (R3)	All the external part of the lens (Lens1)

Ply type	N° of plies	Orientation	Zone
UD M40J	-	circumferential	To fill the gap between lens and rim
Biax T300	patches	radial	Contact curve between lens and rim
Twill T300	1	189° (R3 + 45°)	Central disk (diameter=240)
UD M40J	4 (x5 radius)	radial	Radius of the lens
Twill T300	1	288° (R5)	All the internal part of the lens (Lens2)
Twill T300	1	333° (R5 + 45°)	Central disk (diameter=240)
UD M40J	4 (x5 radius)	radial	Radius of the lens
Twill T300	1	117° (R2 + 45°)	Central disk (diameter=240)
Twill T300	1	72° (R2)	All the internal part of the lens (Lens2)
UD M40J	5 (x5 radius)	radial	Radius of the lens
Twill T300	1	261° (R4 + 45°)	Central disk (diameter=240)
Twill T300	1	216° (R4)	All the internal part of the lens (Lens2)

Table 5.4: Lens plybook v1.1.

To do this new lens, some improvements have been made with respect to its previous version:

- Some disks of Twill T300 have been included to reinforce the central region of the lens. All of them have been orientated  $+45^\circ$  with respect to its preceding Twill ply. In this way, in the central region, all directions are covered with fibers, which means that, this lens will withstand better against stresses caused by torsion, bending, etc.
- The number of UD M40J has been increased in such a way that these UD blocks did not reach more than 1 mm thick (4 UD M40J). This has been done to avoid leaps of thicknesses which can become zones of stress concentration.
- A reinforcement zone has been added between the lens and rim to try to reinforce the curvature that connects these two parts (figure 5.40). These patches have been one using Biaxial T300 (two plies of UD T300 [65] in a  $+45^\circ/-45^\circ$  disposition).

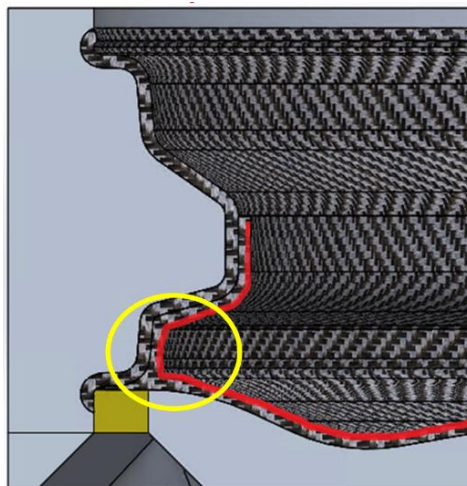


Figure 5.40: Region where the patches of Biaxial T300 are applied.

- As it can be in figure 5.41, the Lens2 has been reduced covering a smaller contact surface between lens and rim. In this way, it is possible to reduce the final weight of the wheel besides facilitating the lamination process to the person who produces these components.

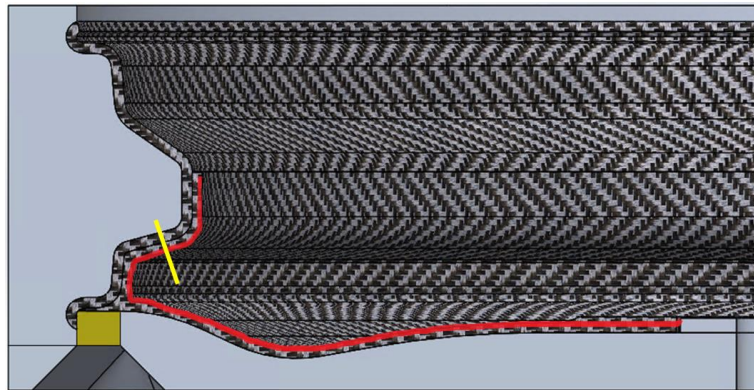


Figure 5.41: New Lens2 surface.

### 5.2.5.1.- Results

The results evaluated in this simulation have been the total deformation of the lens and its inverse reverse factor using the 3D Hashin criterion (figure 5.42). Only this criterion has been used since the experience of the previous wheel project had shown that this is the one which represents better the real behaviour of these components.

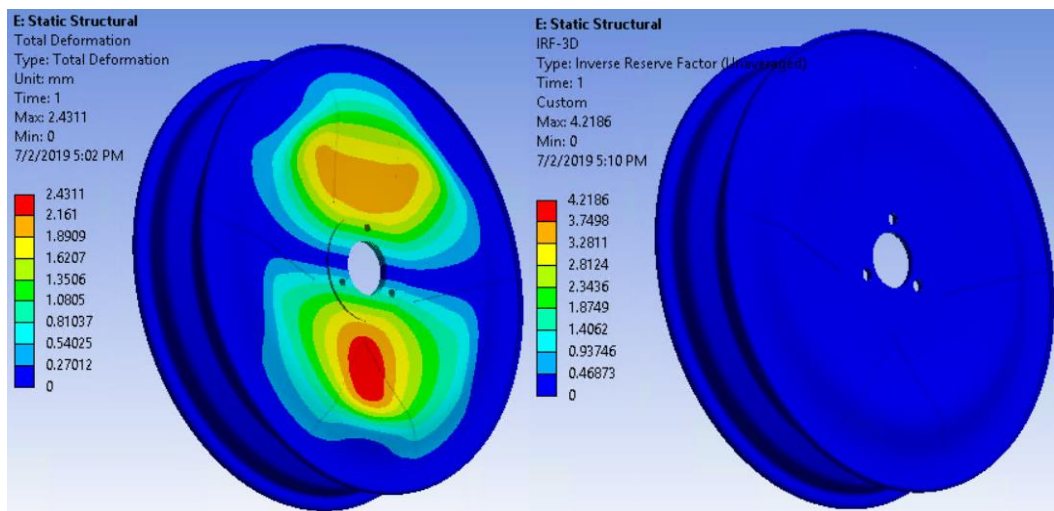


Figure 5.42: Total deformation and inverse reverse factor results.

In this case, the values of the inverse reverse factor have been decreased considerably. Moreover, as it can be seen in figure 5.43, the maximum and highest values correspond to specific areas where the mesh is not able to generate itself correctly or on the curvature located in the gap between the lens and rim. In fact, the results in that curvature don't represent the real performance of this solid since the real wheel will have this gap covered with unidirectional fibers. In the rest of the plies, the inverse reverse factor have acceptable values (figure 5.44).

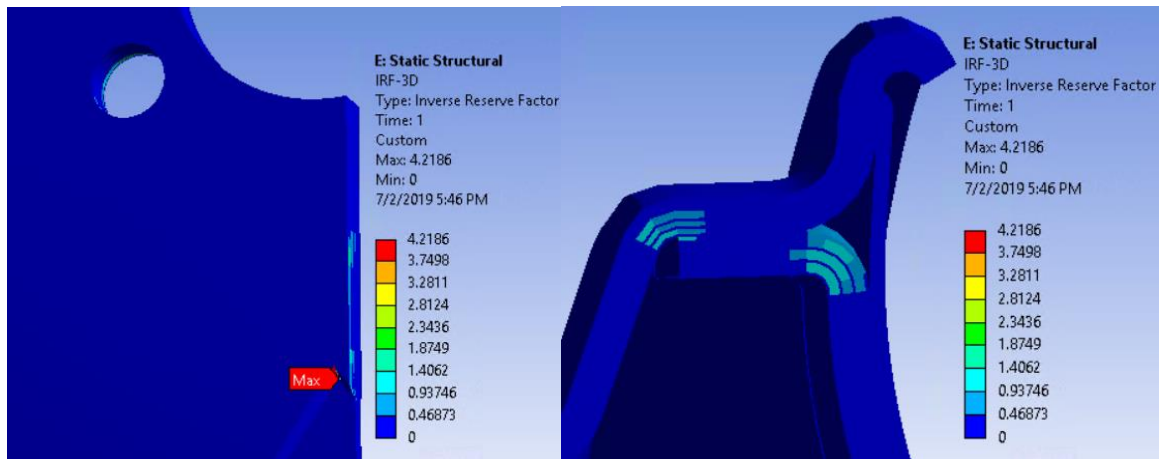


Figure 5.43: Regions where the highest inverse reverse factor values are located.

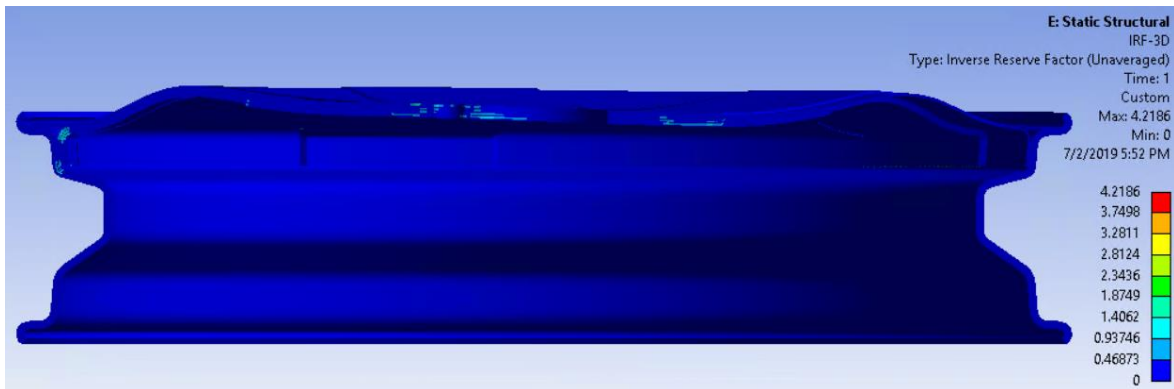


Figure 5.44: Lens inverse reverse factor results.

### 5.2.6.- Rotating bending test (modified from TÜV E/ECE324) simulation (v2.0)

After a meeting with the producer, where the details of the two lamination sequences have been commented (lens and rim plybooks), some changes have been decided.

The first one is to use a T1000 unidirectional [66] instead of M40J UD. This has been due to a shortage of M40J material in stock that would not be enough to produce all the wheels. The other change which has been done is to try to make a rim lamination more optimized in terms of thickness trying to reinforce the most critical zones. Considering these changes, new lamination sequences have been performed (table 5.5 and table 5.6):

Lamination sequence	n° plies	ply orientation	Zone 1	Zone 2	Zone 3	Zone 4	Zone 5
			ply type				
↑	2	0°	Twill T300				
	2	0°	UD T1000				
	2	0°					Twill T300
	1	0°					Twill T300
	2	0°					Twill T300
	4	90°					UD T1000
	2	90°					UD T1000
	1	45°					Twill T300
	3	90°					UD T1000
	3	90°					UD T1000
1	0°	Twill T300					
Mold surface							
Thickness (mm)			1.03	1.38	2.12	3.43	4.11

Table 5.5: Rim plybook v2.0.

As it has been mentioned before, the lamination sequence of the rim has undergone a big change with respect to its first version (v1.0). The intention of this new lamination is to try to scale as much as possible the UD T1000 plies. In this way, it is possible to place a greater number of these plies together avoiding areas where there are large differences in thickness, that can act as stress concentration zones. In addition, a greater number of Twill T300 plies have been added in order to increase the strength of this component against the pressures acting on the tire.

Ply type	N° of plies	Orientation	Zone
Twill T300	1	0° (R1)	All the external part of the lens (Lens1)
Twill T300	1	45° (R1 + 45°)	Central disk (diameter=240mm)
T1000	5 (x5 radius)	radial	Radius of the lens
Twill T300	1	144° (R3)	All the external part of the lens (Lens1)
Ply type	N° of plies	Orientation	Zone
UD T1000	-	circumferential	To fill the gap between lens and rim
Biax T300	patches	radial	Contact curve between lens and rim
Twill T300	1	189° (R3 + 45°)	Central disk (diameter=240)
UD T1000	4 (x5 radius)	radial	Radius of the lens
Twill T300	1	288° (R5)	All the internal part of the lens (Lens2)
Twill T300	1	333° (R5 + 45°)	Central disk (diameter=240)
UD T1000	4 (x5 radius)	radial	Radius of the lens
Twill T300	1	117° (R2 + 45°)	Central disk (diameter=240)
Twill T300	1	72° (R2)	All the internal part of the lens (Lens2)
UD T1000	5 (x5 radius)	radial	Radius of the lens
Twill T300	1	261° (R4 + 45°)	Central disk (diameter=240)
Twill T300	1	216° (R4)	All the internal part of the lens (Lens2)

Table 5.6: Lens plybook v2.0.

As it can be observed in the lens lamination, the changes made have been minimal compared with its second version (v1.1). Only the M40J material has been replaced by the T1000 adding more plies in the most external lens layers.

**5.2.6.1.- Results**

The total deformation and the inverse reverse factor (using the 3D Hashin criterion) results are shown below (figure 5.45 and figure 5.46). The lens and rim have obtained acceptable results since, as it can be observed in figure 5.46, the most critical areas remain the same as those of the previous simulation.

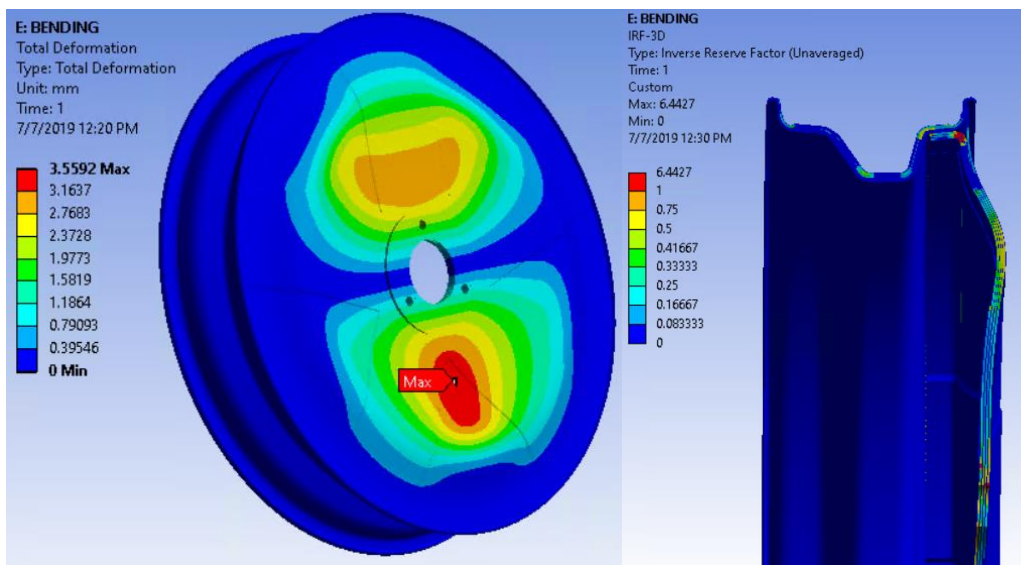


Figure 5.45: Total deformation and inverse reverse factor results.

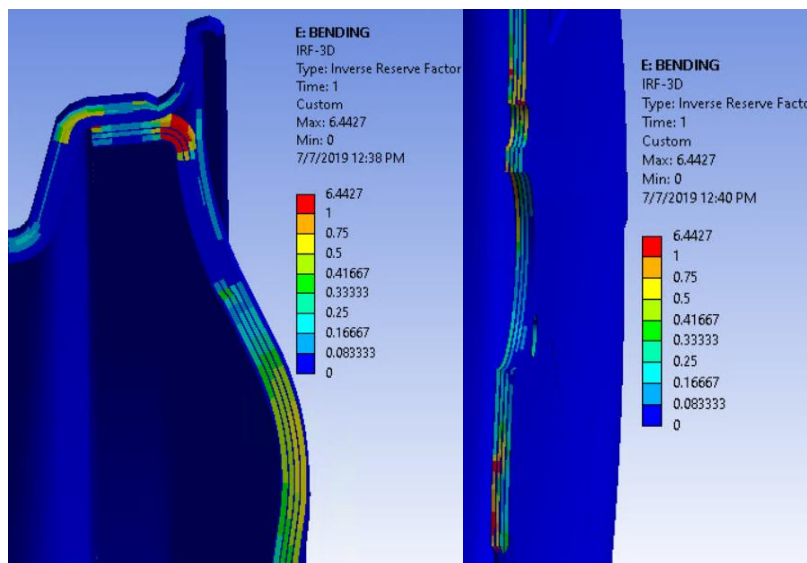


Figure 5.46: Regions where the highest inverse reverse factor values are located.

**5.2.7.- Rim inflation pressure simulation (v2.0)**

In this simulation, the influence of tire pressure acting on the rim has been analysed. As it has been explained earlier on the “Emilia 4 wheels” section, the pressure values for this simulation correspond to those acting on the rim at an inflation pressure of 8 bar. This value represents approximately the maximum pressure that the tire can reach when the wheel meets a bump or a hole in the road during the race.

**5.2.7.1.- Load & constraints**

To represent the 8 bar pressure, two different pressures have been considered.  $P_0$  represents the internal pressure inside the tire while  $P_f$  represents the pressure which acts in the contact area between the rim and the tire (figure 5.47). The relationship between these two magnitudes as well as the calculations necessary to obtain them have been mentioned previously (table 3.14).

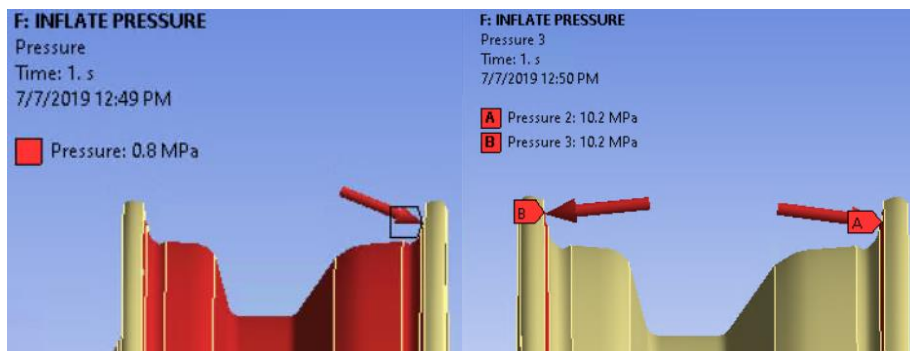


Figure 5.47:  $P_0$  and  $P_f$  pressures.

In addition to including these pressures, it has been decided to fix the central surface of the lens to have a performance of the model as faithful as possible to reality (figure 5.48).

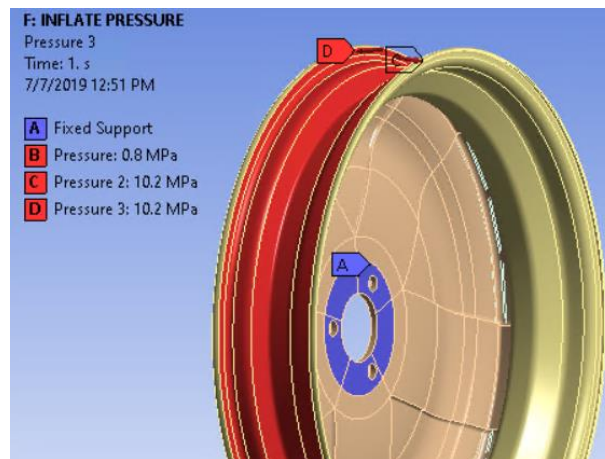


Figure 5.48: Loads and constraints included in the inflation pressure simulation.

### 5.2.7.2.- Results

As it can be observed, in figure 5.49 there are some plies that have inverse reserve factor (Hashin 3D) values greater than one. After observing in detail the failure reason in these plies, it has been discovered that the failure is due to the breakage of the matrix in certain plies of UD T1000. Among the possible reasons for the failure of a composite material, the matrix breakage is one of the least critical if the lamination sequence has been done based on the interruption of crack propagations generated from these microfractures. As mentioned before, a significant number of Twill plies have been included in the rim plybook to avoid this. In addition, it must be considered that this tensional state would only occur if the car reached a bump that can generate a pressure of 8 bar on the tire, which is unlikely. Considering all the above, it can be affirmed that the results of the rim are acceptable in this simulation.

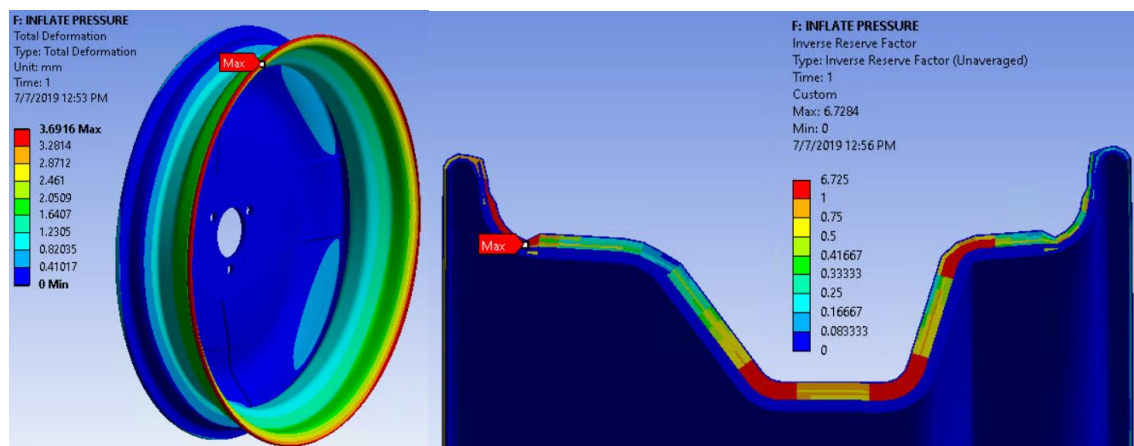


Figure 5.49: Total deformation and inverse reserve factor results in the inflation pressure simulation.

Considering the results obtained from the bending and inflation pressure simulations, it can be confirmed that the rim and lens plybooks v2.0 will be used to produce these components. To validate these plybooks, only these two simulations have been considered since these are the two most critical situations that these two components must endure.

Subsequently, the rest of simulations have been done to observe the performance of the wheel considering different load conditions (torsion, impact...).

### 5.2.8.- Torsion (rev CD – vehicle dynamics) simulation (v2.0)

In this simulation, the effect of the torsional moment transmitted through the pins in the wheel has been analysed.

### 5.2.8.1.- Loads & constraints

The torque moment (665 Nm) has been decomposed into three forces that act on the surface where the pins are located.

In addition, the external part of the rim has been fixed, also adding two displacement constraints to have a proper performance of the model (figure 5.50). In the restriction of the rim only the displacement in the axial direction is allowed while in the case of the central part of the lens, the axial direction is the only one in which there can be no displacement.

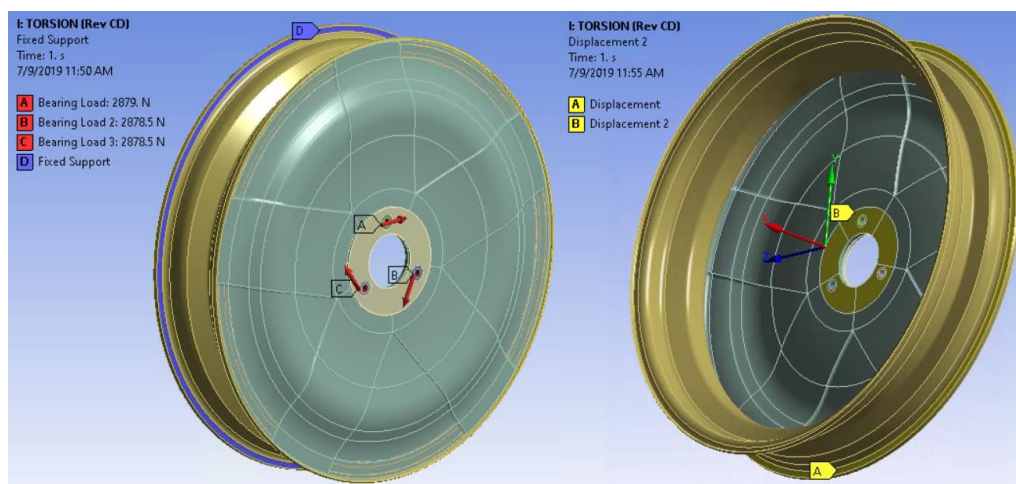


Figure 5.50: Loads and constraints in the torsion simulation.

### 5.2.8.2.- Results

The total deformation and the inverse reserve factor (Hashin-3D) have been evaluated (figure 5.51)

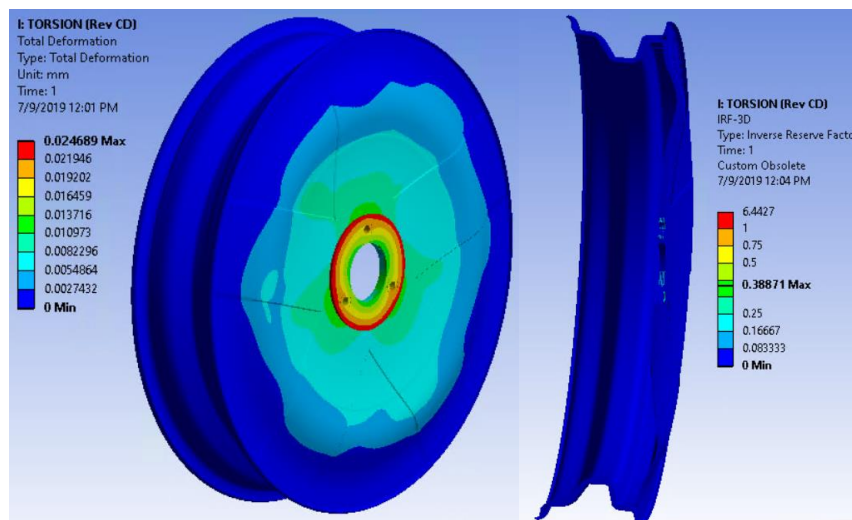


Figure 5.51: Torsion simulation results.

**5.2.9.- Impact (rev CD – vehicle dynamics) simulation (v2.0)**

In the case of the impact test, it has been assumed that the vehicle is subjected to an acceleration of 6g vertical (on both sides of the rim) and a 3g acceleration in the lateral direction (only on one side of the rim), both considering 1/3 of the rim. In addition, the presence of the internal inflation pressure has been included.

**5.2.9.1.- Loads & constraints**

In this simulation, the nominal inflation pressure of 5 bar have been considered.

Through a nodal named selection, it has been possible to apply the 6g and 3g accelerations directly on the 1/3 of the rim which represents the contact region between the rim and the tire when the wheel is in contact to the ground.

Moreover, a displacement and a cylindrical support have been included to constraint the displacement of the lens (figure 5.52). In the case of the central part of the lens, the axial direction is the only one in which there can be no displacement while in the bush surfaces (cylindrical support), the tangential direction is the only one in which there can be a displacement.

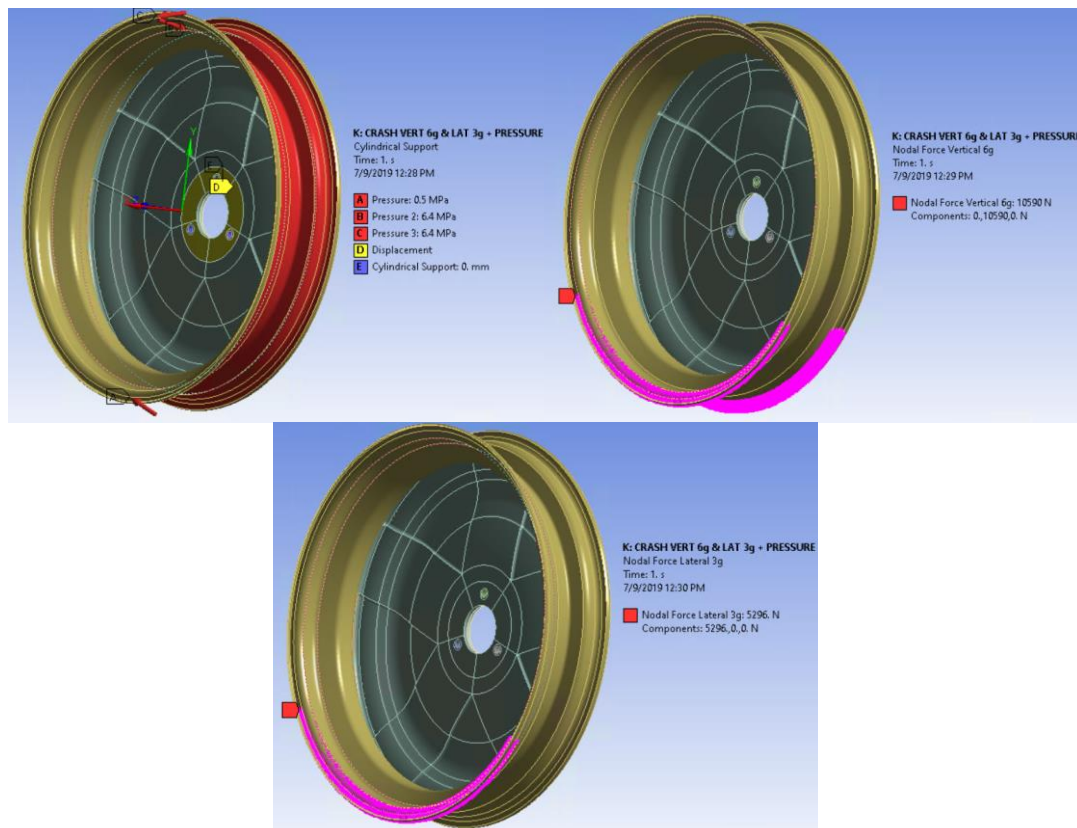


Figure 5.52: Loads and constraints in the impact simulation.

### 5.2.10.- Results

The total deformation and the inverse reserve factor (Hashin-3D) have been evaluated (figure 5.53).

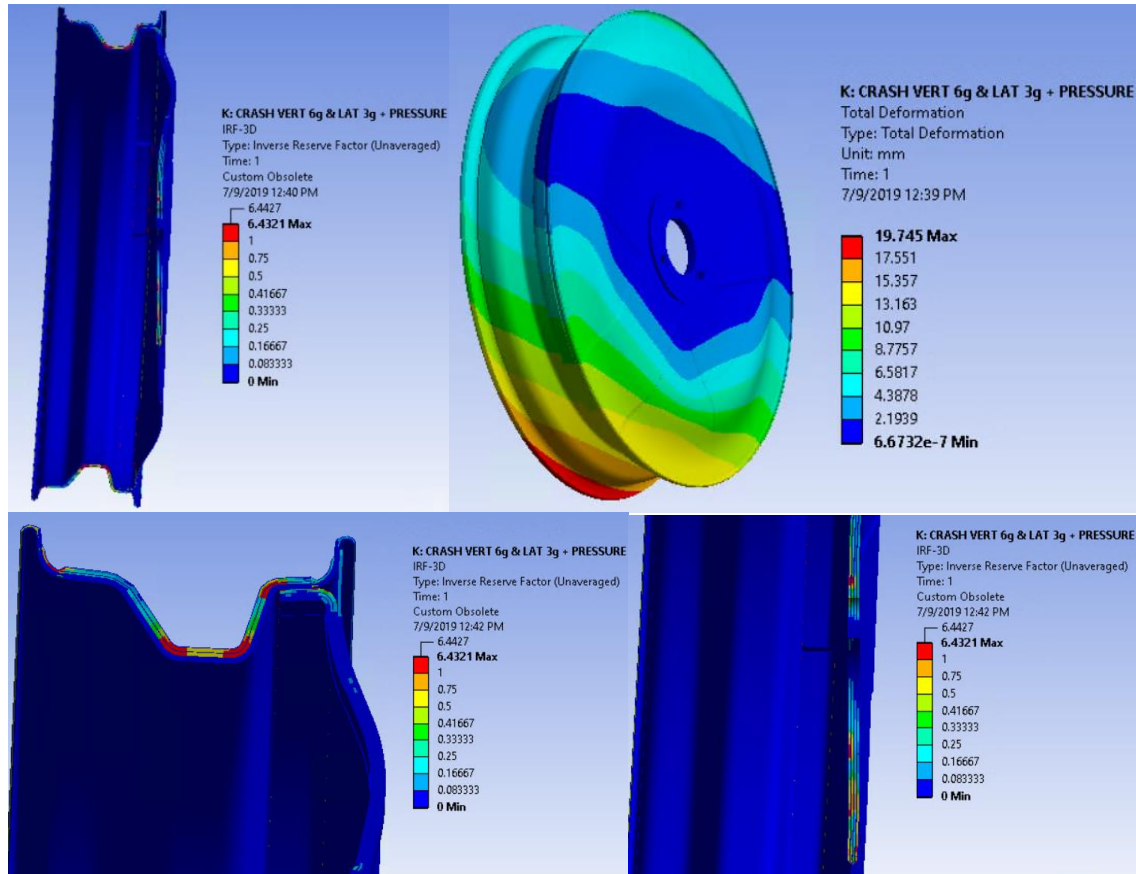


Figure 5.53: Impact test results.

### 5.2.11.- Rolling (modified from TÜV E/ECE 324) simulation (v2.0)

In this simulation it has been considered the effect on the wheel during rolling under a load condition, as it occurs on a road drive.

#### 5.2.11.1.- Load & constraints

A vertical load (6623 N) is applied in the central face of the lens, fixing one side of the rim and controlling the displacement on the other one as it has been done in the torsion simulation. Moreover, it has been included the effect of the inflation pressure at 8 bar (figure 5.54).

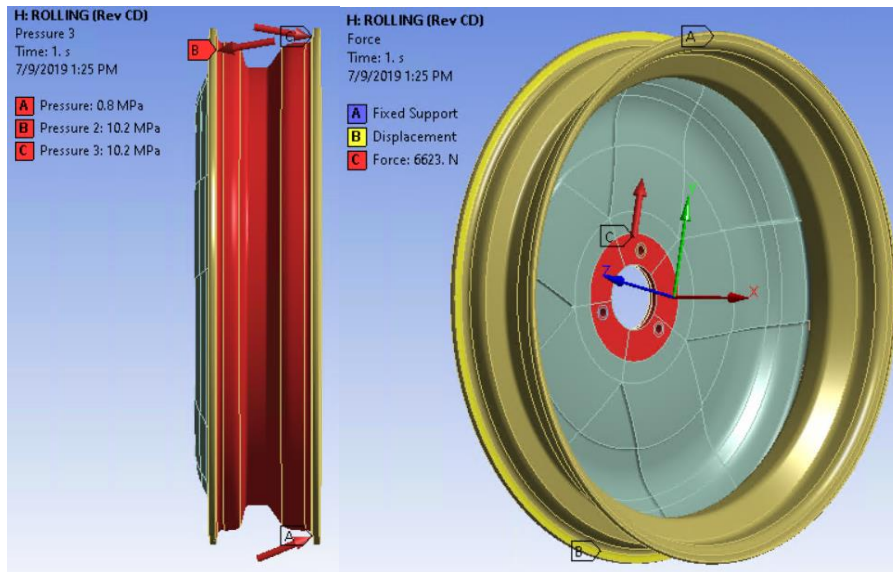


Figure 5.54: Loads and constraints in the rolling simulation.

### 5.2.11.2.- Results

The total deformation and the inverse reverse factor (Hashin-3D) have been evaluated (figure 5.55).

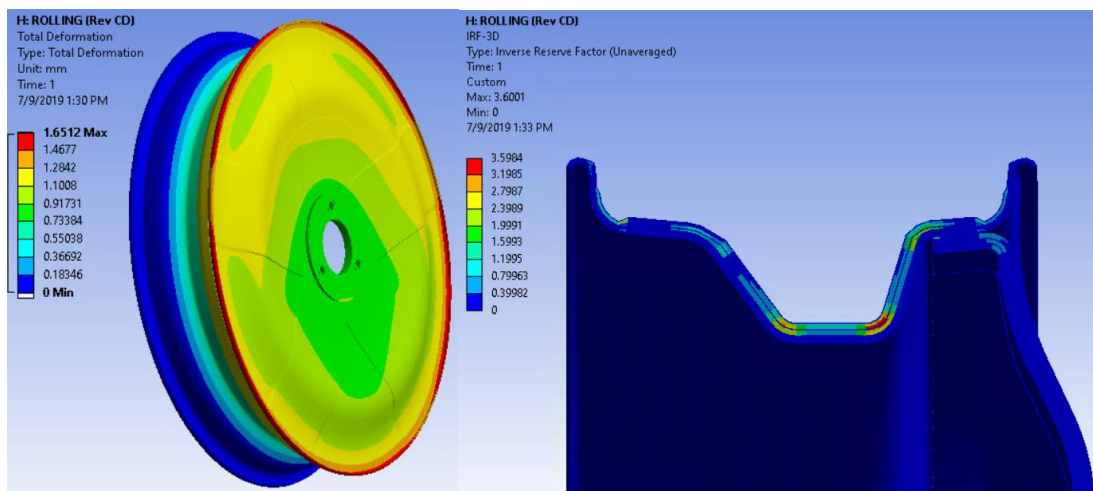


Figure 5.55: Rolling simulation results.

### 5.2.12.- Curve loads (rev CD – vehicle dynamics) simulation (v2.0)

Within this simulation, the load condition, when the vehicle is taking a curve, has been applied on the wheel.

#### 5.2.12.1.- Loads & constraints

To represent the load condition when the vehicle is taking a curve, a remote force including all the force components has been applied in the contact area between rim and

tire considering the external radius of the tire (figure 5.56). Moreover, the effect of the nominal inflation pressure (5 bar) has been included besides fixing displacements on the central region of the lens and the surfaces where pins are located (as it has been done in the impact simulation).

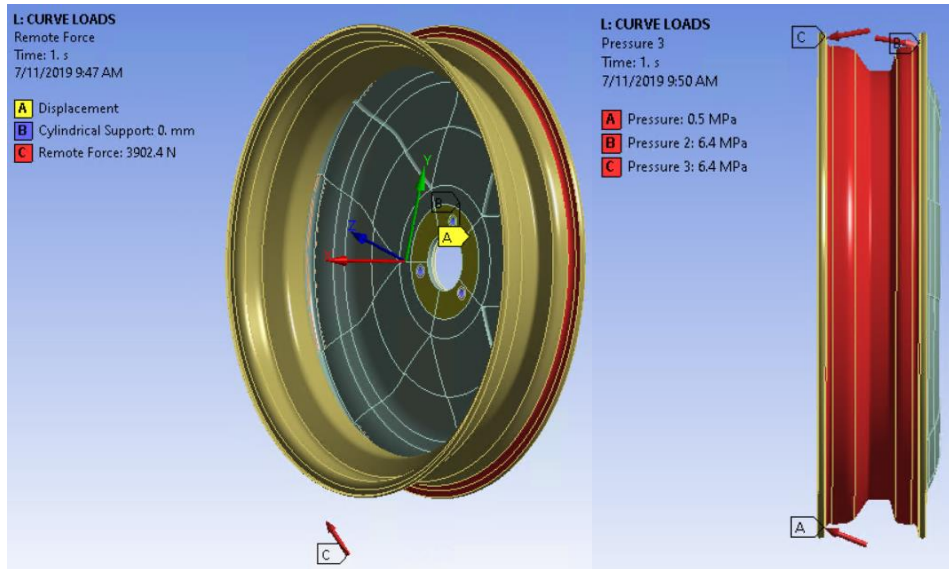


Figure 5.56: Loads and constraints in the curve loads simulation.

### 5.2.12.2.- Results

The total deformation and the inverse reverse factor (Hashin-3D) have been evaluated (figure 5.57).

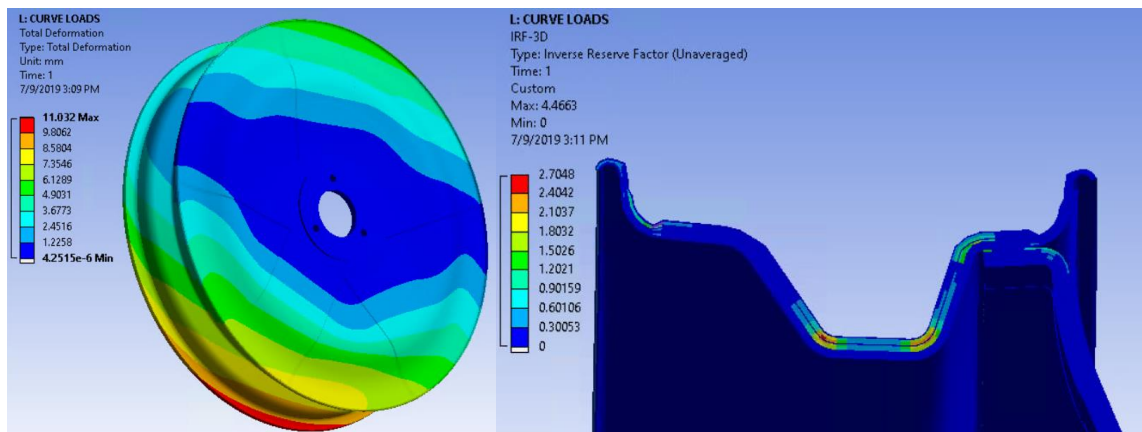


Figure 5.57: Curve loads simulation results.

### 5.2.13.- DOE (direct optimization)

As it has been mentioned before, a direct optimization will be used to determine the optimal stacking sequence of the rim. It has been decided to perform this optimization only

in the rim since, as it has been shown in the results of the previous simulations, this is the most critical component during the load condition of the wheel.

As a starting point, the rim plybook v2.0 will be used as a first approach of the optimal lamination sequence. It should be noted that, the optimal CFRP plybook is not going to be used in the rim production process since due to the project planning, the production of the wheel had to be done before this optimization could have been carried out. For this reason, the lamination sequences used to produce the wheel have been the rim and lens plybooks v2.0.

To perform this optimization, it has been used a simplified FEM model to minimize as much as possible the computation time to obtain the results. The only difference between the final model used to perform the simulations and the simplified model, is that the simplified model is defined as shell (2D) while the final model is defined as solid (3D). The simulation used to perform this optimization has been the inflation pressure simulation.

In figure 5.58, it is shown the flow diagram that represents the entire process that has been done to obtain the optimal rim plybook.

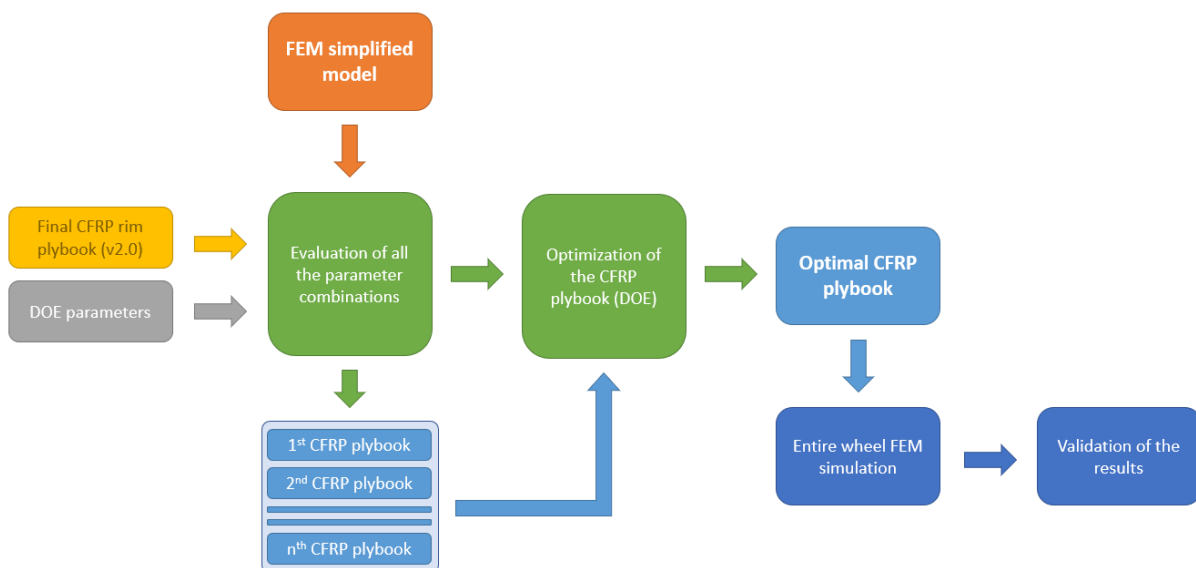


Figure 5.58: Flow diagram of the optimization process.

**5.2.13.1.- Parameters**

For this optimization, three type of input parameters have been used:

- Number of layers: this parameter represents the number of plies of a determined ply material. This variable has been used to evaluate the results using different number of plies of UD T1000 and Twill T300 in some parts of the plybook.
- Ply angle: this parameter defines the orientation of the ply considering the reference system previously defined in ACP (Pre). This variable has been used to evaluate the ply orientation (0° or 45°) in two Twill T300 plies.
- Ply material: this parameter defines the ply material used in a determined ply. This variable has been used to determine if the Twill T300 ply located between the two groups of UD T1000 can be suppressed in the model. What has been done in this variable is to include a material that has a practically zero thickness, in this way, if the results of the simulation show that this material has been chosen, that Twill ply can be deleted from the plybook. The system uses a string list where 1 means that a normal ply of Twill T300 is used, while 2 means that this ply of Twill T300 can be suppressed.

In table 5.7, all the parameters that has been included with their possible respective values are shown:

2	2 TWILL T300 - FINAL		
2	2 UD T1000 (0)		
2			2 TWILL T300 (0) 4-5
1		TWILL T300 (0) 3-4-5	
2		2 TWILL T300 (0) 2-3-4-5	
4			4 UD T1000 (90) 5
2			2 UD T1000 (90) 4-5
1		TWILL T300 (45) 2-3-4-5	
3			3 UD T1000 (90) 4-5
3		3 UD T1000 (90) 3-4-5	
1	TWILL T300 - MOLD		
	Mold surface		

1	Input Parameters			
2	Name	Lower Bound	Upper Bound	
3	P16 - TWILL T300 (0) 3-4-5.ply_material	1	2	
4	P17 - TWILL T300 - MOLD.number_of_layers	1	2	
5	P18 - 2 TWILL T300 (0) 2-3-4-5.number_of_layers	2	3	
6	P19 - TWILL T300 (0) 3-4-5.number_of_layers	1	2	
7	P20 - 2 TWILL T300 (0) 4-5.number_of_layers	2	3	
8	P21 - TWILL T300 (0) 3-4-5.ply_angle	45	0	
9	P22 - 2 TWILL T300 - FINAL.number_of_layers	2	1	
10	P23 - TWILL T300 (45)- 2-3-4-5.ply_angle	45	0	
11	P24 - 4 UD T1000 (90) 5.number_of_layers	4	2	3
12	P25 - 2 UD T1000 (90) 4-5.number_of_layers	2	3	4
13	P26 - 3 UD T1000 (90) 4-5.number_of_layers	3	2	4
14	P27 - 3 UD T1000 (90) 3-4-5.number_of_layers	3	2	4

Table 5.7: List of input parameters.

On the other hand, the output parameters to evaluate the rim plybook have been the maximum values of the inverse reverse factor of Hashin (0.40416), Tsai-Wu (0.66427) and Maximum stress (0.6175) criteria, the maximum directional deformation in the +X direction (1.5777 mm), and the rim weight (759.67 g).

**5.2.13.2.- Objectives and constraints**

For this simulation, the constraints and objectives (table 5.8) that have been defined are the following:

- Minimize the maximum value of the Tsai-Wu inverse reverse factor.
- Minimize the maximum value of the Maximum stress inverse reverse factor.
- Minimize the maximum value of the Hashin inverse reverse factor.
- The weight of the rim must be equal or less than 780 g.
- The sum of the number of plies in each group of UD T1000 must be at most 7. In this way, an excessive thickness is avoided, which could lead to problems of stress concentration.

Table of Schematic G2: Optimization							
	A	B	C	D	E	F	G
1	Name	Parameter	Objective		Constraint		
2			Type	Target	Type	Lower Bound	Upper Bound
3	Minimize P14	P14 - IRF- TsaiWu Maximum	Minimize		No Constraint		
4	Minimize P13	P13 - IRF-MaxStress Maximum	Minimize		No Constraint		
5	Minimize P12	P12 - IRF-Hashin Maximum	Minimize		No Constraint		
6	P15	P15 - Directional Deformation Maximum	No Objective		No Constraint		
7	P29 <= 0.00078	P29 - Sensor.2.weight	No Objective		Values <= Upper Bound		0.00078
*		Select a Parameter					

Parameter Relationships				
	Name	Left Expression	Operator	Right Expression
18	P26+P27 <= 7	P26+P27	<=	7
19	P24+P25 <= 7	P24+P25	<=	7
*	<i>New Parameter Relationship</i>	<i>New Expression</i>	<=	<i>New Expression</i>

Table 5.8: List of objectives and constraints.

**5.2.13.3.- Optimization and candidate points**

The optimization method used is Screening with a number of 260 design points.

First of all, the system generates these points considering all the possible combinations and choosing 260 points that the Screening method determines following its algorithm. Then, each of these 260 combinations is solved consecutively and finally, considering the objectives and constraints, the system determines a list of candidate points (optimal solutions).

The following graphs show the output parameter values of all design points generated for the optimization.

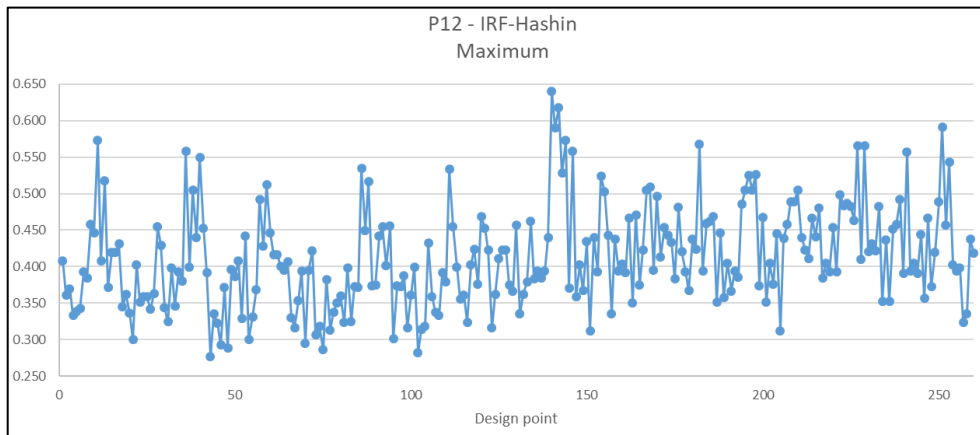


Figure 5.59: Values of the Hashin inverse reverse factor during the optimization.

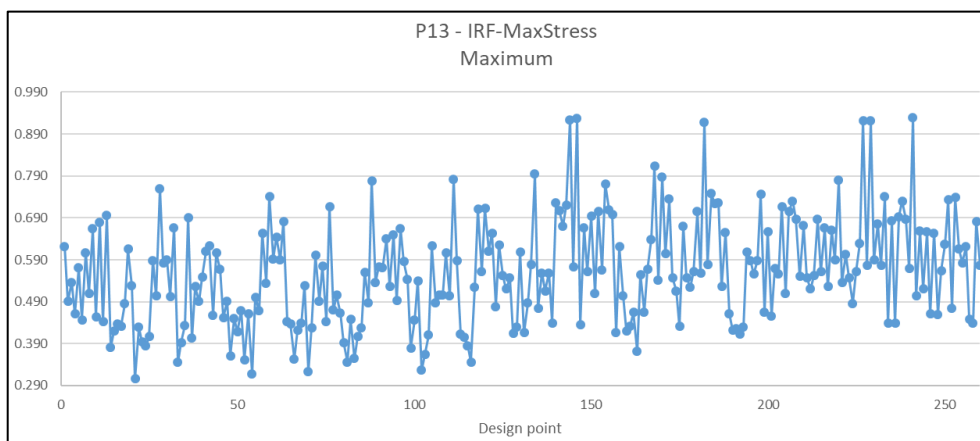


Figure 5.60: Values of the Maximum stress inverse reverse factor during the optimization.

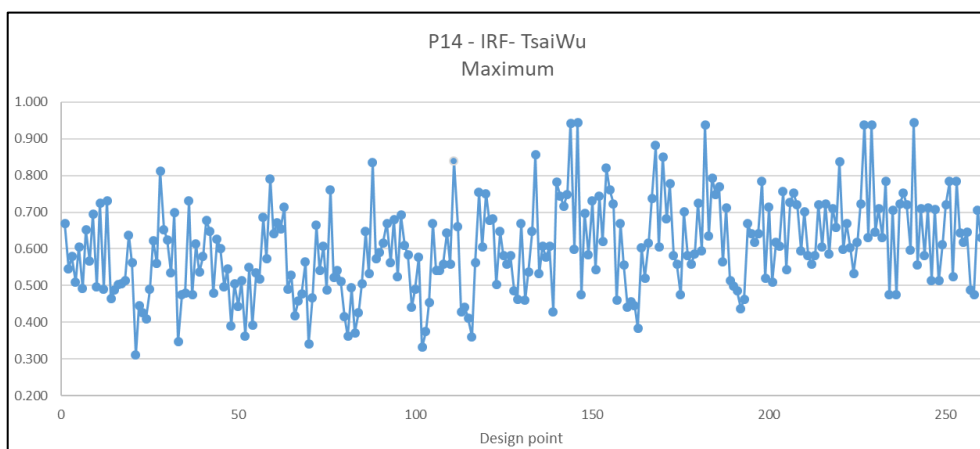


Figure 5.61: Values of the Tsai-Wu inverse reverse factor during the optimization.

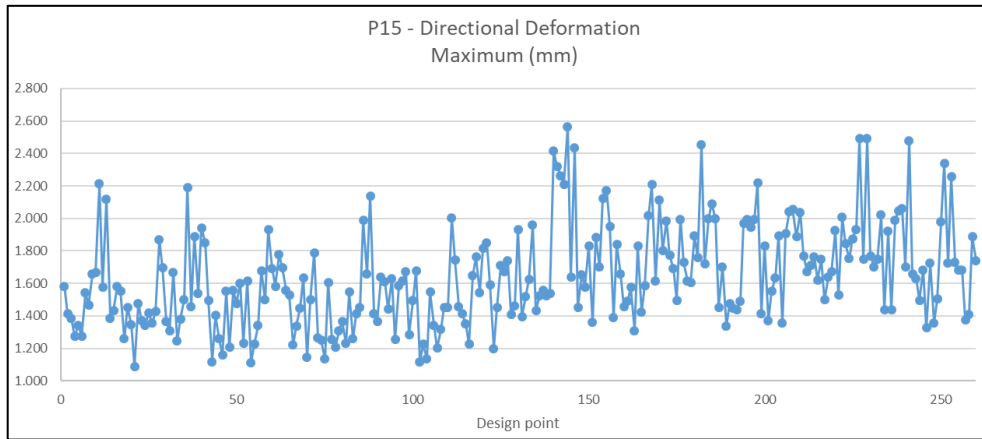


Figure 5.62: Values of the maximum directional deformation during the optimization.

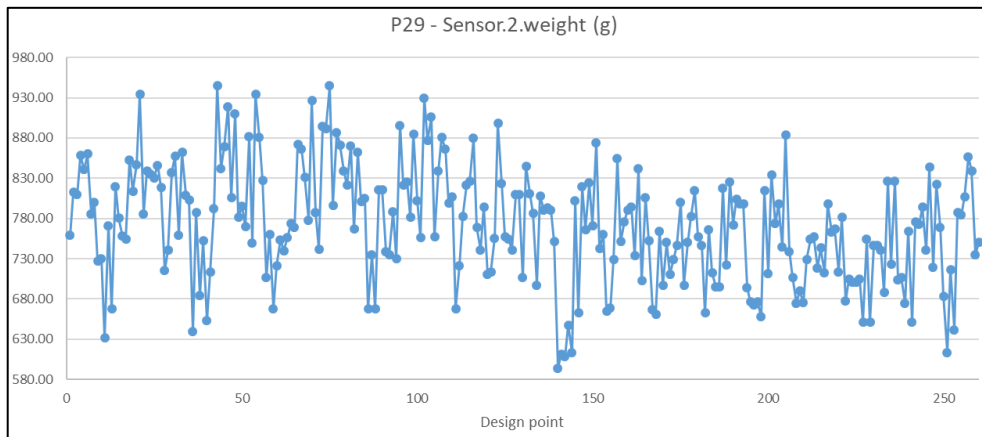


Figure 5.63: Values of the rim weight during the optimization.

In this simulation, five candidate points have been generated choosing the second candidate point as the optimal solution (table 5.9). It has been decided to choose the second since it is the solution that has the lower value of the maximum directional deformation.

Candidate Points	Candidate Point 1	Candidate Point 2	Candidate Point 3	Candidate Point 4	Candidate Point 5
P16 - TWILL T300 (0) 3-4-5.ply_material	1	2	2	1	1
P17 - TWILL T300 - MOLD.number_of_layers	2	1	2	1	2
P18 - 2 TWILL T300 (0) 2-3-4-5.number_of_layers	3	3	3	2	3
P19 - TWILL T300 (0) 3-4-5.number_of_layers	1	2	1	1	1
P20 - 2 TWILL T300 (0) 4-5.number_of_layers	2	2	2	3	3
P21 - TWILL T300 (0) 3-4-5.ply_angle	45	45	0	0	45
P22 - 2 TWILL T300 - FINAL.number_of_layers	1	2	2	2	1
P23 - TWILL T300 (45) 2-3-4-5.ply_angle	0	0	0	0	0
P24 - 4 UD T1000 (90) 5.number_of_layers	4	4	2	4	2
P25 - 2 UD T1000 (90) 4-5.number_of_layers	3	2	2	2	3
P26 - 3 UD T1000 (90) 4-5.number_of_layers	2	2	2	2	2
P27 - 3 UD T1000 (90) 3-4-5.number_of_layers	2	4	3	3	2
P14 - IRF - TsaiWu Maximum	★ 0.49093	★ 0.49941	★★ 0.42904	★ 0.49417	★ 0.49029
P13 - IRF-MaxStress Maximum	★★ 0.44207	★★ 0.42212	★★ 0.43962	★★ 0.44739	★★ 0.44224
P12 - IRF-Hashin Maximum	★ 0.39546	★ 0.40522	— 0.4397	★ 0.39832	★ 0.40824
P15 - Directional Deformation Maximum (mm)	1.5585	1.4746	1.537	1.5476	1.5773
P29 - Sensor.2.weight	★★ 0.00077362	★★ 0.00077201	★★ 0.00075104	★★ 0.00076693	★★ 0.00077092

Table 5.9: List of candidate points.

Therefore, according to the information of the variables of the chosen solution, the optimal rim plybook is the following (table 5.10):

Lamination sequence	n° plies	ply orientation	Zone 1	Zone 2	Zone 3	Zone 4	Zone 5	
			ply type					
↑	2	0°	Twill T300					
	2	0°	UD T1000					
	2	0°				Twill T300		
	3	0°		Twill T300				
	4	90°					UD T1000	
	2	90°				UD T1000		
	1	0°		Twill T300				
	2	90°				UD T1000		
	4	90°			UD T1000			
	1	0°		Twill T300				
			Mold surface					
Thickness (mm)			1.03	1.61	2.29	3.43	4.11	

Table 5.10: Optimal rim plybook.

#### 5.2.13.4.- Results comparison

Finally, this optimal plybook has been evaluated using the 3D solid model of the inflation pressure simulation to compare its results with respect to the previous version (v2.0). In this way, using the same model, it is possible to determine directly the difference in results that exists between the two plybooks.

Below, in figure 5.64 the simulation results of the optimal rim plybook are shown:

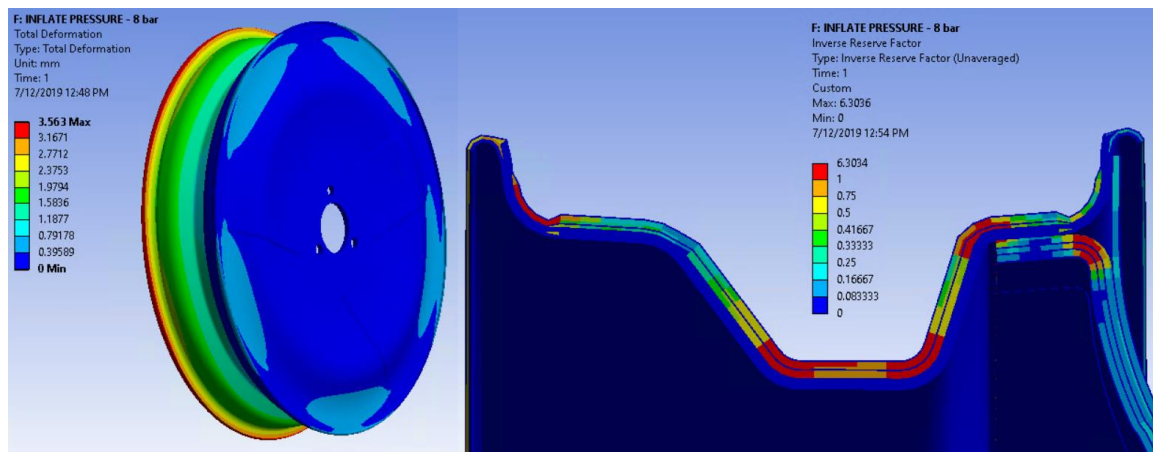


Figure 5.64: Total deformation and Hashin (3D) inverse reverse factor results.

Finally, as it can be observed in the results (table 5.11), it has been possible to reduce the maximum total deformation and the Hashin 3D inverse reverse factor. With these results,

the validation of the simplified model used for the optimization has been confirmed since better results have been obtained in the complete simulation (3D solid model).

	PLYBOOK v2.0 (REFERENCE)	OPTIMAL PLYBOOK	Comparison (%)
Max total deformation (mm)	3.691	3.563	-3.5%
Hashin (3D) inverse reverse factor	6.725	6.303	-6.3%

Table 5.11: Comparison between the results of the different rim plybooks

## 6.- PRODUCTION PROCESS

The production process of the rim and lens is divided in three different phases:

- Lamination of the rim.
- Lamination of the external part of the lens (Lens1).
- Lamination of the inner part of the lens (Lens2).

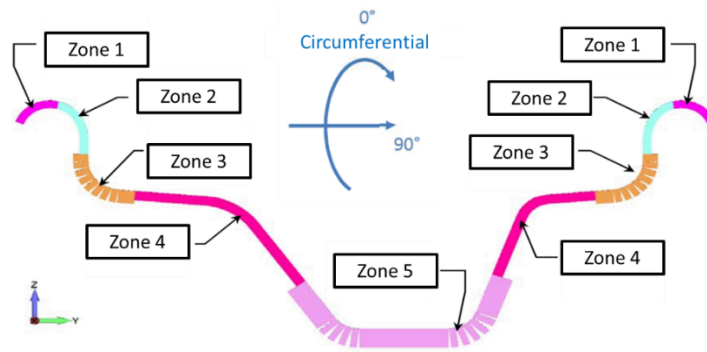
### 6.1.- LAMINATION OF THE RIM

The first step to produce the rim is to fix the different parts of which its mold is composed. This is done using a metal ring which is fixed to the rim mold by pins and screws (figure 6.1).



Figure 6.1: Rim mold assembly process.

Once the mold of the rim is already assembled, the lamination process can be started. As it has been mentioned before, after some simulations comparing different stacking sequences, the final plybook has been decided (table 6.1)



Lamination sequence	n° plies	ply orientation	Zone 1	Zone 2	Zone 3	Zone 4	Zone 5	
			ply type					
↑	2	0°	Twill T300					
	2	0°	UD T1000					
	2	0°				Twill T300		
	1	0°			Twill T300			
	2	0°		Twill T300				
	4	90°					UD T1000	
	2	90°				UD T1000		
	1	45°		Twill T300				
	3	90°				UD T1000		
	3	90°			UD T1000			
	1	0°		Twill T300				
	Mold surface							
Thickness (mm)			1.03	1.38	2.12	3.43	4.11	

Table 6.1: Final rim plybook (v2.0).

First of all, it is necessary to fill the reinforcement of the valve placing Twill T300 plies in the appropriate region of the rim. The depth of the valve hole is 1 mm approximately, which means that is necessary to apply 4 plies of Twill T300 (figure 6.3).

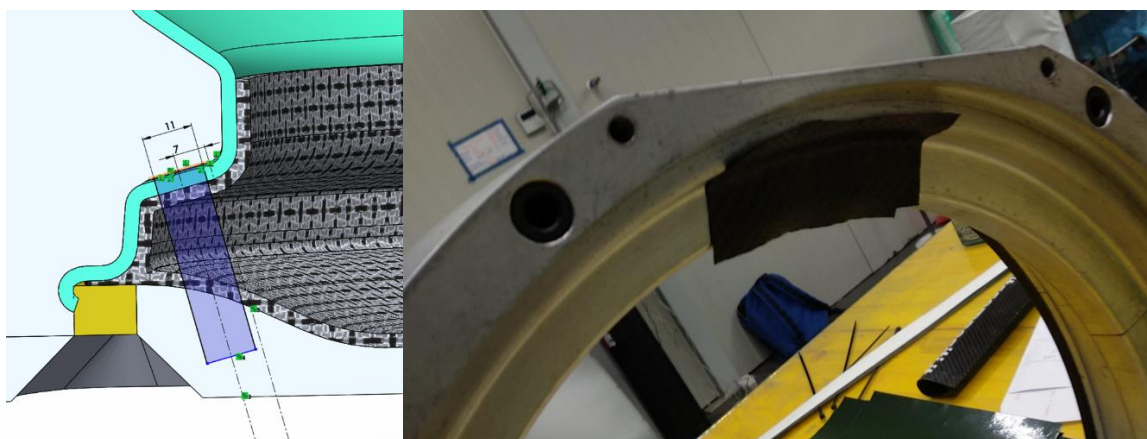


Figure 6.2: Twill T300 plies applied on the valve hole.

Then, the lamination process of the rim can be performed following the plybook lamination steps (figure 6.4).



Figure 6.3: Lamination process of the rim.

## 6.2.- LAMINATION OF THE EXTERNAL PART OF THE LENS (LENS1)

The first step to perform the lamination of the lens is to prepare the lens mold. As it has been explained before, the lens molds includes a silicone ring which is used to push the fibers of the Lens1 against the rim piece which is already produced. Although in figure 6.5, this silicone ring seems totally rigid, in reality, is an element that deforms very easily. For this reason, it has been necessary to fill the holes of the lens mold to keep this ring as straight as possible and thus, be able to perform its function. The material used to cover these holes is the Angeloni Siltec RTV 930 [67] which is a liquid silicone that after 10 minutes approximately, becomes rigid (figure 6.6).



Figure 6.4: Lens mold including the silicone ring (yellow part).

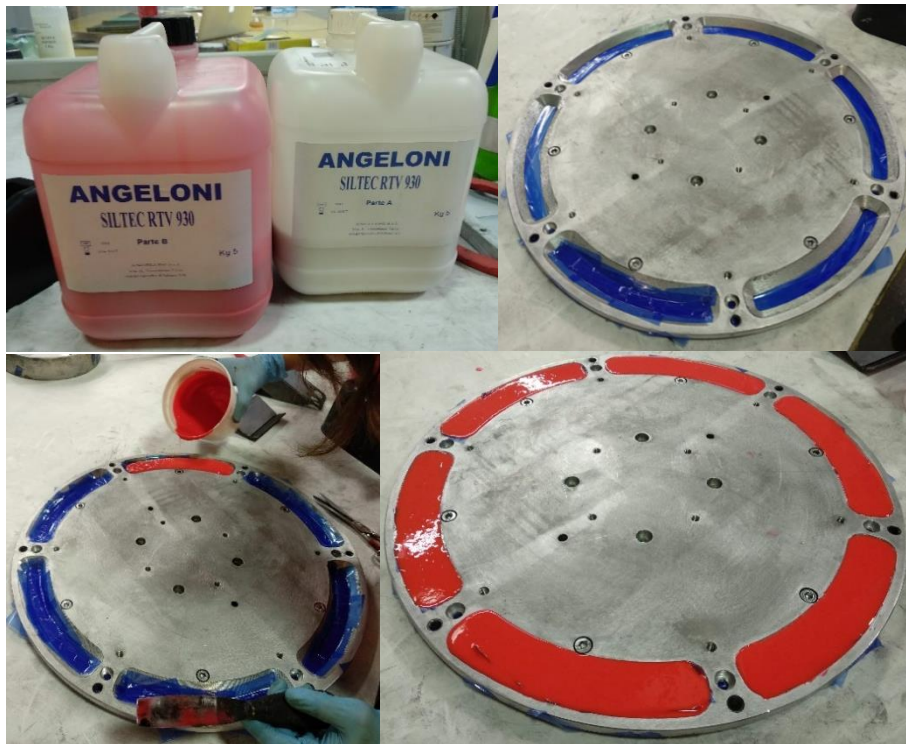


Figure 6.5: Silicone liquid used to fill the holes of the lens mold.

Once this liquid has become solid, the mold should be turned over, and after placing the silicone ring, the lamination process of the lens can be started (figure 6.7).



Figure 6.6: Lens mold already prepared to start the lamination of the external part of the lens.

Then, the lamination process of the Lens1 (figure 6.9) have been done following the stacking sequence determined in the final lens plybook (figure 6.8).

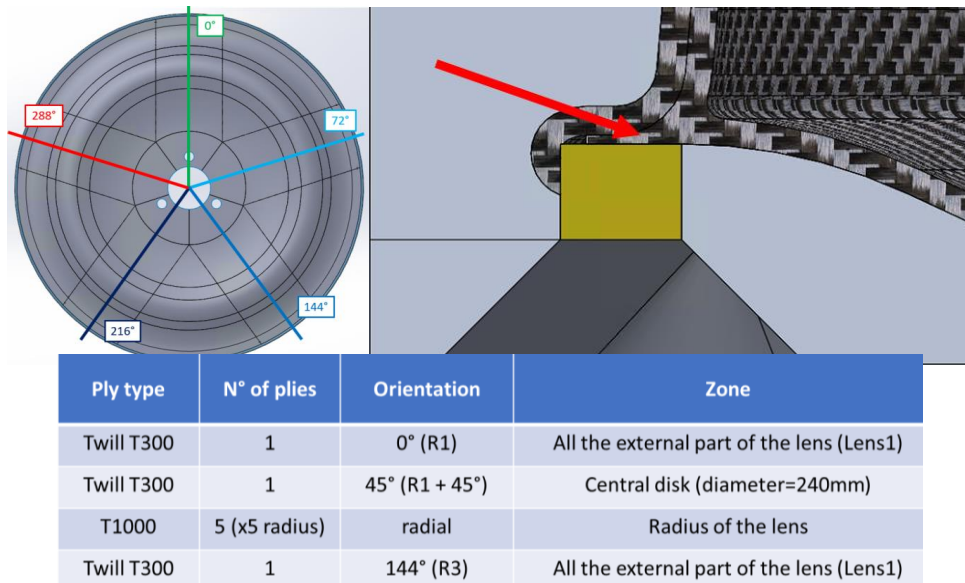


Figure 6.7: Plybook of the external part of the lens (Lens1) (v2.0).

The thickness available between the already laminated rim and the silicone mold is approximately 1 mm (red arrow in figure 6.8). Therefore, only 2 UD T1000 can be applied covering the same region, while the other plies must be scaled to allow the rim and lens to be well compacted during the curing process.



Figure 6.8: Lamination process of the external part of the lens (Lens1).

### 6.3.- LAMINATION OF THE INTERNAL PART OF THE LENS (LENS2)

Before starting the third phase, the rim already produced with its mold must be fixed to the lens mold using pins (figure 6.10). In this way, it is possible to compact all the lens plies which have to reach the rim shape and, after that, start the lamination of the internal part of the lens (table 6.2).



Figure 6.9: Assembly process to combine the lens and rim molds.

Ply type	N° of plies	Orientation	Zone
UD M40J	-	circumferential	To fill the gap between lens and rim
Biax T300	patches	radial	Contact curve between lens and rim
Twill T300	1	189° (R3 + 45°)	Central disk (diameter=240)
T1000	4 (x5 radius)	radial	All the internal part of the lens (Lens2)
Twill T300	1	288° (R5)	All the internal part of the lens (Lens2)
Twill T300	1	333° (R5 + 45°)	Central disk (diameter=240)
T1000	4 (x5 radius)	radial	All the internal part of the lens (Lens2)
Twill T300	1	117° (R2 + 45°)	Central disk (diameter=240)
Twill T300	1	72° (R2)	All the internal part of the lens (Lens2)
T1000	5 (x5 radius)	radial	All the internal part of the lens (Lens2)
Twill T300	1	261° (R4 + 45°)	Central disk (diameter=240)
Twill T300	1	216° (R4)	All the internal part of the lens (Lens2)

Table 6.2:Plybook of the internal part of the lens (Lens2) (v2.0).

First of all, some UD fibers need to be placed circumferentially (3 in figure 5.15), to fill the empty space between lens and rim. It is recommended to put enough UD to increase as much as possible the connection radius of the internal lens (2 in figure 5.15)

After that, the patches of Biaxial T300 have been placed in the region represented in figure 5.40. Finally, the rest of the steps of the lamination process have been performed until obtaining the final lens shape (figure 6.11).



Figure 6.10: Lamination process of the internal part of the lens (Lens 2).

#### 6.4.- MANUFACTURED COMPONENTS

Once the vacuum bag molding and Autoclave curing processes have been carried out, the final rim and lens components have been obtained (figure 6.12).



Figure 6.11: Final version of the composite wheel produced.

## 7.- CONCLUSIONS

The overall aim of this project was to design and optimize some components for the new Emilia 4 motorwheel (figure 7.1). The main design criteria have been to produce lightweight components but always maintaining acceptable safety factors. The components that have been produced are the wheel housing (hub support), the rim and the lens of the wheel.

For the wheel housing, some static structural simulations have been done to optimize its weight using a topology optimization tool, and after that, to evaluate stress, deformation and contact pressure results trying to minimize them to get a component that worked within the required conditions. In addition, the manufacturing process of this piece has been supervised in order to verify its quality and the dimensions that are crucial to have a good performance with the rest of the wheel elements.

For the rim and lens, the design process has been more complex since these components are made using CFRP materials. The first step has been the optimization of the lens shape trying to have a wheel laterally stiff and vertically compliant. Then, some static structural simulations have been done to verify its performance, and after that, the molds to produce these pieces have been done.

Once the final shape of the rim and lens have been decided, several static structural simulations following the TÜV standard and considering the vehicle dynamics have been done to determine the final lamination sequence of these components. Finally, a design of experiment has been performed optimizing the final plybook of the rim using a simplified model. As in the wheel housing case, the manufacturing process has been supervised directly with the producer to control and check all the important parameters during its production.



Figure 7.1: Final assembly of the Emilia 4 new motorwheel.

## 8.- BIBLIOGRAPHY

- [1] [https://en.wikipedia.org/wiki/Solar\\_car](https://en.wikipedia.org/wiki/Solar_car) (Last Access: 26/07/2019)
- [2] [https://en.wikipedia.org/wiki/World\\_Solar\\_Challenge#Objective](https://en.wikipedia.org/wiki/World_Solar_Challenge#Objective) (Last Access: 26/07/2019)
- [3] [https://www.worldsolarchallenge.org/about\\_wsc/overview](https://www.worldsolarchallenge.org/about_wsc/overview) (Last Access: 26/07/2019)
- [4] <http://americansolarchallenge.org/> (Last Access: 26/07/2019)
- [5] <https://www.unibo.it/en/notice-board/emilia-4-the-solar-car-of-the-university-of-bologna-wins-the-american-solar-challenge> (Last Access: 26/07/2019)
- [6] <https://magazine.unibo.it/archivio/2018/07/23/emilia-4-lauto-solare-delluniversita-di-bologna-vince-lamerican-solar-challenge> (Last Access: 26/07/2019)
- [7] [https://www.solbian.eu/en/blog/emilia-4-the-solar-powered-four-seater-100-made-in-italy-n258?utm\\_referrer=https%3A%2F%2Fwww.google.com%2F](https://www.solbian.eu/en/blog/emilia-4-the-solar-powered-four-seater-100-made-in-italy-n258?utm_referrer=https%3A%2F%2Fwww.google.com%2F) (Last Access: 26/07/2019)
- [8] <http://ondasolare.com/il-progetto> (Last Access: 26/07/2019)
- [9] Rondina, F., Taddia, S., Mazzocchetti, L., Donati, L., Minak, G., Rosenberg, P., Bedeschi, A., Dolcini, E. (2018): *Development of full carbon wheels for sport cars with high-volume technology*, Composite Structures.
- [10] [https://mech.utah.edu/composites\\_cars/](https://mech.utah.edu/composites_cars/) (Last Access: 26/07/2019)
- [11] R. A. Ridha (1979): *Fiber-Reinforced Automotive Wheels – Promises and Challenges*. Central Research Labs, The Firestone Tire & Rubber Co. Akron, OH.
- [12] Nicole Scheweizer, Andreas Büter (2012): *Development of a Composite Wheel with Integrated Hub Motor and Requirements on Safety Components in Composite*. Fraunhofer Institute for Structural Durability and System Reliability, Darmstadt, Germany.
- [13] James A. Woefel (1981) US Patent 4294490: *Fiber-reinforced Composite Wheel Construction*. Motor Wheel Corporation, Lansing, Michigan, US.
- [14] <http://www.ecv1.com/e-cerchi.htm> (Last Access: 26/07/2019)

- [15] Malcolm K. McDougall (1988) US Patent 4749235: *Composite Wheel Construction*. The Budd Company, Troy, Michigan, US.
- [16] <https://www.slashgear.com/koenigsegg-aircore-carbon-fiber-wheels-appear-in-metal-free-hollow-construction-24279221/> (Last Access: 26/07/2019)
- [17] <http://www.carimproject.eu/> (Last Access: 26/07/2019)
- [18] <https://auto.howstuffworks.com/in-wheel-motor.htm> (Last Access: 26/07/2019)
- [19] <https://www.machinedesign.com/automotive/hub-motors-all-electric-vehicles-still-have-some-technological-challenges-overcome> (Last Access: 26/07/2019)
- [20] <https://www.proteanelectric.com/> (Last Access: 26/07/2019)
- [21] [https://www.motorauthority.com/news/1030025\\_michelins-active-wheel-technology-in-detail](https://www.motorauthority.com/news/1030025_michelins-active-wheel-technology-in-detail) (Last Access: 26/07/2019)
- [22] [https://www.researchgate.net/figure/Michelin-active-tire-with-in-wheel-motor\\_fig2\\_276242559](https://www.researchgate.net/figure/Michelin-active-tire-with-in-wheel-motor_fig2_276242559) (Last Access: 26/07/2019)
- [23] <https://www.machinedesign.com/automotive/hub-motors-all-electric-vehicles-still-have-some-technological-challenges-overcome> (Last Access: 26/07/2019)
- [24] <https://www.wfb-bremen.de/en/page/bremen-invest/engineers-from-bremen-are-working-on-electric-drive-systems-of-the-future> (Last Access: 26/07/2019)
- [25] Schweizer, N., Giessl, A., Schwarzhaupt, O. and Büter, A. (2012): *Development of a Composite Wheel with Integrated Hub Motor*. 15th European Conference on composite materials (ECCM15), 24–29 June, Venice, Italy.
- [26] <https://towardsdatascience.com/introduction-to-evolutionary-algorithms-a8594b484ac> (Last Access: 26/07/2019)
- [27] M. Giger and P. Ermanni (2005): *Development of CFRP racing motorcycle rims using a heuristic evolutionary algorithm approach*. Centre of Structure Technologies, Institute of Mechanical Systems, Swiss Federal Institute of Technology, Zurich, Switzerland.
- [28] <https://asq.org/quality-resources/design-of-experiments> (Last Access: 26/07/2019)
- [29] [https://www.sharcnet.ca/Software/Ansys/17.0/en-us/help/wb\\_dx/dxwhatis.html](https://www.sharcnet.ca/Software/Ansys/17.0/en-us/help/wb_dx/dxwhatis.html) (Last Access: 26/07/2019)

- [30] [https://www.sharcnet.ca/Software/Ansys/16.2.3/en-us/help/wb\\_dx/dx\\_uselocalsen.html](https://www.sharcnet.ca/Software/Ansys/16.2.3/en-us/help/wb_dx/dx_uselocalsen.html) (Last Access: 26/07/2019)
- [31] [https://www.sharcnet.ca/Software/Ansys/16.2.3/en-us/help/wb\\_dx/dxmethoddef.html](https://www.sharcnet.ca/Software/Ansys/16.2.3/en-us/help/wb_dx/dxmethoddef.html) (Last Access: 26/07/2019)
- [32] <https://caesai.com/blog/how-does-my-doe-model-determine-how-many-design-points-generate> (Last Access: 26/07/2019)
- [33] [http://designinformaticslab.github.io/productdesign\\_tutorial/2016/11/20/ansys.html#introduction](http://designinformaticslab.github.io/productdesign_tutorial/2016/11/20/ansys.html#introduction) (Last Access: 26/07/2019)
- [34] [https://www.sharcnet.ca/Software/Ansys/17.0/en-us/help/wb\\_dx/dx\\_Interpolation\\_o\\_r.html](https://www.sharcnet.ca/Software/Ansys/17.0/en-us/help/wb_dx/dx_Interpolation_o_r.html) (Last Access: 26/07/2019)
- [35] <https://caesai.com/blog/design-optimization-finite-element-analysis> (Last Access: 26/07/2019)
- [36] [http://designinformaticslab.github.io/productdesign\\_tutorial/2016/11/20/ansys.html#introduction](http://designinformaticslab.github.io/productdesign_tutorial/2016/11/20/ansys.html#introduction) (Last Access: 26/07/2019)
- [37] <https://www.ansys.com/products/platform/ansys-designxplorer/designxplorer-capabilities#cap3> (Last Access: 26/07/2019)
- [38] <https://caesai.com/blog/design-optimization-finite-element-analysis> (Last Access: 26/07/2019)
- [39] [https://www.sharcnet.ca/Software/Ansys/17.0/en-us/help/wb\\_dx/dx\\_optimization\\_options.html](https://www.sharcnet.ca/Software/Ansys/17.0/en-us/help/wb_dx/dx_optimization_options.html) (Last Access: 26/07/2019)
- [40] TÜV, Guidelines for Testing Special Wheels for Vehicles and their Trailers, 29-01-2004
- [41] JASO T203-85, Light alloy wheels for motorcycles, 27-03-1985
- [42] WSC Michelin tire 95-80 R16 datasheet
- [43] J.Stearns, T.S.Srivatsan, X.Gao, and P.C.Lam (2005): *Understanding the Influence of Pressure and Radial Loads on Stress and Displacement Response of a Rotating Body: The Automobile wheel*. Department of Mechanical Engineering, The University of Akron, USA.

- [44] <http://asm.matweb.com/search/SpecificMaterial.asp?bassnum=MA7075T6>  
(Last Access: 26/07/2019)
- [45] [http://metallurgicaveneta.it/pdf/acciai\\_per\\_molle/52SiCrNi5.pdf](http://metallurgicaveneta.it/pdf/acciai_per_molle/52SiCrNi5.pdf) (Last Access: 26/07/2019)
- [46] <https://www.skf.com/it/products/bearings-units-housings/ball-bearings/deep-groove-ball-bearings/deep-groove-ball-bearings/index.html?designation=6004-2Z> (Last Access: 26/07/2019)
- [47] <https://www.skf.com/it/products/bearings-units-housings/ball-bearings/deep-groove-ball-bearings/deep-groove-ball-bearings/index.html?designation=6005-2Z> (Last Access: 26/07/2019)
- [48] [http://www.rodalsa.net/?page\\_id=4231](http://www.rodalsa.net/?page_id=4231) (Last Access: 26/07/2019)
- [49] <http://www.victoriasas.it/Prodotti-per-categoria/BOCCOLE/BOCCOLE-CON-COLLARE-DIN-172-CORTE-cod-72> (Last Access: 26/07/2019)
- [50] <https://www.unisalento.it/documents/20152/250080/dati+e+tabelle+utili+2015.doc/55977778-858b-5ee3-fabe-33bc22020867?version=1.0> (Last Access: 26/07/2019)
- [51] <https://road.cc/content/news/114442-paul-lew-talks-wheel-dynamics> (Last Access: 26/07/2019)
- [52] Laboratorio di Progettazione con Materiali Compositi course. Dipartimento di Ingegneria Meccanica (DIN), University of Bologna.
- [53] <https://www.azom.com/article.aspx?ArticleID=8353> (Last Access: 26/07/2019)
- [54] [https://www.sharcnet.ca/Software/Ansys/16.2.3/en-us/help/acp\\_ug/Tsai-Hill\\_failure\\_criterion.html](https://www.sharcnet.ca/Software/Ansys/16.2.3/en-us/help/acp_ug/Tsai-Hill_failure_criterion.html) (Last Access: 26/07/2019)
- [55] R. Jones (1999): *Mechanics of Composite Materials*. Taylor & Francis. pp. 109-112.
- [56] [https://www.sharcnet.ca/Software/Ansys/16.2.3/en-us/help/acp\\_ug/Tsai\\_Wu.html](https://www.sharcnet.ca/Software/Ansys/16.2.3/en-us/help/acp_ug/Tsai_Wu.html)  
(Last Access: 26/07/2019)
- [57] [https://www.sharcnet.ca/Software/Ansys/17.0/en-us/help/acp\\_ug/hashin\\_fail\\_crit.html](https://www.sharcnet.ca/Software/Ansys/17.0/en-us/help/acp_ug/hashin_fail_crit.html)  
(Last Access: 26/07/2019)
- [58] [https://www.sharcnet.ca/Software/Ansys/17.0/en-us/help/acp\\_ug/Max\\_stress\\_](https://www.sharcnet.ca/Software/Ansys/17.0/en-us/help/acp_ug/Max_stress_)



criterion.html (Last Access: 26/07/2019)

[59] [http://stg.toray.testcrafting.com/file\\_viewer.php?id=4471](http://stg.toray.testcrafting.com/file_viewer.php?id=4471) (Last Access: 26/07/2019)

[60] <http://www.nauticexpo.com/prod/angeloni/product-39168-297766.html> (Last Access: 26/07/2019)

[61] [https://www.sharcnet.ca/Software/Ansys/17.0/en-us/help/acp\\_ug/acp\\_Rosettes.html](https://www.sharcnet.ca/Software/Ansys/17.0/en-us/help/acp_ug/acp_Rosettes.html)  
(Last Access: 26/07/2019)

[62] [https://www.sharcnet.ca/Software/Ansys/17.0/en-us/help/acp\\_ug/acp\\_oes.html](https://www.sharcnet.ca/Software/Ansys/17.0/en-us/help/acp_ug/acp_oes.html)  
(Last Access: 26/07/2019)

[63] [https://www.sharcnet.ca/Software/Ansys/17.0/en-us/help/acp\\_ug/acp\\_modeling\\_ply.html](https://www.sharcnet.ca/Software/Ansys/17.0/en-us/help/acp_ug/acp_modeling_ply.html) (Last Access: 26/07/2019)

[64] [https://www.sharcnet.ca/Software/Ansys/17.0/en-us/help/acp\\_ug/solid\\_model\\_general.html](https://www.sharcnet.ca/Software/Ansys/17.0/en-us/help/acp_ug/solid_model_general.html) (Last Access: 26/07/2019)

[65] [https://www.toraycma.com/file\\_viewer.php?id=4462](https://www.toraycma.com/file_viewer.php?id=4462) (Last Access: 26/07/2019)

[66] [https://www.toraycma.com/file\\_viewer.php?id=4465](https://www.toraycma.com/file_viewer.php?id=4465) (Last Access: 26/07/2019)

[67] <http://www.g-angeloni.it/elenco-prodotti/siliconi-e-gomme/rtv-930/> (Last Access: 26/07/2019)

[68] VDI 2230 Systematic calculation of high duty bolted joints with one cylindrical bolt

[69] ISO 68-1 ISO general purpose screw threads —Basic profile

[70] G. Niemann, H. Winter, B.R. Hohn - Manuale degli organi delle macchine (2006)

# 9.- ANNEX I.- CALCULATION OF THE BOLT PRETENTION

To obtain the theoretical value of the bolt pretension between the ferrule and the wheel housing, the standard VDI 2230 [68] of design calculation and assessment for threaded joints has been used. Using this standard is possible to calculate the maximum value of the allowed assembly preload which is based on the equivalent stress formula.

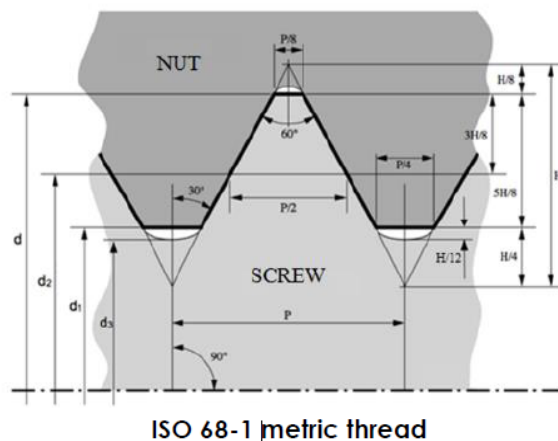
$$\sigma_{eq} = \sqrt{\left(\frac{F_i}{A_t}\right)^2 + 3 \cdot \left(\frac{M_{shank}}{W_t}\right)^2} = \sqrt{F_i^2 + 48 \cdot \left(F_i \cdot \frac{(0,16 \cdot p + 0,58 \cdot \mu_{th} \cdot d_2)}{d_t}\right)^2} \cdot \frac{1}{A_t} \leq v \cdot R_{p0.2} = S_p$$

This equation represents the equivalent stress acting on a screw considering the normal stresses due to the bolt pretension, and the shear stresses due to the torque.

Before performing the calculation of the maximum bolt pretension  $F_i$ , some basic parameters or the screw must be defined (figure 9.1):

## THREADED JOINTS: KEY DIMENSIONS

ISO basic thread profile according to ISO 68-1



- d nominal screw diameter
- d<sub>1</sub> minimum nut thread diameter
- d<sub>2</sub> mean thread diameter
- d<sub>3</sub> minimum screw thread diameter
- d<sub>4</sub> stress diameter
- H basic triangle height
- P thread pitch

$$H = \frac{\sqrt{3}}{2} P$$

$$d_1 = d - 1,08253 \cdot P$$

$$d_2 = d - 0,64952 \cdot P$$

$$d_3 = d - 1,22687 \cdot P$$

$$d_4 = (d_2 + d_3) / 2 = d - 0,9382 \cdot P$$

Figure 9.1: ISO basic thread profile dimensions according to ISO 68-1 [69].

After obtaining these geometrical parameters, an Excel sheet has been done including all the calculations (table 9.1):

d	52	mm	Nominal diameter of the screw
d_int	45	mm	Inner diameter of the screw
p	3	mm	Thread pitch
d_t	49.19	mm	Stress diameter
d_1	48.75	mm	Minimum nut thread diameter
d_2	50.05	mm	Mean thread diameter
μ_th	0.25		Coefficient of friction between Al-Al
At	309.61	mm <sup>2</sup>	Stress area
v	0.40		Screw utilization factor with respect to the yield point (for standard applications is between 0.7 and 0.9)
Rp_0.2	450	Mpa	Yield strength of aluminium
<b>F_i</b>	<b>37681</b>	<b>N</b>	<b>Maximum axial preload</b>

Table 9.1: Excel calculations to obtain the maximum axial preload of the screw.

For these calculations, it has to be considered that, this is not a standard application because the screw on this component has an inner hole where it is located the 6004-Z bearing. Because of this, the stress area has a different value than the regular one for bolts in this standard.

The stress area in this case is calculated as:

$$A_t = \frac{\pi (d_t^2 - d_{int}^2)}{4} = \frac{\pi (49.19^2 - 45^2)}{4} = 309.61 \text{ mm}^2$$

Moreover, for this model, it has been reduced the screw utilization factor with respect to the yield point, because as it is said before, this is not a standard case and is not possible to reach the same values in some coefficients.

As it can be seen in the results before, the final value of the maximum axial preload is 37681 N. Despite this, for the final simulation, it has been decided to round the value of the maximum bolt pretension up to 40000 N. The previous value represents the maximum value that theoretically could be obtained with the parameters mentioned previously using the VDI 2230 standard. However, in reality, it is impossible to reach a pretension of this value for this type of application.

## 10.- ANNEX II.- CALCULATION OF THE CONTACT PRESSURE

In this section, the calculations to obtain the theoretical value of the contact pressure have been done. The assumptions considered in this case to calculate this pressure are the following:

- It does not allow the articulation of the components.
- The pins serve to centre the components.

For the first three simulations, it is only considered one contact surface. This surface corresponds to the contact between the pins and the holes where they are located.

On the other hand, in the final assembly, there are two different contact areas. These two areas are, the contact between pins and the inner diameter of the bushes (region 2), and the other one is the contact between the external diameter of the bushes and the holes (region 1) where they are located (figure 10.1).

Because of this, two different calculations have been performed to obtain the contact pressure value, one for each region.

In this case, these are the input parameters to do the calculations:

- Number of pins: 3.
- Maximum torsion moment: 740 Nm.
- Diameter of the circumference which defines the distance between the holes and the revolution axis of the component: 77 mm.
- Modulus of the tangential force due to the effect of the torsion moment on each pin: 3200 N.

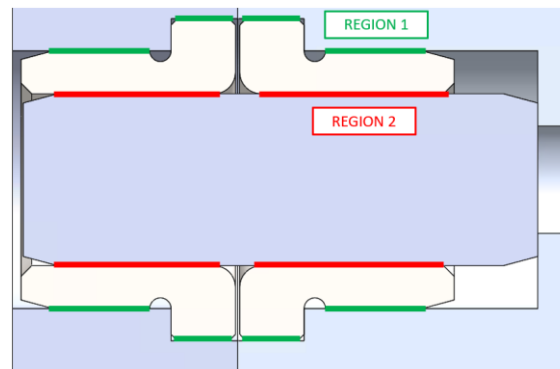


Figure 10.1: Detail of the two different contact regions.

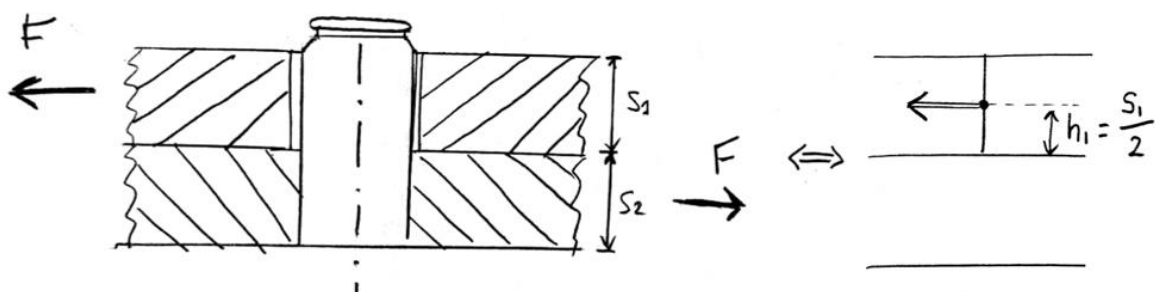
As it can be seen in the figure above, due to the geometrical parameters of these components, there is a discontinuity in both regions. Because of this, the results obtained using these calculations are only an approximation of the real performance of the components. However, it is useful to know this value to compare it with the FEM results.

To perform these calculations, the contact must be verified in three different ways [70]:

- Bending assessment.
- Shear assessment.
- Admissible contact assessment.

### 10.1.- BENDING ASSESSMENT

In this case, it only makes sense to study the effect of the bending moment in the region 2, that is, to determine if these pins work for this specific application. The following picture represents in a schematic way, the bending effect that two plates with a shear force has on a single pin. As it can be observed, this simplified case is very similar to the real one.



With the following formulas, it is possible to obtain the maximum bending moment that these pins suffer and compare this value with the admissible stress of the pins which is 360 MPa.

$$\sigma_f = \frac{M_f}{W_f} = \frac{F * h}{\pi * d^3} 32 \leq \sigma_{adm}$$

$$\sigma_{adm} = 360 \text{ MPa} = \frac{S_y}{CS}$$

The input parameters to obtain these values are shown in table 10.1:

d_pin	8	mm
s1	9	mm
s2	9	mm
h1	4.5	mm
h2	4.5	mm

Table 10.1: Input parameters.

The calculations show that the safety factor (CS) is over one and therefore, these pins are suitable in terms of bending effect (table 10.2).

Wf	50	mm <sup>3</sup>
Mf	14399	N*mm
σ_f	286	MPa
σ_adm	360	MPa
CS	1.26	
CS_Sy	1.89	

Table 10.2: Results of the bending assessment.

## 10.2.- SHEAR ASSESSMENT

To perform the shear assessment, the maximum shear stress and the safety factor have been calculated using the following formulas. The admissible shear stress of the pins is 208 MPa.

$$\tau_{max} = \frac{F}{A} = \frac{4 F}{\pi * d^2} \leq \tau_{adm}$$

$$\tau_{adm} = 208 \text{ MPa} = \frac{\sigma_{adm}}{\sqrt{3}} = \frac{S_y}{\sqrt{3} CS}$$

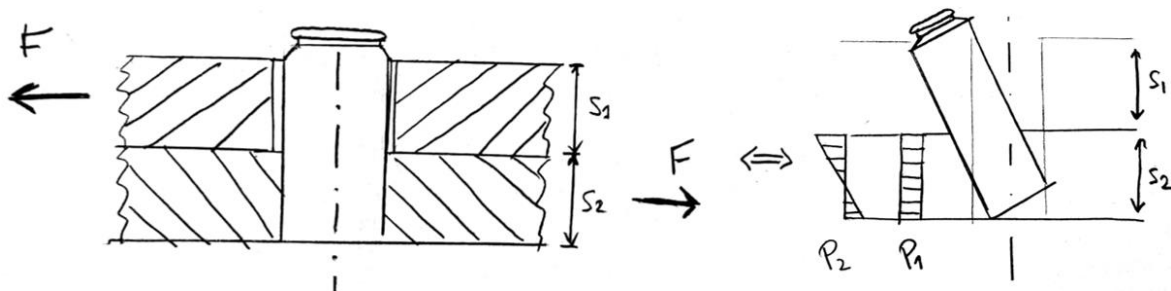
τ_max	64	MPa
τ_adm	208	MPa
CS	3.3	

Table 10.3: Results of the shear assessment.

As it can be seen in the results (table 10.3), for the shear assessment, these pins have been validated since its safety factor is over one.

### 10.3.- ADMISSIBLE CONTACT PRESSURE ASSESSMENT

In this case, to obtain evaluate the contact pressure it is necessary to calculate the results in both regions. The following picture represents in a schematic way, the pressure distributions that appear when a shear force is applied between two different plates and a pin.



The formulas to obtain that pressure distributions are shown below.

$$P_1 = \frac{F}{s * d} = \frac{S_y}{\sqrt{3} CS}$$

$$P_2 = \frac{F}{s * d} * 6 \left( \frac{h}{s} + \frac{1}{2} \right)$$

$$P_{max} = P_1 + P_2$$

#### 10.3.1.- Region 2

For this region, two different cases must be considered. The contact pressure magnitude is the same, but the pins are made of C40 steel (Admissible pressure = 800 MPa) and the bushes are made of UNI 18NiCrMo5 steel (Admissible pressure = 1400 MPa).

P1	44	Mpa
P2	400	MPa
P_max	444	MPa
P_adm_bush	1400	Mpa
CS_bush	3.15	
P_adm_pin	800	MPa
CS_pin	1.80	

Table 10.4: Contact pressure calculations in region 2.

As it can be seen in the results (table 10.4), the two materials are validated for this application since its safety factors, CS\_bush and CS\_pin, are over 1.

### 10.3.2.- Region 1

In this region, the contact occurs between the steel of the bushes (Admissible pressure = 1400 MPa) and the aluminium of the wheel housing (Admissible pressure = 381 MPa)

P1	38	Mpa
P2	343	MPa
P_max	381	MPa
P_adm_Al	383	Mpa
CS_Al	1.01	
P_adm_bush	1400	Mpa
CS_bush	3.68	

Table 10.5: Contact pressure calculations in region 1.

As in the previous case, all the safety factors are over 1 which means that these two materials are suitable (table 10.5).

# 11.- ANNEX III.- COMPOSITE MATERIALS DATA

In this annex, all the composite materials data used to perform the simulations are shown. To obtain this data, some calculations have been performed based on the micromechanics of composite materials [52].

## 11.1.- T1000 UD

In this case, the T1000 UD has a fiber mass of 140 g/m<sup>2</sup> with a resin percentage of 36%.

From that parameters, it has been calculated the prepreg data as well as the main properties of the matrix and fiber (table 11.1)

Prepreg datasheet		Prepreg	
Fiber	T1000	Mass	218.75 [g/m <sup>2</sup> ]
Type	UD	Fiber mass	64.0%
Fiber mass	140 [g/m <sup>2</sup> ]	Fiber volume	54.2%
Angle	0 [°]	Matrix volume	45.8%
Resin % in mass	36%	Density	1.525 [g/cm <sup>3</sup> ]
Fiber data		Thickness	0.143 [mm]
Elastic modulus	294000 [Mpa]	E1	160373 [Mpa]
Strength	6370 [Mpa]	E2	8997 [Mpa]
Shear modulus	50000 [Mpa]	E3	8997 [Mpa]
Maximum elongation	2.2%	v12	0.3275
Poisson	0.30	v13	0.3275
Density	1.8 [g/cm <sup>3</sup> ]	v21	0.0184
Alpha	-8.00E-07 [1/°C]	v31	0.0184
Matrix data		v23	0.3986
Density	1.2 [g/cm <sup>3</sup> ]	v32	0.3986
Elastic modulus	2000 [Mpa]	G12	5041 [Mpa]
Strength	40 [Mpa]	G13	5041 [Mpa]
Shear modulus	1600 [Mpa]	G23	3216 [Mpa]
Poisson	0.36	alfa1	-4.53E-07 [1/°C]
Maximum elongation	2.0%	alfa2	3.69E-05 [1/°C]
Alpha	6.00E-05 [1/°C]	alfa3	3.69E-05 [1/°C]
Conductivity	0.2 [W/m°C]	sig 1 tension	3473 [Mpa]
Thermal capacity	1000 [J/Kg°C]	sig 2 tension	30 [Mpa]
		sig 3 tension	30 [Mpa]
		sig 1 compression	-1579 [Mpa]
		sig 2 compression	-99 [Mpa]
		sig 3 compression	-99 [Mpa]
		shear XY	60 [Mpa]
		shear YZ	30 [Mpa]
		shear XZ	60 [Mpa]

Table 11.1: T1000 UD properties.

For this material, the values of the elastic modulus and the tensile stress in X direction have been decreased with respect to their theoretical values to keep a certain margin of safety (table 11.2).

UD T1000 Prepreg

Data	Density	1.53	[g/cm <sup>3</sup> ]
------	---------	------	----------------------

Coefficient of thermal expansion	Direction X	-4.53E-07	[1/°C]
	Direction Y	3.69E-05	[1/°C]
	Direction Z	3.69E-05	[1/°C]

Orthotropic Elasticity	Young's Modulus X	148300	[Mpa]
	Young's Modulus Y	8997	[Mpa]
	Young's Modulus Z	8997	[Mpa]
	Poisson's Ratio XY	0.33	
	Poisson's Ratio YZ	0.40	
	Poisson's Ratio XZ	0.33	
	Shear Modulus XY	5041	[Mpa]
	Shear Modulus YZ	3216	[Mpa]
	Shear Modulus XZ	5041	[Mpa]

Stress Limits	Tensile X	2845	[Mpa]
	Tensile Y	30	[Mpa]
	Tensile Z	30	[Mpa]
	Compressive X	-1579	[Mpa]
	Compressive Y	-99	[Mpa]
	Compressive Z	-99	[Mpa]
	Shear XY	60	[Mpa]
	Shear YZ	30	[Mpa]
	Shear XZ	60	[Mpa]

Strain Limits	Tensile X	0.0192
	Tensile Y	0.0033
	Tensile Z	0.0033
	Compressive X	-0.0106
	Compressive Y	-0.0110
	Compressive Z	-0.0110
	Shear XY	0.0119
	Shear YZ	0.0093
	Shear XZ	0.0119

Tsai-Wu Constant	Coupling Coefficient XY	-1
	Coupling Coefficient YZ	-1
	Coupling Coefficient XZ	-1

Puck Constant	Compressive Inclination XZ	0.30
	Compressive Inclination YZ	0.25
	Tensile Inclination XZ	0.35
	Tensile Inclination YZ	0.25
	Interface Weaking Factor	0.8
	Degradation Parameter s	0.5
	Degradation Parameter M	0.5

Table 11.2: T1000 UD Engineering data.

### 11.2.- M40J UD

The M40J UD has a fiber mass of 300 g/m<sup>2</sup> with a resin percentage of 38%.

Prepreg datasheet					
Fiber		M40J			
Type		UD			
Fiber mass		300 [g/m <sup>2</sup> ]			
Angle		0 [°]			
Resin % in mass		38%			
Fiber data					
Elastic modulus		377000 [Mpa]			
Strength		4400 [Mpa]			
Shear modulus		50000 [Mpa]			
Maximum elongation		1.2%			
Poisson		0.30			
Density		1.77 [g/cm <sup>3</sup> ]			
Alpha		-8.00E-07 [1/°C]			
Matrix data					
Density		1.2 [g/cm <sup>3</sup> ]			
Elastic modulus		2000 [Mpa]			
Strength		40 [Mpa]			
Shear modulus		1600 [Mpa]			
Poisson		0.36			
Maximum elongation		2.0%			
Alpha		6.00E-05 [1/°C]			
Conductivity		0.2 [W/m°C]			
Thermal capacity		1000 [J/Kg°C]			
Prepreg					
Mass		483.87 [g/m <sup>2</sup> ]			
Fiber mass		62.0%			
Fiber volume		52.5%			
Matrix volume		47.5%			
Density		1.499 [g/cm <sup>3</sup> ]			
Thickness		0.3227 [mm]			
E1		198950 [Mpa]			
E2		8553 [Mpa]			
E3		8553 [Mpa]			
v12		0.3285			
v13		0.3285			
v21		0.0141			
v31		0.0141			
v23		0.4126			
v32		0.4126			
G12		4794 [Mpa]			
G13		4794 [Mpa]			
G23		3027 [Mpa]			
alfa1		-5.10E-07 [1/°C]			
alfa2		3.84E-05 [1/°C]			
alfa3		3.84E-05 [1/°C]			
sig 1 tension		2330 [Mpa]			
sig 2 tension		30 [Mpa]			
sig 3 tension		30 [Mpa]			
sig 1 compression		-1059 [Mpa]			
sig 2 compression		-99 [Mpa]			
sig 3 compression		-99 [Mpa]			
shear XY		60 [Mpa]			
shear YZ		30 [Mpa]			
shear XZ		60 [Mpa]			

Table 11.3: M40J UD properties.

UD M40J Prepreg

Data	Density	1.50	[g/cm <sup>3</sup> ]
------	---------	------	----------------------

Coefficient of thermal expansion	Direction X	-5.10E-07	[1/°C]
	Direction Y	3.84E-05	[1/°C]
	Direction Z	3.84E-05	[1/°C]

Orthotropic Elasticity	Young's Modulus X	198950	[Mpa]
	Young's Modulus Y	8553	[Mpa]
	Young's Modulus Z	8553	[Mpa]
	Poisson's Ratio XY	0.33	
	Poisson's Ratio YZ	0.41	
	Poisson's Ratio XZ	0.33	
	Shear Modulus XY	4794	[Mpa]
	Shear Modulus YZ	3027	[Mpa]
	Shear Modulus XZ	4794	[Mpa]

Stress Limits	Tensile X	2330	[Mpa]
	Tensile Y	30	[Mpa]
	Tensile Z	30	[Mpa]
	Compressive X	-1059	[Mpa]
	Compressive Y	-99	[Mpa]
	Compressive Z	-99	[Mpa]
	Shear XY	60	[Mpa]
	Shear YZ	30	[Mpa]
	Shear XZ	60	[Mpa]

Strain Limits	Tensile X	0.0117
	Tensile Y	0.0035
	Tensile Z	0.0035
	Compressive X	-0.0053
	Compressive Y	-0.0116
	Compressive Z	-0.0116
	Shear XY	0.0125
	Shear YZ	0.0099
	Shear XZ	0.0125

Tsai-Wu Constant	Coupling Coefficient XY	-1
	Coupling Coefficient YZ	-1
	Coupling Coefficient XZ	-1

Puck Constant	Compressive Inclination XZ	0.30
	Compressive Inclination YZ	0.25
	Tensile Inclination XZ	0.35
	Tensile Inclination YZ	0.25
	Interface Weaking Factor	0.8
	Degradation Parameter s	0.5
	Degradation Parameter M	0.5

Table 11.4: M40J UD Engineering data.

### 11.3.- TWILL T300

The Twill T300 has a fiber mass of 200 g/m<sup>2</sup> with a resin percentage of 46% and an overall thickness of 0.23.

#### Twill T300 Prepreg

Data	Density	1.42	[g/cm <sup>3</sup> ]
------	---------	------	----------------------

Coefficient of thermal expansion	Direction X	2.20E-06	[1/°C]
	Direction Y	2.20E-06	[1/°C]
	Direction Z	1.00E-05	[1/°C]

Orthotropic Elasticity	Young's Modulus X	62500	[Mpa]
	Young's Modulus Y	62500	[Mpa]
	Young's Modulus Z	6900	[Mpa]
	Poisson's Ratio XY	0.04	
	Poisson's Ratio YZ	0.30	
	Poisson's Ratio XZ	0.30	
	Shear Modulus XY	3200	[Mpa]
	Shear Modulus YZ	2700	[Mpa]
	Shear Modulus XZ	2700	[Mpa]

Stress Limits	Tensile X	630	[Mpa]
	Tensile Y	630	[Mpa]
	Tensile Z	50	[Mpa]
	Compressive X	-480	[Mpa]
	Compressive Y	-480	[Mpa]
	Compressive Z	-170	[Mpa]
	Shear XY	125	[Mpa]
	Shear YZ	65	[Mpa]
	Shear XZ	65	[Mpa]

Strain Limits	Tensile X	0.0101
	Tensile Y	0.0101
	Tensile Z	0.0072
	Compressive X	-0.0077
	Compressive Y	-0.0077
	Compressive Z	-0.0246
	Shear XY	0.0391
	Shear YZ	0.0241
	Shear XZ	0.0241

Tsai-Wu Constant	Coupling Coefficient XY	-1
	Coupling Coefficient YZ	-1
	Coupling Coefficient XZ	-1

Puck Constant	Compressive Inclination XZ	0.30
	Compressive Inclination YZ	0.25
	Tensile Inclination XZ	0.35
	Tensile Inclination YZ	0.25
	Interface Weaking Factor	0.8
	Degradation Parameter s	0.5
	Degradation Parameter M	0.5

Table 11.5: Twill T300 Engineering data.

### 11.4.- BIAXIAL T300

In this case, the biaxial has been made considering two plies of T300 UD. Each ply of UD has a fiber mass of 150 g/m<sup>2</sup> with a resin percentage of 40%.

Prepreg datasheet		Prepreg	
Fiber	T300	Mass	250.00 [g/m <sup>2</sup> ]
Type	UD	Fiber mass	60.0%
Fiber mass	150 [g/m <sup>2</sup> ]	Fiber volume	50.6%
Angle	0 [°]	Matrix volume	49.4%
Resin % in mass	40%	Density	1.483 [g/cm <sup>3</sup> ]
Fiber data		Thickness	0.1686 [mm]
	PAN	E1	117281 [Mpa]
Elastic modulus	230000 [Mpa]	E2	7907 [Mpa]
Strength	3500 [Mpa]	E3	7907 [Mpa]
Shear modulus	50000 [Mpa]	v12	0.3297
Maximum elongation	1.5%	v13	0.3297
Poisson	0.30	v21	0.0222
Density	1.76 [g/cm <sup>3</sup> ]	v31	0.0222
Alpha	-8.00E-07 [1/°C]	v23	0.4236
Matrix data		v32	0.4236
Density	1.2 [g/cm <sup>3</sup> ]	G12	4542 [Mpa]
Elastic modulus	2000 [Mpa]	G13	4542 [Mpa]
Strength	40 [Mpa]	G23	2777 [Mpa]
Shear modulus	1600 [Mpa]	alfa1	-2.87E-07 [1/°C]
Poisson	0.36	alfa2	3.99E-05 [1/°C]
Maximum elongation	2.0%	alfa3	3.99E-05 [1/°C]
Alpha	6.00E-05 [1/°C]	sig 1 tension	1789 [Mpa]
Conductivity	0.2 [W/m°C]	sig 2 tension	30 [Mpa]
Thermal capacity	1000 [J/Ke°C]	sig 3 tension	30 [Mpa]
		sig 1 compression	-813 [Mpa]
		sig 2 compression	-99 [Mpa]
		sig 3 compression	-99 [Mpa]
		shear XY	60 [Mpa]
		shear YZ	30 [Mpa]
		shear XZ	60 [Mpa]

Table 11.6: T300 UD properties.

UD T300 Prepreg

Data	Density	1.48	[g/cm <sup>3</sup> ]
Coefficient of thermal Expansion	Direction X	-2.87E-07	[1/°C]
	Direction Y	3.99E-05	[1/°C]
	Direction Z	3.99E-05	[1/°C]
Orthotropic Elasticity	Young's Modulus X	117281	[Mpa]
	Young's Modulus Y	7907	[Mpa]
	Young's Modulus Z	7907	[Mpa]
	Poisson's Ratio XY	0.33	
	Poisson's Ratio YZ	0.42	
	Poisson's Ratio XZ	0.33	
	Shear Modulus XY	4542	[Mpa]
Shear Modulus YZ	2777	[Mpa]	
Shear Modulus XZ	4542	[Mpa]	

Stress Limits	Tensile X	1789	[Mpa]
	Tensile Y	30	[Mpa]
	Tensile Z	30	[Mpa]
	Compressive X	-813	[Mpa]
	Compressive Y	-99	[Mpa]
	Compressive Z	-99	[Mpa]
	Shear XY	60	[Mpa]
	Shear YZ	30	[Mpa]
	Shear XZ	60	[Mpa]

Strain Limits	Tensile X	0.0153
	Tensile Y	0.0038
	Tensile Z	0.0038
	Compressive X	-0.0069
	Compressive Y	-0.0125
	Compressive Z	-0.0125
	Shear XY	0.0132
	Shear YZ	0.0108
	Shear XZ	0.0132

Tsai-Wu Constant	Coupling Coefficient XY	-1
	Coupling Coefficient YZ	-1
	Coupling Coefficient XZ	-1

Puck Constant	Compressive Inclination XZ	0.30
	Compressive Inclination YZ	0.25
	Tensile Inclination XZ	0.35
	Tensile Inclination YZ	0.25
	Interface Weaking Factor	0.8
	Degradation Parameter s	0.5
	Degradation Parameter M	0.5

Table 11.7: T300 UD Engineering data.

### 11.5.- TWILL T800 (ISOTROPIC AND HOMOGENEOUS)

This material has been used to represent the components made with composite materials mainly in the wheel housing simulations. In this way, it has been avoided to do simulations in which all the lamination sequences of the CFRP components had to be included.

Twill T800 Homogeneous

Data	Density	7.85	[g/cm <sup>3</sup> ]
Isotropic Secant Coefficient of Thermal Expansion	Coefficient of Thermal Expansion	1.20E-07	[1/°C]
Isotropic Elasticity	Young's Modulus	50500	[Mpa]
	Poisson's Ratio	0.33	
	Bulk Modulus	4.95E+10	[Pa]
	Poisson's Ratio XZ	1.90E+10	[Pa]
Strain-Life Parameters	Strength Coefficient	920	[Mpa]
	Strength Exponent	-0.106	
	Ductility Coefficient	0.213	
	Ductility Coefficient	-0.47	
	Cyclic Strength Coefficient	1000	[MPa]
	Cyclic Strain Hardening Exponent	0.2	
Stress Limits	Tensile Yiled Strenght	800	[Mpa]
	Compressive Yield Strength	800	[Mpa]
	Tensile Ultimate Strength	885	[Mpa]

Table 11.8: Twill T800 Engineering data.

